ELECTROMAGNETIC MODELING OF SUBSURFACE LIGHT NON-AQUEOUS PHASE-LIQUIDS SPILLS

By

Sandra Soto-Cabán

A DISSERTATION

Submitted to
Michigan State University
in partial fulfillment of the requirements
for the degree of

DOCTOR OF PHILOSOPHY

Electrical Engineering

2011

ABSTRACT

ELECTROMAGNETIC MODELING OF SUBSURFACE LIGHT NON-AQUEOUS
PHASE-LIQUIDS SPILLS

By

Sandra Soto-Cabán

Hydrocarbon contamination from fuel leaks and spills has been one of the most common ground water pollution problems in the United States for decades. Generally, underground leaks and spills are difficult to detect and locate and can cause serious health problems to people living close to the contaminated areas. The goal of this study is to simulate a contaminated region and determine its physical limits within a tolerable level of certainty given the characteristics of the soil in question without the environmental and financial cost of physical experimentation.

The first part of this study is focused in the determination of the dielectric properties of soil and contaminated soil. A coaxial fixture was designed to characterize dry and contaminated soil samples in the frequency range of 100 MHz to 1 GHz. Experimental results for contaminated and uncontaminated soil samples are presented and analyzed. Values of permittivity obtained using the designed coaxial waveguide were used to calculate the scattering electric fields of a simulated contaminated underground system. The information collected from these simulations was used in the reconstruction of the contrast profile of two lossless configurations involving dielectric circular cylinders buried in soil. The image-reconstruction algorithm is based on the Fourier diffraction theorem and multiple frequencies were used to improve resolution.

The problem was simulated using a two-dimensional formulation since three-dimensional structures need not be considered in the context of the underground mapping application. This study is not intended to achieve buried material identification of contaminants. However, a wide, full volume scanning of a potentially contaminated area is useful for ecological impact

mitigation since it can be coupled with borehole assays to determine the specific contaminant and extent of contamination. With such information, environmental engineers can determine the need and the most suitable method for mitigation. Hence, the proposed radio frequency based survey research is meant to provide a screening tool to be used in concert with other methods.

I dedicate this dissertation to my wonderful family, particularly to my understanding and patient husband, Ferdinand, who has put up with these many years of research, and to our children, Gabhriel, Fernando, and Frances who are the joy of our lives and my inspiration.

ACKNOWLEDGEMENTS

TABLE OF CONTENTS

LIST OF FIGURES

LIST OF TABLES

KEY TO SYMBOLS AND ABBREVIATIONS

DT   Diffraction Tomography

EM   Electromagnetic

GPR   Ground penetrating radar

LNAPL   Light non-aqueous phase liquids

LUST   Leaking underground storage tank

NIST   National Institute of Standards and Technology

RCS   Radar cross section

SAR   Synthetic Aperture Radar

SNR   Signal-to-Noise Ratio

SW   Scattering width

TE   Transverse electric

TEM   Transverse electromagnetic

TM   Transverse magnetic

TR   Transmission/reflection

UHF   Ultra-high frequency

VNA   Vector network analyzer

CHAPTER 1

INTRODUCTION

Hydrocarbon contamination from fuel leaks and spills has been one of the most common ground water pollution problems in the United States for decades [1]. In particular, leaks from underground storage tanks and improper disposal of gasoline and oil threaten drinking water wells, lakes, streams, and basements all over the country [2]. Hydrocarbon contamination can be widely dispersed or confined to a local region and they can contain a variety of chemicals that can cause serious health problems to people living close to the contaminated areas. Leaks in underground storage tanks and underground fuel transfer lines are difficult to detect and locate. Often the leaks are so small that routine tests are ineffective in locating the source of the pollutant. The rate of dissipation of hydrocarbon contamination in soil is extremely slow in many cases and even a small fuel leak can produce serious contamination that is extremely costly to remediate [3].

Most hydrocarbons are lighter than water with a low dielectric permittivity. Because of these properties, they are known as light non-aqueous phase liquids (LNAPL). At LNAPL contamination sites, LNAPL can form a pool in the subsurface on top of the water table [4]. The following figures illustrate two examples of hydrocarbon contamination. Figure 1 is a cross sectional view of a hypothetical LNAPL spill due to improper disposal of contaminants and Figure 2 is an example of underground water contamination due to a leaking storage tank.
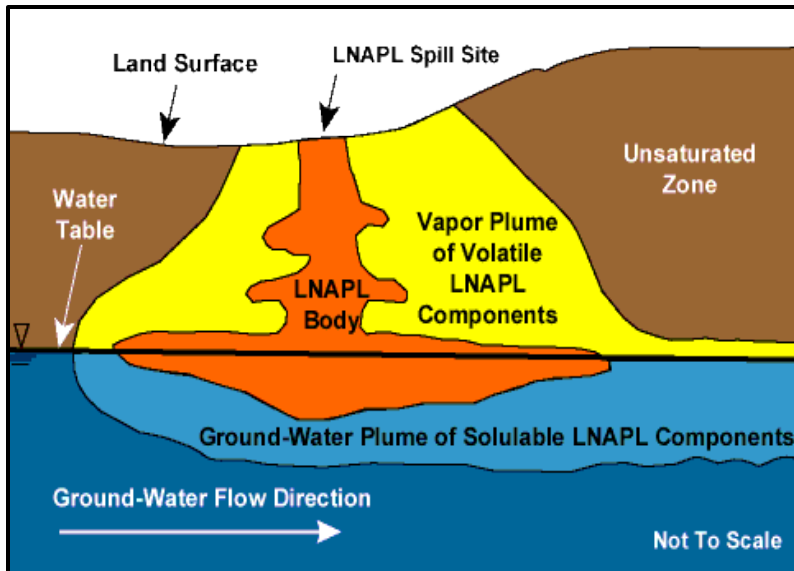
Figure 1-1. Cross-sectional view of a hypothetical LNAPL spill. Figure has been adapted from Delin and others, 1998, USGS Fact Sheet FS-084-98. For interpretation of the references to color in this and all other figures, the reader is referred to the electronic version of this dissertation.
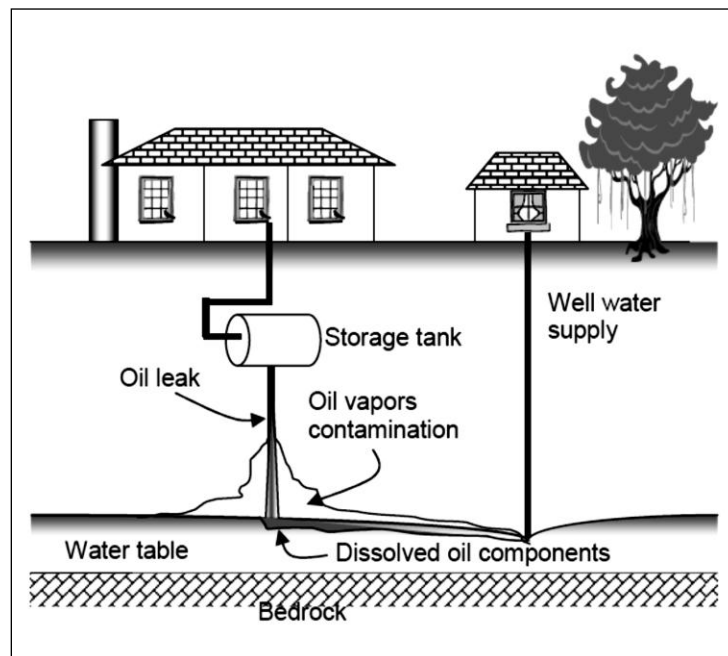
Figure 1-2. A schematic of a typical leaking underground storage tank (LUST) spill site. The leaky tank releases gasoline, or LNAPL. The gasoline descends through the unsaturated soil zone to float on the water table (gasoline is lighter than water) causing contamination of the aquifer [5].

In view of the magnitude and the continuing nature of this problem, it is important that techniques for detecting and mapping hydrocarbon contamination in soil and ground water be continually improved. There are various methods used to detect organic contaminants in soil. The most common are chromatography and mass spectrometry [6]. These methods are based on chemical analysis of the soil pore-fluid and are both time consuming and expensive. As an alternative to chemical analysis, geophysical methods, such as surface geophysics and borehole geophysical logging, can be used to aid in characterizing changes in subsurface features [7]. These methods are based on the propagation of electromagnetic waves and their performance is determined fundamentally by the soil electromagnetic properties and the target characteristics. Because of that, before using any of the geophysical methods available, a better knowledge of the dielectric properties of the media involved in the investigation is needed.

The goal of this study is to simulate a contaminated region and have an algorithm that can be used to determine its physical limits within a tolerable level of certainty given the characteristics of the soil in question. The first part of this study is focused in the determination of the dielectric properties of soil and contaminated soil. A durable and cost effective coaxial waveguide was designed to obtain permittivity values of the soils. Dielectric measurements of dry, wet, and contaminated soil were performed in a frequency range of 100 to 1000 MHz. The design of the coaxial waveguide and measurement results are presented in Chapter 2. Values of permittivity obtained using the designed coaxial waveguide were used for a computer simulation of a contaminated underground system. The soil was modeled as a homogeneous dielectric space and the contaminated area was modeled as an inhomogeneous dielectric space. The contaminated area was assumed to be composed of wet and contaminated soil. Analytical formulation of the electromagnetic scattering from the contaminated system is presented in Chapter 3. Different

system configurations were simulated and the information collected from these simulations was used in the reconstruction of the contrast profile of two lossless configurations involving dielectric circular cylinders buried in soil. The image-reconstruction algorithm is based on the Fourier diffraction theorem [8] and multiple frequencies were used to improve resolution [9]. The inversion algorithm and reconstructed contrast images are presented in Chapter 4. The concluding remarks and the future work are issued in Chapter 5.

This study is not intended for a direct identification of contaminants. However, a wide, full volume scanning of a potentially contaminated area is useful for ecological impact mitigation since it can be coupled with borehole assays to determine the specific contaminant and extent of contamination. With such information, environmental engineers can determine the need and the most suitable method of mitigation. Hence, the proposed radio frequency based survey research is meant to provide a screening tool to be used in concert with other methods.

CHAPTER 2

COAXIAL WAVEGUIDE FIXTURE FOR THE MEASUREMENT OF DIELECTRIC PROPERTIES OF CONTAMINATED SOIL AT UHF FREQUENCIES

2.1 Introduction

Identification of organic contaminants in the subsurface can be obtained using geophysical methods such as ground penetrating radar (GPR) [10] and borehole logging [11]. The performance of these microwave technologies is determined fundamentally by the soil electromagnetic (EM) properties and the target characteristics at study sites as well as the sensor equipment. From the perspective of the signal, both wave speed and power attenuation depends on the dielectric properties of the propagation media.

Many researchers have collected data on soil dielectric properties using different measurement techniques. Measurement of dielectric properties involves measurements of the complex relative permittivity (ε_r) and complex relative permeability (μ_r) of the materials. There are many techniques developed for measuring the complex permittivity and permeability and each technique is limited to specific frequencies, materials, applications, etc. by its own constraint. Some measurement techniques include open-ended coaxial probe, free-space, resonant, and transmission/reflection line. Baker-Jarvis *et al.* present a discussion of these prior efforts in [12]. Curtis [13] used a coaxial transmission/reflection measurement system to collect complex dielectric property data for soils at 45 MHz to 26.5 GHz. Different from his work, this research presents a new, large-volume coaxial sample holder, designed and fabricated at Michigan State University for the dielectric measurements of soil and contaminated soil at the

UHF band. This fixture was designed and used since it offered wide bandwidth and the ability to measure a volume of material that is sufficiently large at the operating frequencies so that homogenization of properties is assured given the dimensions of the potential solid phase of the samples.

The transmission/reflection (TR) method is widely used for the measurement of solid materials. In the TR method, a material sample is placed in a section of a waveguide or coaxial line after calibration of the fixture has been performed, and an incident electromagnetic field is applied. The technique involves measurement of the reflected (S_{11}) and transmitted signal (S_{21}). Scattering equations are found from the analysis of the electric field at the sample interface. The scattering equations relate the measured scattering parameters to the permittivity (ε) and permeability (μ) of the material through an inversion process. In developing the scattering equations, only the fundamental waveguide mode is assumed to propagate.

The TR inversion method was first introduced by Nicholson and Ross [14] in the early 1970's. In their paper, a new method for obtaining the complex permittivity and permeability of linear materials over a broad range of frequencies is presented. Before this study, such measurements were made at fixed frequencies using slotted-line or impedance bridge configurations. After Nicholson and Ross, Weir [15] determined the complex values of ε and μ from measurements made directly in the frequency domain. This is known as the Nicholson-Ross-Weir (NRW) method. This method is a commonly used technique for direct calculation of both the permittivity and permeability from the S-parameters. However, the technique diverges for low-loss materials at frequencies corresponding to integer multiples of one-half wavelength in the sample. Baker-Jarvis *et al*. [16] improved the NRW method by allowing measurements to be taken on samples of arbitrary length. This technique is known as NIST Iterative method.

NIST Iterative technique performs the calculation using a Newton-Raphson's root finding technique and is suitable for permittivity calculation only. It works well if a good initial guess is available and is suitable for long samples and characterizing low loss materials. Boughriet, *et al.* [17] developed a non-iterative transmission/reflection method applicable to permittivity measurements using arbitrary sample lengths in wide-band frequencies. This method is based on a simplified version of the NRW method and its accuracies are comparable to the iterative technique. It does not need an initial estimation of permittivity and can perform the calculation very fast. Later, Courtney [18] used the Nicholson and Ross method, and extended the procedure to account for the infinite set of transmissions and reflections of the transient wave at the interfaces of the material sample.

In this chapter, the design of a new, large-volume coaxial sample holder for the dielectric measurements of soil and contaminated soil at the UHF band is presented. Unlike traditional sample holders common in many electromagnetic material characterization laboratories, it can accommodate significant volumetric samples of material. The sample holder is a symmetric coaxial waveguide fabricated using brass. It is intended to operate in a frequency range between 100 MHz and 1 GHz. Using a Vector Network Analyzer (VNA), the values for complex relative permittivity $(\varepsilon_r = \varepsilon_r' - j\varepsilon_r'')$ and complex relative permeability $(\mu_r = \mu_r' - j\mu_r'')$ were calculated using the TR method.

2.2 Transmission/Reflection method

A sample of material with unknown electromagnetic parameters ε_r, μ_r, and known thickness d is placed in an air-filled coaxial sample holder. A typical cylindrical coaxial sample holder is illustrated in Figure 2-1.
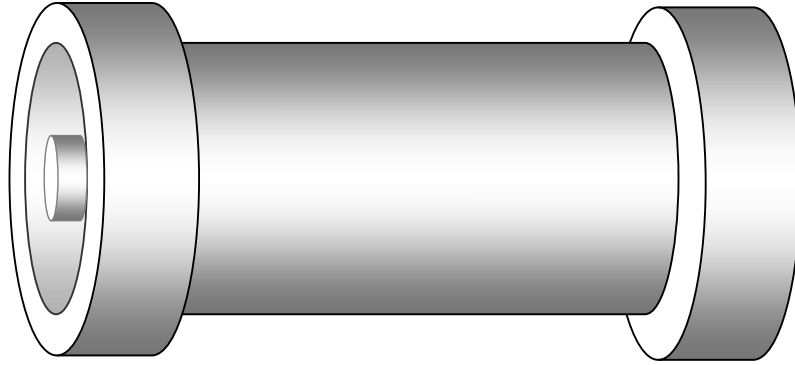
Figure 2-1. Coaxial sample holder.

Figure 2-2 shows a cross-sectional view of the sample holder with the material-under-test placed at the center of the holder in the volume between the inner and outer conductors. The calibration reference plane positions for the measurements are shown and the electric fields in each region of the line are indicated.
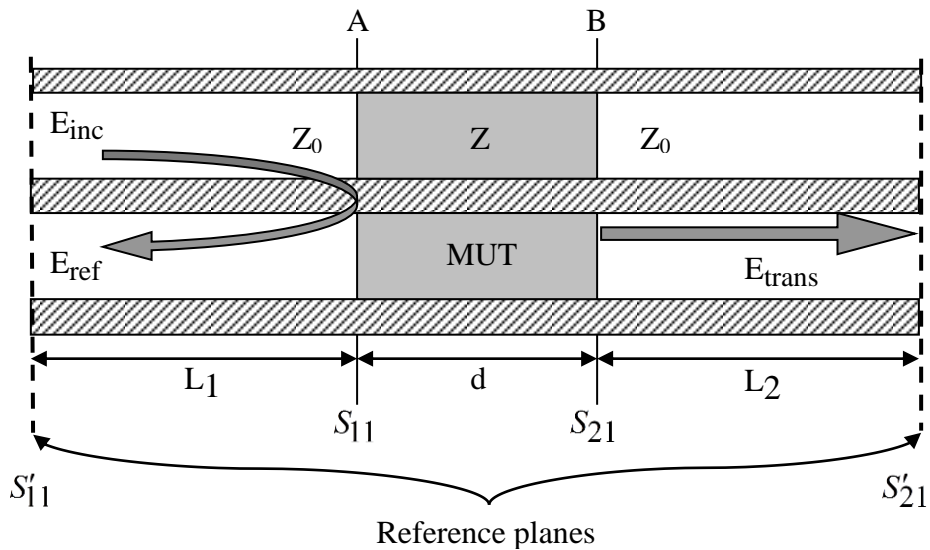
Figure 2-2. Cross-sectional view of the coaxial sample holder.

A transverse electromagnetic (TEM) wave propagates on the coaxial transmission line. Measurements of the S-parameters, indicated as S'_{11} and S'_{21}, are made at the reference planes. These values can be written for a time-harmonic excitation as:

$$S'_{11}(\omega) = \frac{E_{ref}}{E_{inc}} \tag{2.1}$$

$$S'_{21}(\omega) = \frac{E_{tran}}{E_{inc}} \tag{2.2}$$

where E_{inc} is the incident field, E_{ref} is the total reflected field, and E_{tran} is the total transmitted field. Translating these parameters to the interfaces between regions yields

$$S_{11}(\omega) = S'_{11}(\omega) e^{j2\beta_0 L_1} \tag{2.3}$$

$$S_{21}(\omega) = S'_{21}(\omega) e^{j(\beta_0 L_1 + \beta_0 L_2)} \tag{2.4}$$

where $\beta_0 = \omega/c_0$, $\omega = 2\pi f$, f = frequency, c_0 = speed of light in vacuum, and L_1 and L_2 are the distances between the sample and the reference plane positions. The complex transient reflection coefficient Γ can be expressed as:

$$\Gamma_{12} = \frac{Z - Z_0}{Z + Z_0} = \frac{\sqrt{\mu_{r2}/\varepsilon_{r2}} - 1}{\sqrt{\mu_{r2}/\varepsilon_{r2}} + 1} \tag{2.5}$$

where $Z_0 = \sqrt{\mu_0/\varepsilon_0}$, $Z = \sqrt{\mu_2/\varepsilon_2}$, $\mu_2 = \mu_0\left(\mu'_{r2} - j\mu''_{r2}\right)$, $\varepsilon_2 = \varepsilon_0\left(\varepsilon'_{r2} - j\varepsilon''_{r2}\right)$.

The transmission coefficient through the sample material can be written as:

$$z = e^{-j\beta_2 d} \tag{2.6}$$

where $\beta_2 = \omega\sqrt{\varepsilon_{r2} \cdot \mu_{r2}}/c_0$.

Equations (2.3) and (2.4) can be rewritten in terms of the wave impedances as:

$$S_{11}(\omega) = \frac{\left(Z^2 - Z_0^2\right)\left(1 - e^{-j2\beta_2 d}\right)}{(Z + Z_0)^2 - (Z - Z_0)^2 e^{-j2\beta_2 d}} \tag{2.7}$$

and

$$S_{21}(\omega) = \frac{4(Z_0 Z)e^{-j\beta_2 d}}{(Z + Z_0)^2 - (Z - Z_0)^2 e^{-j\beta_2 d}}. \tag{2.8}$$

Using transmission-line theory [14]:

$$S_{11}(\omega) = \frac{E_A}{E_{inc}} = \frac{\left(1 - z^2\right)\Gamma_{12}}{1 - \Gamma_{12}^2 z^2} \tag{2.9}$$

$$S_{21}(\omega) = \frac{E_B}{E_{inc}} = \frac{(1 + \Gamma)(1 - \Gamma)z}{1 - \Gamma_{12}^2 z^2} = \frac{\left(1 - \Gamma_{12}^2\right)z}{1 - \Gamma_{12}^2 z^2} \tag{2.10}$$

where E_A and E_B are the fields at planes A and B, respectively.

From the above equations, the complex permittivity and complex permeability can be expressed as:

$$\varepsilon_r = \left(\frac{1 - \Gamma_{12}}{1 + \Gamma_{12}}\right)\left(\frac{j\ln(1/z)c}{2\pi f d}\right) \tag{2.11}$$

10

and

$$\mu_r = \left(\frac{1+\Gamma_{12}}{1-\Gamma_{12}}\right)\left(\frac{j\ln(1/z)c}{2\pi fd}\right).$$

(2.12)

Using these equations, the complex permeability and permittivity can be obtained from measurements of the transmission and reflection scattering coefficients of the material. For non-magnetic materials, $\mu_r = 1$. This eliminates the ill-behaved term $(1-\Gamma_{12})/(1+\Gamma_{12})$, which produces undesired ripples in the extracted ε_r and μ_r [17]. This technique gives smooth permittivity results, with no divergences at frequencies that are multiples of one-half wavelength, is accurate, arbitrary length of samples can be used, and no initial guess is needed. Some disadvantages of the technique are that is only applicable for permittivity measurements and the challenge of solving the logarithm of a complex function.

2.3   Measurement procedure

2.3.1   Design of the coaxial waveguide fixture

The designed sample holder is a symmetrical coaxial waveguide fixture made of brass ($\sigma = 1.57 \times 10^7$ S/m, $\mu = 4\pi \times 10^{-7}$ H/m). It was designed to operate in a frequency range between 100 MHz to 1 GHz. The length of the coaxial waveguide is slightly less than a half-wavelength, for the dominant TEM mode, of the signal at the desired higher frequency of 1 GHz. The distributed electromagnetic parameters of the coaxial line fixture were determined using the following equations [19]:

$$R = \frac{R_S}{2\pi b}\left[1 + \frac{b}{a}\right]$$

$$L = \frac{\mu}{2\pi}\ln\left(\frac{b}{a}\right)$$

$$C = \frac{2\pi\varepsilon'}{\ln\left(\frac{b}{a}\right)} \qquad (2.13)$$

$$G = \omega C \tan\theta R = \frac{R_S}{2\pi b}\left[1 + \frac{b}{a}\right]$$

where R is the distributed resistance, L is the distributed inductance, C is the distributed capacitance, and G is the distributed conductance of the line. The inner diameter of the outer conductor is b and a is the outer diameter of the inner conductor. R_S is surface resistivity, ε' is the real part of the permittivity of the dielectric material, and $\tan\theta$ is the loss tangent of the dielectric filling. These EM parameters can be used to determine the propagation constant γ, and the characteristic impedance Z_0 of the coaxial waveguide. For the designed fixture, $L = 1.704$ x 10^{-7} H/m and $C = 6.528\text{x}10^{-11}$ F/m. The characteristic impedance is $Z_0 = \sqrt{L/C} = 51.08$ Ω. The propagation constant γ is $j2.095$ rad/m at 100 MHz, $j10.477$ rad/m at 500 MHz, and $j20.954$ rad/m at 1 GHz. The transverse electric mode TE_{11} has the lowest cutoff frequency of all the higher modes. For this mode, the cutoff frequency was 1.785 GHz. The intended frequency range of operation is below the cutoff condition and the transverse electromagnetic mode (TEM) will be the only mode of propagation within the frequency range given sufficient stand-off distance for the measurement ports and the calibration planes (e.g. the axial boundaries of the MUT). The dimensions of the coaxial fixture are illustrated in Figure 2-3. The total volumetric capacity of the sample holder is approximately 552 cm^3. This volume permits homogenization of the

12

material properties even with relatively large (order of millimeter) solid phase constituent materials in the soil mixture.
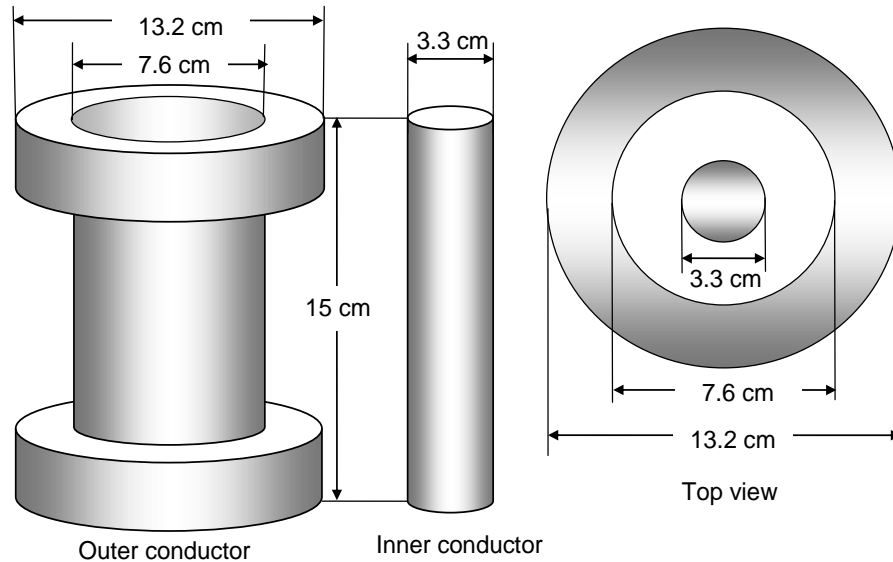
Figure 2-3. Dimensions of the coaxial waveguide sample holder. The inner conductor is placed inside the outer conductor for measurements as shown in the top view.

2.3.2 Experimental setup

The designed coaxial waveguide fixture was connected to an HP 8753D Vector Network Analyzer (VNA) using a set of ASTM D 4935 flanged coaxial fixtures [20] shown in Figure 2-4. The experimental setup is shown in Figure 2-5. The VNA was used for measurement of the S-parameters of the sample. The Thru-Reflection-Line (TRL) method was used for calibration purposes [21]. The Thru standard was realized by directly connecting the two ASTM D 4935 coaxial sections. A circular brass plate was placed at the end of the coaxial section to provide a reflection standard. The line standard was done using the empty sample holder fixture between the two ASTM D 4935 coaxial sections. The calibration configurations are shown in Figure 2-6.

After the calibration process, the network analyzer reported the S-parameters of the sample, which then were processed to obtain the required EM properties.

Figure 2-4. ASTM D 4935 Flanged Coaxial Fixture
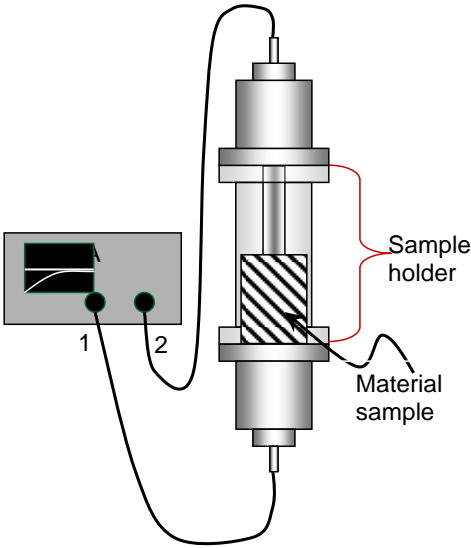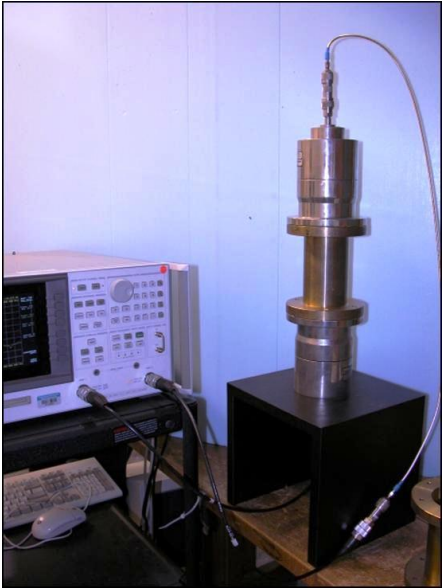
Figure 2-5. Measurement setup. The material sample can be seen in the interior of the sample holder.
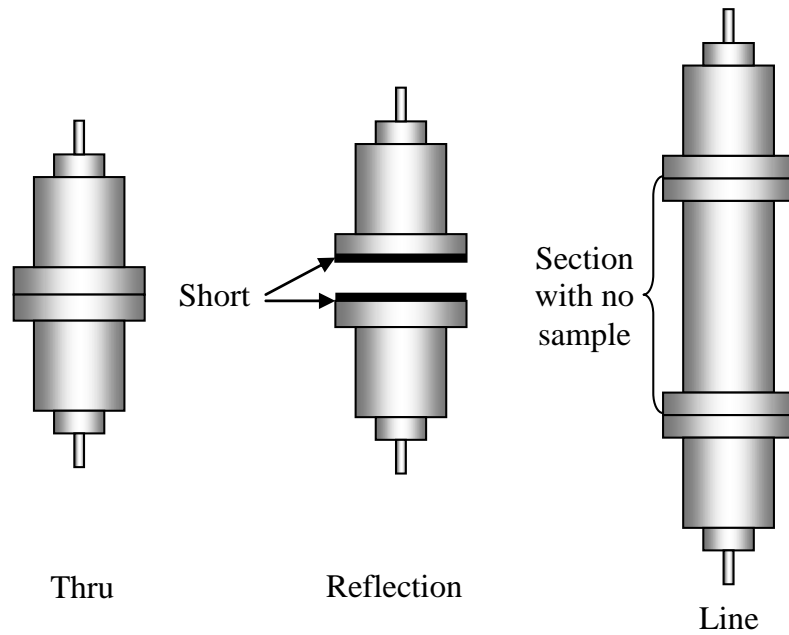
Figure 2-6. Calibration standards.

To test the system, air was used as the first sample material. Values of permittivity and permeability for air are well known and well approximated by the free-space values of these parameters. The measured complex permittivity and permeability for air are shown in Figure 2-7. Measured values are in accordance with the expected values.

The second material used for testing was Plexiglas. Two Plexiglas samples with lengths 9.5 cm and 4.75 cm were machined to fit snugly inside the coaxial fixture. The samples were placed as shown in Figure 2-5, at the bottom of the sample holder instead of the center. This configuration allows for a flat surface when materials with loose particles, like soil, are used. For the two Plexiglas samples, the average measured values of permittivity and permeability were $\varepsilon_r = 2.58 - j0.02$ and $\mu_r = 1.01 - j0.02$ in a frequency range from 100 to 950 MHz. These

values are in accordance with the typical values for Plexiglas [22]. Measured values for the two

Plexiglas samples are presented in Figure 2-8 and Figure 2-9.
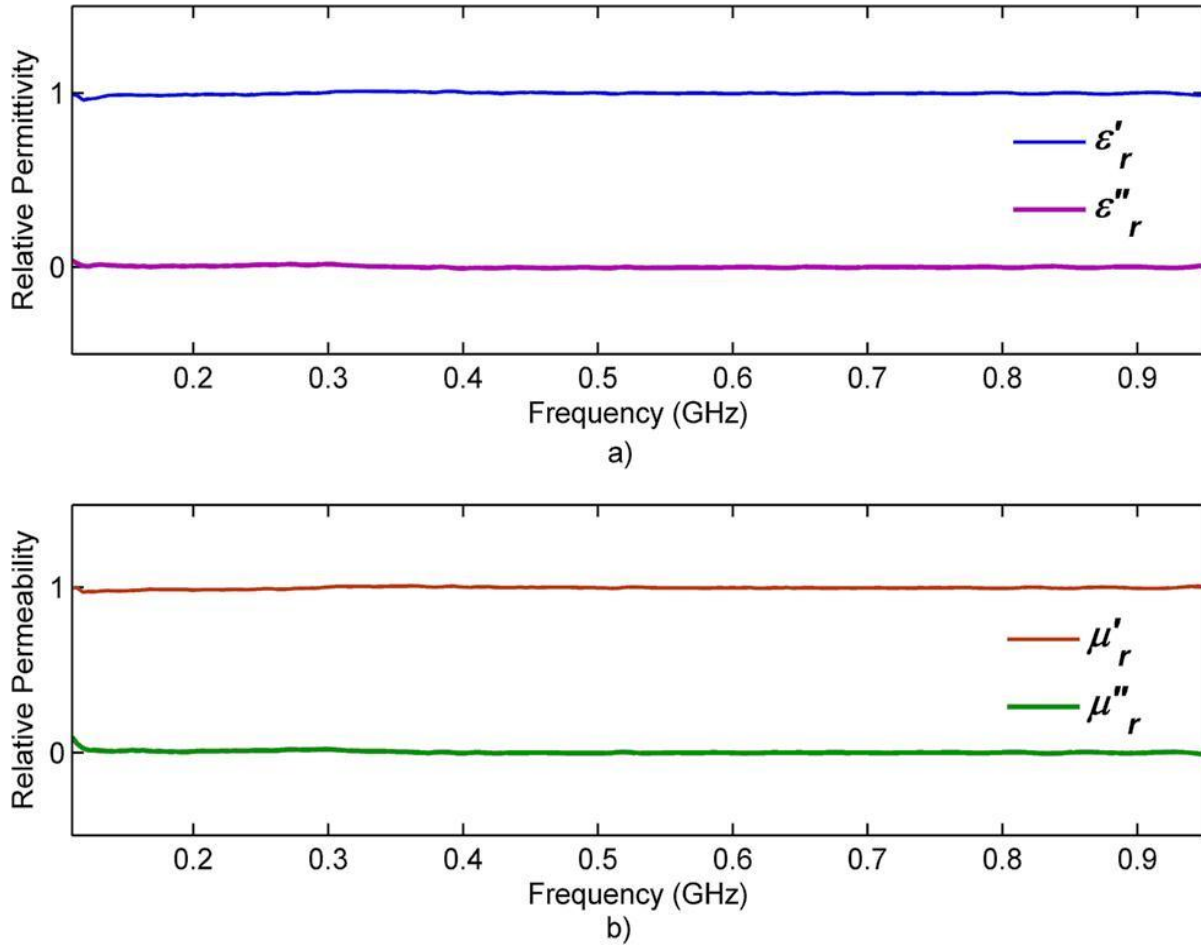
Figure 2-7. Complex relative permittivity and permeability of air in a frequency range from 100 to 950 MHz. a) Relative permittivity $\left(\varepsilon_r = \varepsilon_r' - j\varepsilon_r''\right)$. b) Relative permeability $\left(\mu_r = \mu_r' - j\mu_r''\right)$.
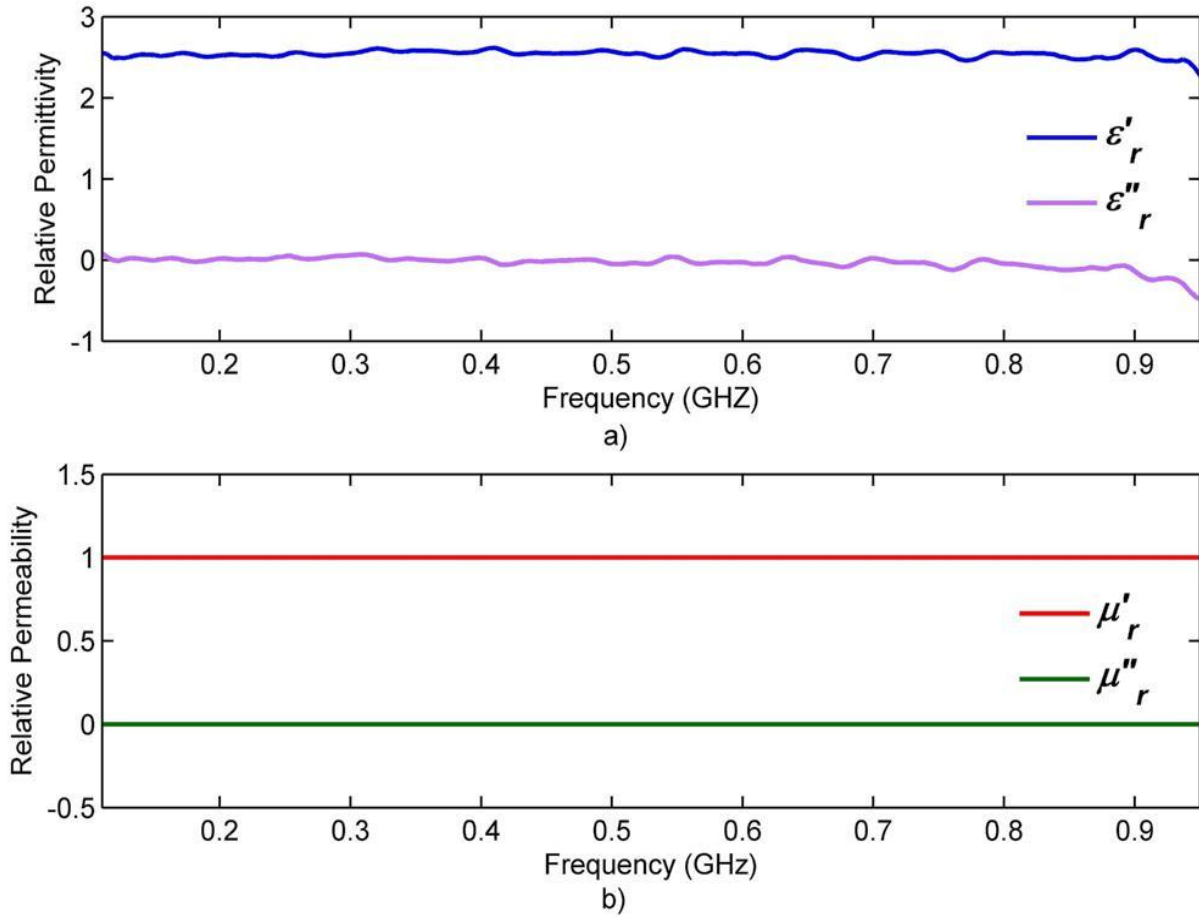
Figure 2-8. Complex relative permittivity and permeability of 9.50 cm long Plexiglas sample in a frequency range from 100 to 950 MHz. a) Relative permittivity $\left(\varepsilon_r = \varepsilon_r' - j\varepsilon_r''\right)$. b) Relative permeability $\left(\mu_r = \mu_r' - j\mu_r''\right)$.
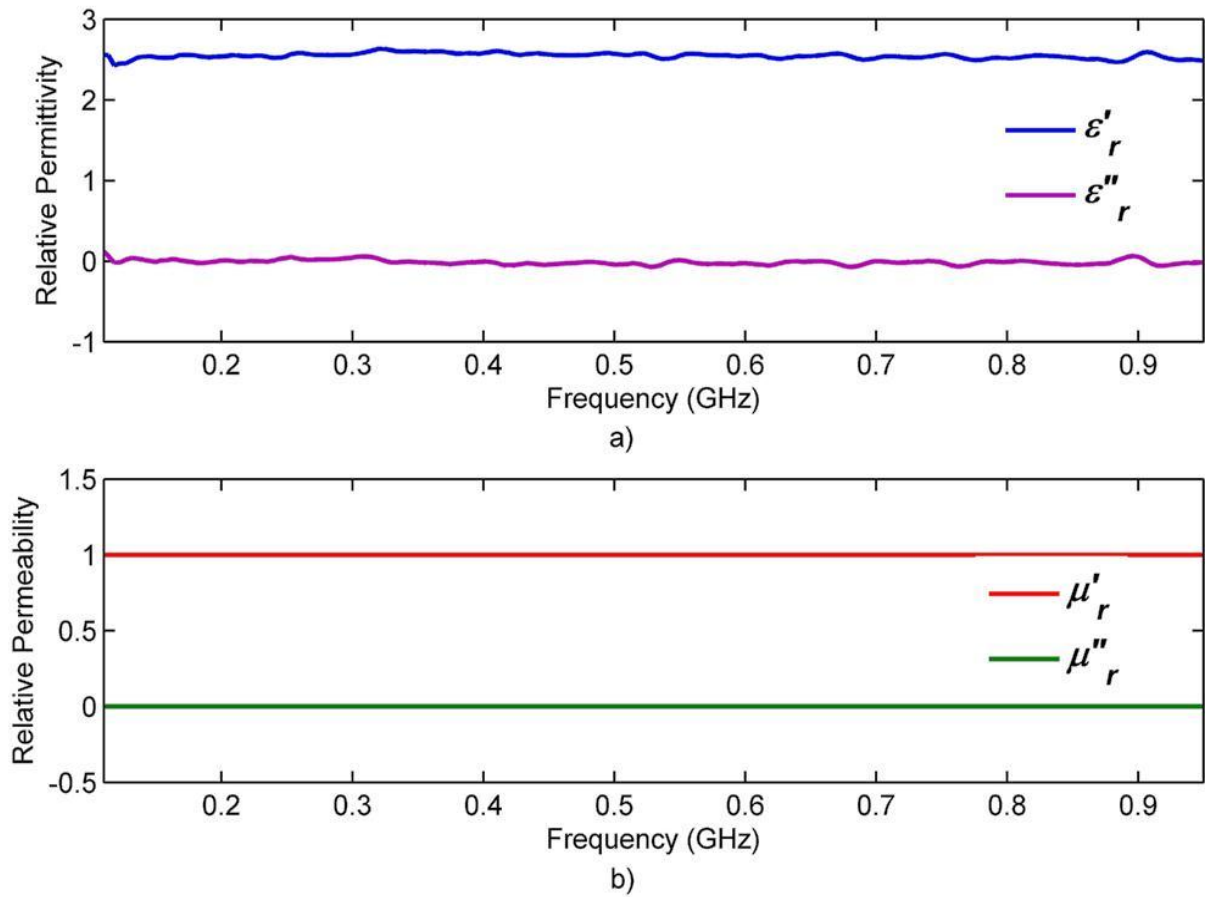
Figure 2-9. Complex relative permittivity and permeability of 4.75 cm long Plexiglas sample in a frequency range from 100 to 900 MHz. a) Relative permittivity $\left(\varepsilon_r = \varepsilon'_r - j\varepsilon''_r \right)$. b) Relative permeability $\left(\mu_r = \mu'_r - j\mu''_r \right)$.

2.4   Sample preparation

Samples of dry soil, wet soil, and contaminated soil were prepared. The soil was collected in Muskingum County, Ohio; specifically in the Zanesville region. Map of the region with soil physical properties is shown in Figure 2-10. Description of the terms in each region of the map and corresponding soil properties are presented in Table 2-1.

Figure 2-10. The red star indicates the area where the soil was collected. The map was generated using the Web Soil Survey tool of the USDA Natural Resources and Conservation Service - Soil Survey Area Map for Muskingum County OH (Survey OH119) [23].

Table 2-1. Physical Soil Properties – Muskingum County, Ohio

Map symbol and soil name	Depth (inches)	Sand (%)	Silt (%)	Clay (%)
AfB: Alford	0-10	--	--	12-26
	10-50	--	--	22-32
	50-80	--	--	8-20
AfC2: Alford	0-10	--	--	12-26
	10-50	--	--	22-32
	50-80	--	--	8-20
CtE: Coshocton	0-8	--	--	15-23
	8-20	--	--	18-30
	20-40	--	--	24-41
	40-60	--	--	24-41
	60-75	--	--	--
Me: Melvin	0-3	--	--	12-17
	3-44	5-15	50-83	12-35
	44-60	15-35	30-78	7-35
Ne: Newark	0-11	--	--	7-27
	11-32	8-20	50-74	18-35
	32-60	10-20	50-78	12-40
Ud: Udorthents	--	--	--	--
WuC2: Westmoreland	0-9	--	--	15-30
	9-40	10-35	30-70	20-35
	40-60	10-35	30-72	18-35
	60-62	--	--	--
ZnB: Zanesville	0-7	--	42-95	12-27
	7-28	5-20	45-70	18-35
	28-45	5-20	47-77	18-33
	45-80	10-35	25-70	20-40
ZnC2: Zanesville	0-7	--	42-95	12-27
	7-28	5-20	45-70	18-35
	28-45	7-42	40-60	18-33
	45-80	0-38	42-64	20-40

Soil physical properties were measured and results compared with the data presented in Table 2-1. The collected soil had a composition of approximately 15% clay, 5% sand and 80% silt. Based on these results and Table 2-1, the soil is Zanesville silt loam (ZnC2) which agreed with the soil in the collection region.

The collected soil was dried following Standard T 265 of the American Association of State Highway and Transportation Officials (AASHTO) [24]. The soil was heated in an oven at 105°C for approximately 24 hours. The weight of the dry soil samples was measured, and a predetermined amount of distilled water was then added to achieve the desired volumetric moisture content. After weighing the wet soil samples, they were sealed and allowed to settle for a few hours. From the weight of the dry soil W_d, and the weight of the water added W_w, the gravimetric moisture content m_g, can be calculated using $m_g = W_w/W_d$. The volumetric moisture content m_v, is determined by $\rho_b m_g$, where ρ_b is the bulk density of the soil sample given by W_d/V, where V is the volume of the dry sample [25]. Since these values are bulk densities, the possibility of air spaces between the soil particles is ignored.

2.5   Calculation of soil electromagnetic properties

Researchers have developed semi-empirical dielectric mixing models that calculate the electrical properties of the different components of soil. For this study, a model for predicting both the real and imaginary parts of the relative permittivity ε_r ($\varepsilon_r = \varepsilon_r' - j\varepsilon_r''$) for a known frequency band and different moisture levels was required. Peplinski *et al.* [26] developed a semi-empirical dielectric model for soils, covering the frequency range of 0.3 to 1.3 GHz. The model provides frequency-dependent expressions for the real and imaginary parts of the relative

dielectric constants of a soil medium in terms of the fraction of sand particles S, the fraction of clay particles C, the volumetric water content m_v, and the bulk density of the soil ρ_b, all being available parameters. The real part of the complex relative permittivity for the bulk soil is approximated as:

$$\varepsilon'_m = 1.15 \left[1 + \frac{\rho_b}{\rho_s} \left(\varepsilon_s^\alpha \right) + m_v^{\beta'} \varepsilon_{fw}'^\alpha - m_v \right]^{1/\alpha} - 0.68 \ . \tag{2.14}$$

The imaginary part is given as:

$$\varepsilon''_m = \left[m_v^{\beta''} \varepsilon_{fw}''^\alpha \right]^{1/\alpha} \tag{2.15}$$

where $\varepsilon_m = \varepsilon'_m - j\varepsilon''_m$ is the relative complex dielectric constant of the soil-water mixture, $\rho_s = 2.66$ g/cm^3 is the specific density of the solid soil particles, $\alpha = 0.65$ is an empirically determined constant [27], and β' and β'' are soil-type dependent constants given by

$$\beta' = 1.2748 - 0.519S - 0.152C \tag{2.16}$$

and

$$\beta'' = 1.33797 - 0.603S - 0.166C \tag{2.17}$$

The quantities ε'_{fw} and ε''_{fw} are the real and imaginary parts of the relative dielectric constant of free water given by a Debye-type dispersion equation [28] are

$$\varepsilon'_{fw} = \varepsilon_{w\infty} + \frac{\varepsilon_{w0} - \varepsilon_{w\infty}}{1 + \left(2\pi f \tau_w\right)^2} \tag{2.18}$$

$$\varepsilon''_{fw} = \frac{2\pi f \tau_w \left(\varepsilon_{w0} - \varepsilon_{w\infty}\right)}{1 + \left(2\pi f \tau_w\right)^2} + \frac{\sigma_{eff}}{2\pi\varepsilon_0 f} \frac{\left(\rho_s - \rho_b\right)}{\rho_s m_v} \tag{2.19}$$

where ε_0 is the permittivity of free space, f is the frequency in hertz, τ_w is the relaxation time for water, ε_{w0} is the static dielectric constant for water, and $\varepsilon_{w\infty} = 4.9$ is the high-frequency limit of ε'_{fw}. At room temperature (20°C), $2\pi \cdot \tau_w = 0.58 \times 10^{-10} s$ and $\varepsilon_{w0} = 80.1$ [28]. The effective conductivity σ_{eff} derived in [26] is given by

$$\sigma_{eff} = 0.0467 + 0.2204\rho_b - 0.4111S + 0.6614C \tag{2.20}$$

When a contaminant is added to the soil samples, a mixing formula is used to calculate the effective permittivity of the mixture [29]. Mixing formulas or rules are used to provide an approximate electromagnetic description for the structural complexity of materials occurring in nature. Mixing formulas use the concept of effective or macroscopic permittivity, which implies that the mixture responds to electromagnetic excitation as if it were homogeneous [30]. The size of the inclusions in the mixture and the spatial correlation length of the permittivity function need to be small with respect to the wavelength. There are many effective medium approximations [29]-[31]. Perhaps the most common mixing rule is the Maxwell Garnett formula [32]. It is simple in appearance but with broad applicability. The effective permittivity of a mixture ε_{eff} relative to the environment permittivity ε_e is determined by only two parameters and obeys the following rule:

$$\varepsilon_{eff} = \varepsilon_e + 3v_i\varepsilon_e \frac{\varepsilon_i - \varepsilon_e}{\varepsilon_i + 2\varepsilon_e - v_i(\varepsilon_i - \varepsilon_e)} \tag{2.21}$$

where ε_i is the inclusion permittivity and v_i is the volume fraction of the inclusions. Other important mixing rules in the remote sensing community are the Polder–van Santen formula [33], known as Bruggerman formula [34], and the Coherent Potential formula [35]. For dilute mixtures ($v_i \ll 1$), all three mixing rules, Maxwell Garnet, Polder–van Santen, and Coherent Potential, predict the same results [30].

2.6   Experimental results

First, the permittivity of the dry soil sample was measured. The obtained value of permittivity was compared to the predicted value using the dielectric model for soils developed by Peplinski *et al*. [26]. Figure 2-11 illustrates the measured and predicted relative complex permittivity of dry soil. Averaged measured relative permittivity in a frequency range from 300 to 800 MHz for dry soil is 2.0954-j0.0028. In the same frequency range, the calculated relative permittivity using the Peplinski model is 2.0863-j0.000.
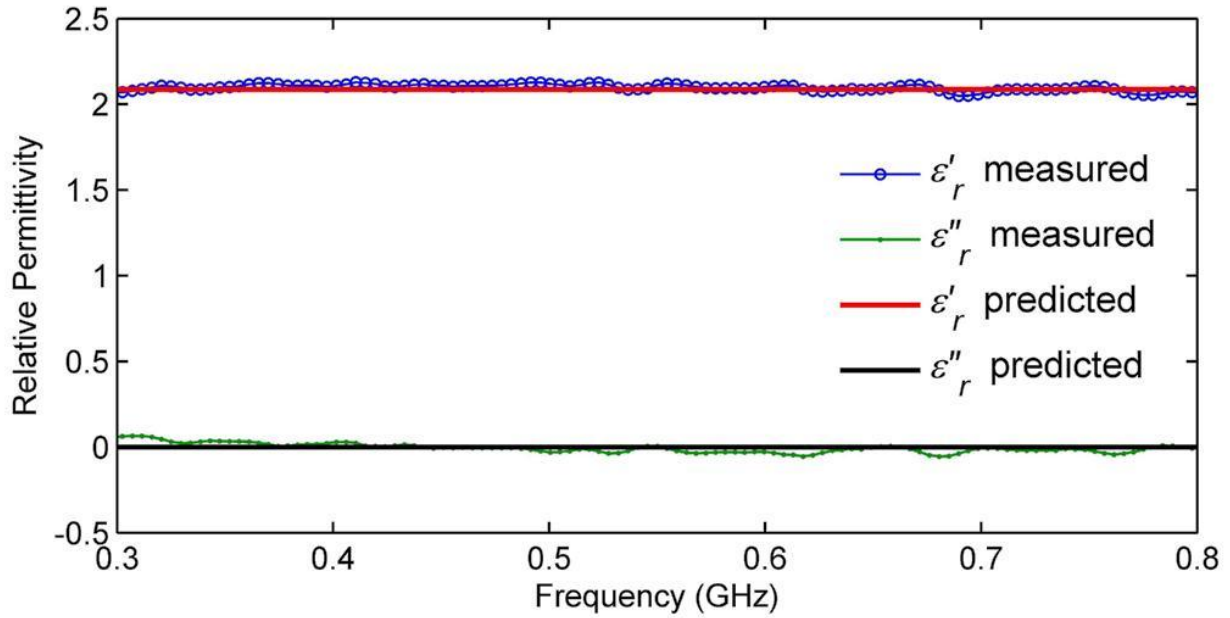
Figure 2-11. Complex relative permittivity of dry soil sample. Predicted values of permittivity were obtained using the dielectric model for soils developed by Peplinski *et al.* [26].

Once we know the permittivity of dry soil, the second step is to measure the permittivity of wet soil. First, the dielectric spectra for bulk/liquid water were calculated using equations 2.18 and 2.19 of the Debye model. The dielectric spectra of bulk/liquid water are presented in Figure 2-12. Relaxation times of 9.23, 8.30, 6.48, and 5.17 picoseconds were used for liquid water at a temperature T = 20, 25, 35, and 45°C, respectively [36]. The obtained permittivity values using the Debye model and measured data are in agreement with the literature, within 0.5% of previously reported data [37].
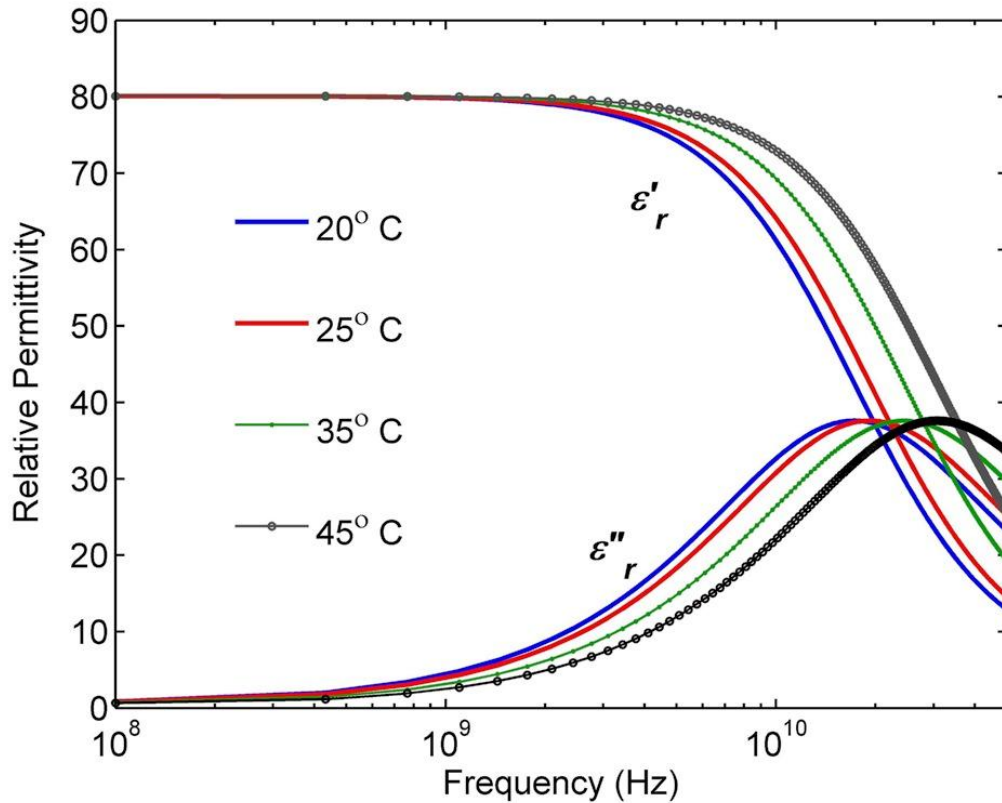
Figure 2-12. Dielectric spectra of bulk/liquid water calculated using the Debye model and measured data. Relaxation times of 9.23, 8.30, 6.48, and 5.17 ps were used for liquid water at T = 20, 25, 35, and 45°C, respectively [36].

Wet soil samples were prepared by adding 10%, 20%, and 25% volume of moisture to the dry soil samples. Averaged values of permittivity for the different wet samples are tabulated in Table 2-2. Permittivity values versus frequency are presented in Figures 2-13, 2-14, and 2-15. Table 2-2 As expected, a reasonable increase in permittivity values is obtained as the water content of the sample increases. As shown in the following figures, measured results are in agreement with the model predicted values.

Table 2-2. Measured and calculated predicted values of permittivity of soil with different moisture content in a frequency range from 300 to 800 MHz. Predicted values of permittivity were obtained using the dielectric model for soils developed by Peplinski et al. [26].

Relative permittivity (Average)	Moisture Content		
	10%	20%	25%
Measured	6.9148-j0.0028	13.1200-j0.0680	17.2000-j0.0255
Calculated	6.9648-j0.0606	13.2700-j0.2038	16.8700-j0.2748
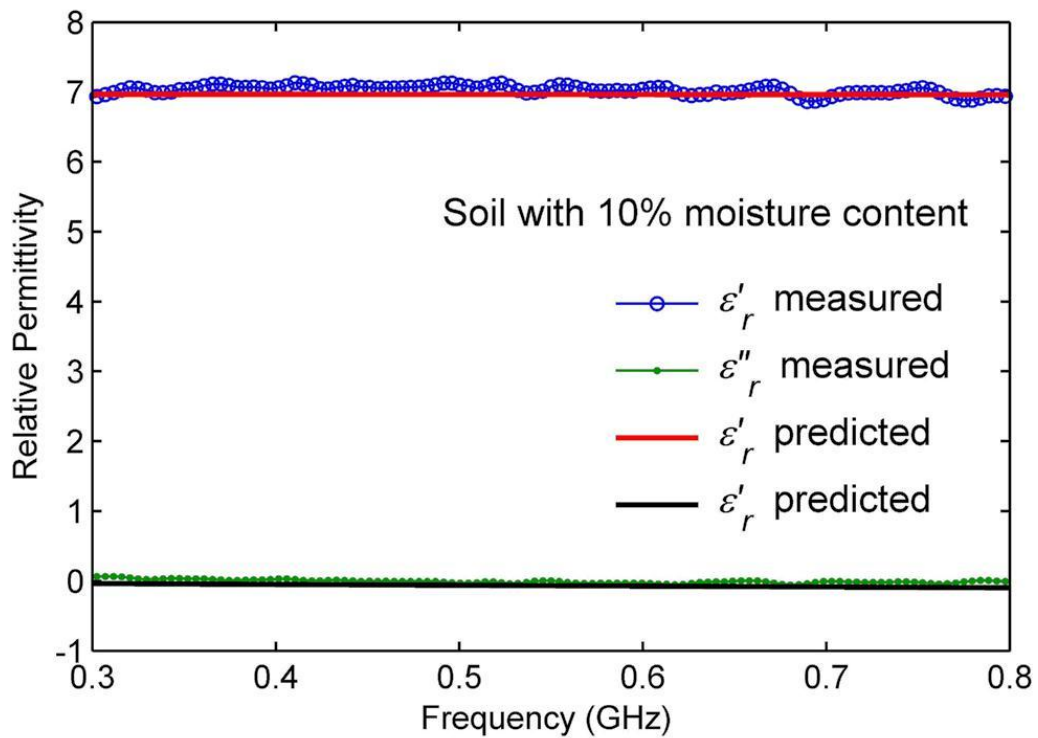
Figure 2-13. Complex relative permittivity of soil with 10% moisture content. Predicted values of permittivity were obtained using the dielectric model for soils developed by Peplinski *et al.* [26].
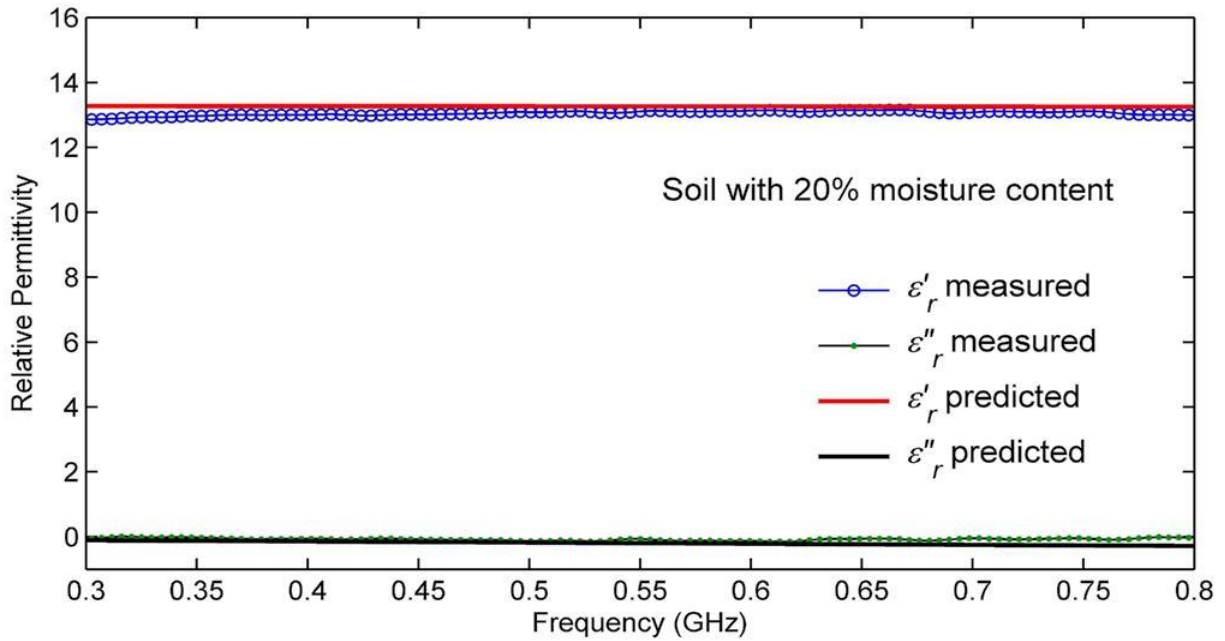
Figure 2-14. Complex relative permittivity of soil with 20% moisture content. Predicted values of permittivity were obtained using the dielectric model for soils developed by Peplinski *et al.* [26]
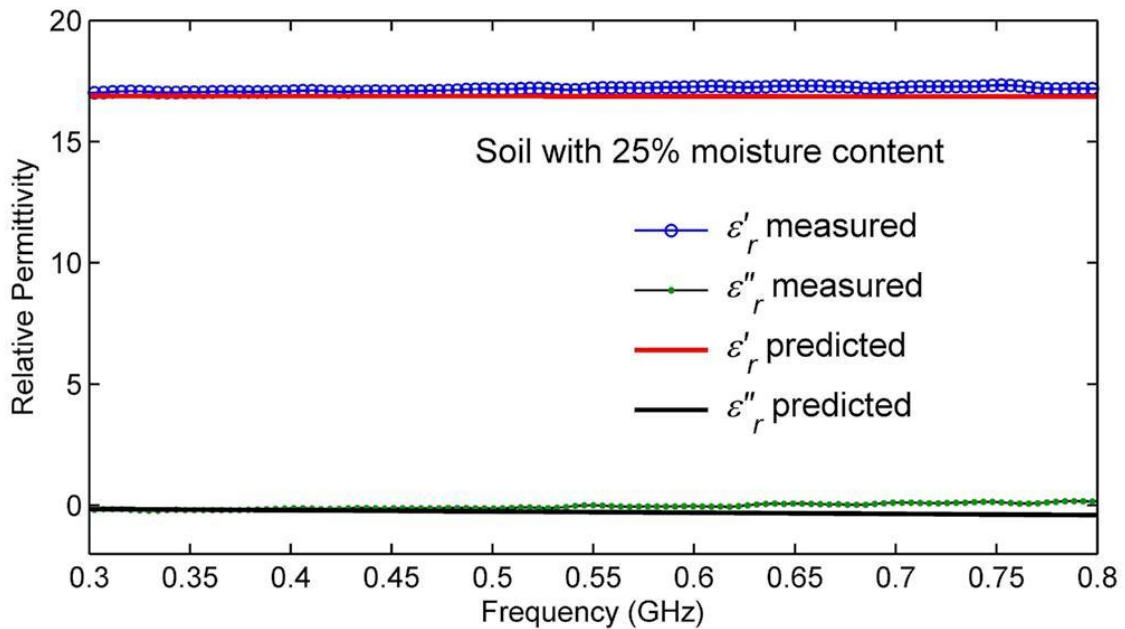
Figure 2-15. Complex relative permittivity of soil with 25% moisture content. Predicted values of permittivity were obtained using the dielectric model for soils developed by Peplinski *et al.* [26]

Next the permittivity value for contaminated soil was determined. Dry soil was polluted with a contaminant following the same procedure as with the wet soil samples. The contaminant used was motor oil SAE 30. This material was chosen as representative of hydrocarbons without having onerous material handling (e.g. safety) requirements. Dielectric properties of various petroleum oils were given by von Hippel [22]. Based on his data, the dielectric constant and loss tangent of motor oil used in this work were estimated using the following equations:

$$\varepsilon_r' = 2.24 - 0.000727T \tag{2.22}$$

$$\tan(\delta) = (0.527T + 4.82) \times 10^{-4} \tag{2.23}$$

where T is the temperature of the room in °C and tan(δ) is the loss tangent. For a room temperature of 22°C, the calculated relative permittivity of motor oil is $\varepsilon_r = 2.2236 - j0.0016$. Its permittivity value is close to the relative permittivity of dry soil. Therefore, not much change in permittivity was expected. Samples of dry soil with 25% volumetric oil content were measured. The results were compared with the predicted values calculated using the Maxwell Garnett mixing rule presented in [29]. Figure 2-16 shows the permittivity values obtained. There was insufficient difference in permittivity values to distinguish between dry and contaminated soil.
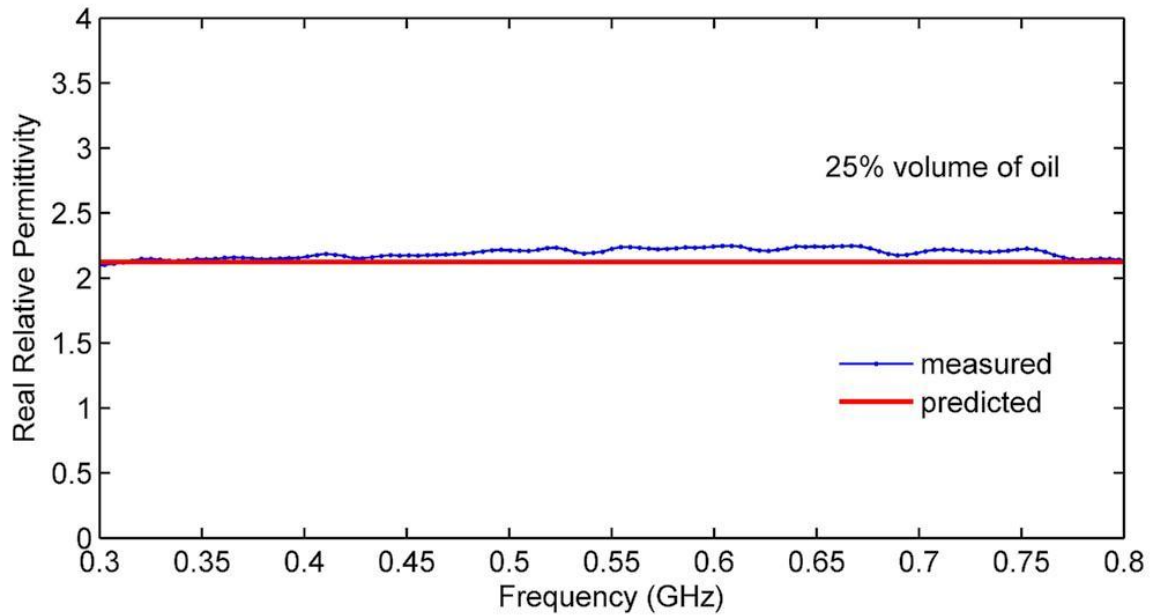
Figure 2-16. Real relative permittivity value for dry soil with 25% oil content. Predicted values of permittivity were obtained using the Maxwell Garnett mixing formula presented in [29].

Greater contrast should be observed, though, by considering soil with a higher water content per unit volume. This represents soil close to groundwater. General facts about groundwater can be found in [38]. The zone of soil above the water table is known as the unsaturated zone or the vadose zone. Soil particles in the unsaturated zone are coated with layers of water. No matter how tightly the soil particles are packed, there will always be void spaces between them. The void spaces between the soil particles are known as the soil pores. Below the water table the pore spaces are filled with water. Above the water table the pore spaces are filled with varied amounts of air and water. As contaminants move vertically through water-wet soil to the water table, it displaces the air and some of the water from the soil pores [39]. Soil particles remain wetted by water and the contaminant emerges as a dispersed phase. At a macro-scale, the oil does not appear to separate from the water due to the soil. After reaching the water table, the dissolved contaminant will move along with the groundwater in the direction of its hydraulic

gradient potentially causing contamination of wells [40]. To represent spills in the vadose zone, mixtures of 25% volume of oil and soil with 10% and 25% volumetric moisture content were simulated. Measured results were compared with the predicted values calculated using the mixing rules for moist and high-loss materials presented in [41]. Results are presented in Figure 2-17.
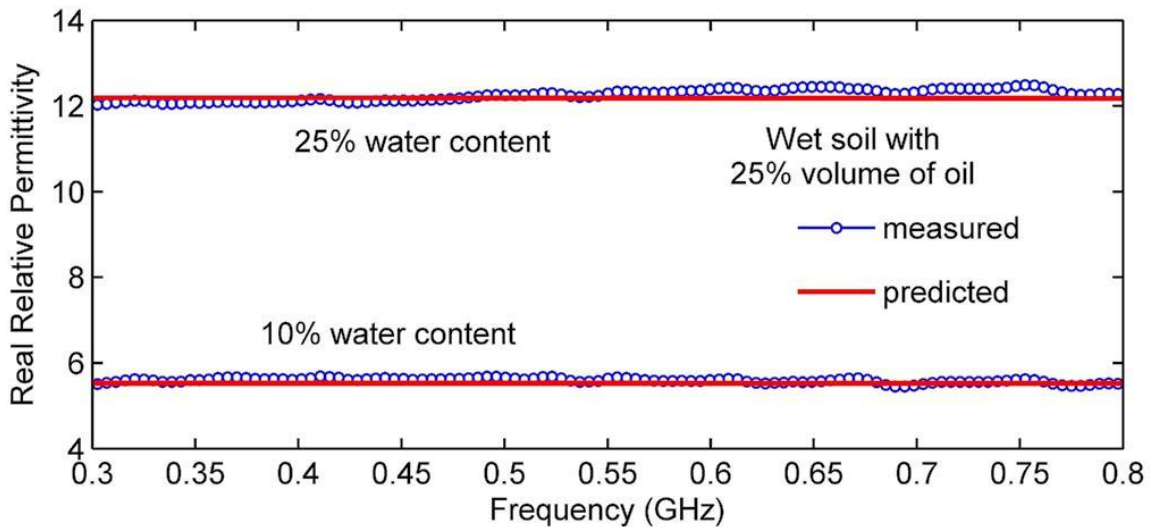
Figure 2-17. Results for a mixture of 25% volume of contaminant in soil with 10% and 25% volumetric moisture content. Measured results are compared with the predicted values calculated using the mixing rules for moist and high-loss materials presented in [41].

A significant difference, i.e. greater than the nominal uncertainty in the measured data, with regards to the permittivity values, was observed between the wet soil and wet soil with oil contamination. This is an indication that if wet soil is present, it will provide sufficient contrast to distinguish contaminated from uncontaminated soil.

As GPR signals travel through the soil, they are attenuated at a rate determined by the complex dielectric constant of the soil. The power attenuation in dB/m is given by

$$\text{Power Attenuation} = 8.6855 \frac{2\pi f}{c} \sqrt{\frac{\varepsilon'}{2}\left(\sqrt{1+\left(\frac{\varepsilon''}{\varepsilon'}\right)^2}-1\right)} \tag{2.24}$$

where c is the speed of light 2.997×10^8 m/s.

Figure 2-18 shows how changes in frequency relate to radar wave attenuation in different soils. As frequency increases, the attenuation of the GPR signals in both wet and contaminated soils increases rapidly. High frequency radar is often used to enhance resolution since resolution increases with frequency, but as shown in this figure, signal attenuation increases quite dramatically at higher frequencies.
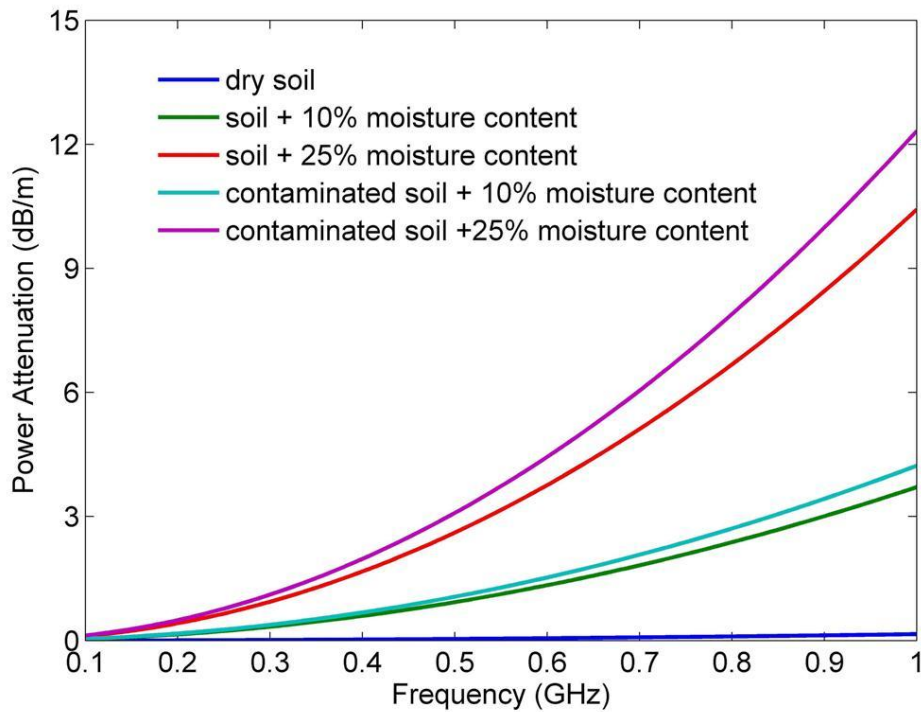
Figure 2-18. Power attenuation in dry, wet and contaminated soil in a frequency range of 100 MHz to 1 GHz.

The next chapter presents the analytical formulation of the algorithm used in the simulation of contaminants in soil using ground-truth obtained in these experiments.

CHAPTER 3

ANALYTICAL FORMULATION OF ELECTROMAGNETIC SCATTERING FROM AN UNDERGROUND HYDROCARBON SPILL

3.1   Introduction

Location and imaging of objects in the subsurface is an important engineering problem facilitating the design of systems utilized for the detection of mines, underground structures, pipelines, faults, waste pollution, etc. Among the techniques proposed for this purpose, those based on electromagnetic wave scattering are widely used [42]. Scattering from buried dielectric objects has been studied extensively by many researchers from the theoretical and numerical point of view during the past 4 decades.

Large volumes of hazardous liquids and fuels are stored worldwide in surface and underground tanks. Frequently, these tanks are found to leak resulting in loss of inventory and, more importantly, contamination to soil and groundwater. There are two methods for detecting leakage from tanks: monitoring the liquid level of fuel in the tank and monitoring the soil under the tanks for leaks. Chemical detection of leaks is very expensive, because it requires that hundreds of chemical sensors be placed around and underneath the tank to ensure reliable detection of the chemical spill [43]. Instead, borehole logging can be used to detect leaks in underground storage tanks and underground fuel transfer lines. Borehole logging is a nondestructive measuring technique and logistically simple and economical compared to other exploration methods [44]. Geophysical borehole logging involves gradually lowering a probe down a borehole, while the probe measures a physical property of the surrounding rock or soil.

Probes can be designed to measure any one of a variety of physical properties [45]. Since the measured physical property is related to the composition of the surrounding rocks and soils, borehole logs can be used to map the subsurface.

In this study, a simulated GPR borehole logging system was used as the method for detection. Figure 3-1 is a representation of a possible underground spill and borehole logging system. It is essential that the soil dielectric characteristics, presented in Chapter 2, are considered when analyzing the GPR response from dielectric targets. For the quantitative analysis of the subsurface, modeling of the electromagnetic interaction of the waves with the targets, is essential. Computational models provide basis for identifying target signal features and serve as the forward model for inversion analysis and reconstruction [42].
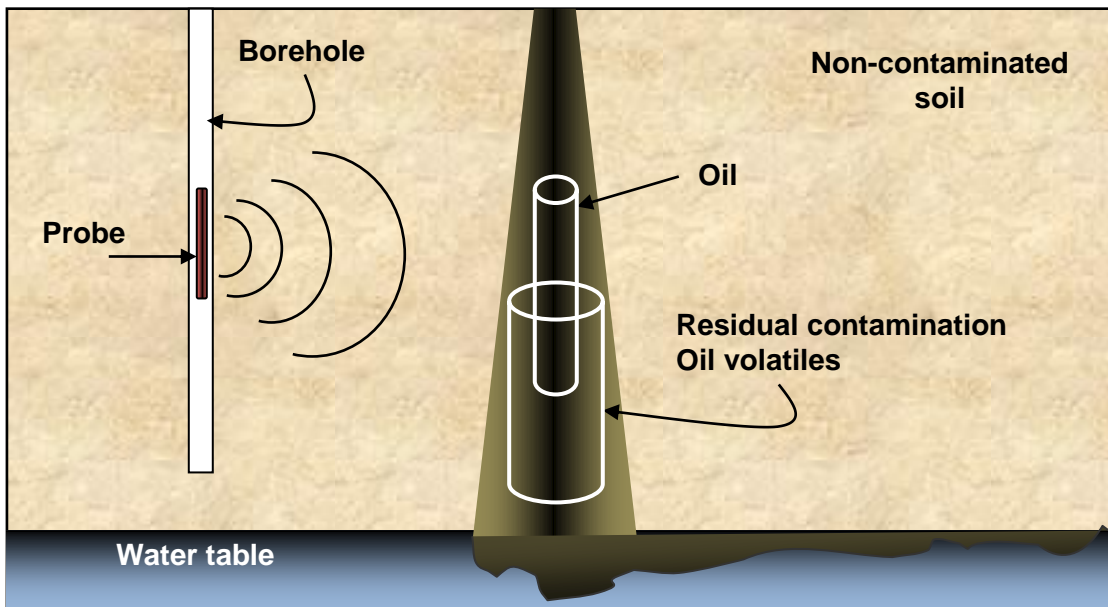
Figure 3-1. Schematic diagram of a possible underground spill and borehole logging system. For simplicity, the soil is modeled as a homogeneous dielectric space and the contaminated area is modeled as two eccentric, homogeneous circular cylinders.

In this chapter, solutions for scattering from a dielectric cylinder of infinite length (e.g. a two-dimensional, normal incidence scattering scenario) are reviewed. Values of permittivity obtained using the coaxial waveguide presented in Chapter 2 are used for a computer simulation of a contaminated underground system. For simplicity, the soil was modeled as a homogeneous dielectric space and the contaminated area was modeled as two eccentric, homogeneous circular cylinders as shown in Figure 3-2. Cylinders with different permittivities were considered to be sufficiently representative of a contaminated region for academic purposes.
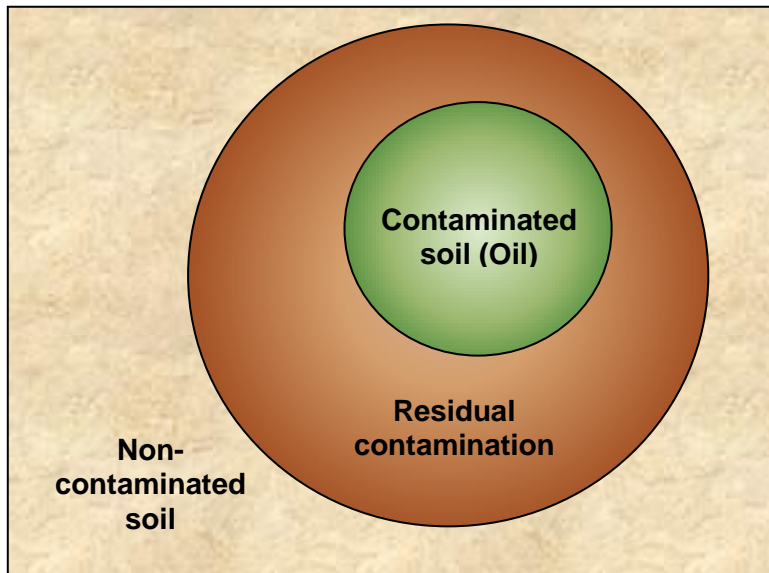
Figure 3-2. Cross-sectional view of the spill illustrated in Figure 3-1. The spill is modeled as an eccentric dielectric cylinder embedded in another dielectric cylinder. The non-contaminated soil is modeled as a homogeneous dielectric space

First, scattering equations from a homogeneous dielectric cylinder of infinite length immersed in a lossless homogeneous medium are presented. Convergence analysis and contrast analysis was performed to assure convergence of the Bessel and Hankel functions and scattering field intensity, respectively. Then, a system of eccentric cylinders is analyzed. The cylinders are assumed to be infinite in length and their axes are parallel to the z-direction. The system is

35

illuminated by a cylindrical wave from a line source of infinite extent located at $\left(\rho_0, \phi_0\right)$ in a direction parallel to the cylinder axis. Hence the incidence angle is normal rather than skew resulting in a non-depolarizing scattering scenario. Electromagnetic scattering from the cylinders is calculated using a boundary-value mode-matching approach presented by Kishk, Parrikar, and Elsherbeni in [46], called the KPE algorithm. The approach to the problem involves solving the scalar Helmholtz equation in cylindrical coordinates subject to the boundary conditions imposed by Maxwell's equations.

3.2   Scattering by dielectric objects

3.2.1   Normal incidence plane wave scattering by dielectric circular cylinder: fundamental theory.

Cylinders represent an important class of objects for GPR since they represent important environmental and engineering targets and also because their scattering properties are strongly polarization dependent [47]. Polarization in this context refers to the orientation of the electric field vectors. The electric field of a wave traveling in a direction normal to the z-axis can be described by two orthogonal components as given by [48] [49]:

$$E_x(z,t) = E_{x0}e^{-\alpha z}\cos\left(\omega t - \beta z - \phi_x\right) \tag{3.1}$$

$$E_y(z,t) = E_{y0}e^{-\alpha z}\cos\left(\omega t - \beta z - \phi_y\right) \tag{3.2}$$

where α represents the attenuation constant, β the phase constant, ω the angular frequency, ϕ the phase, and E_{x0} and E_{y0} are the maximum amplitudes of the E_x and E_y components, respectively.

Polarization vectors are chosen such that one vector is oriented along the long axis of the cylinder (E-parallel or transverse-magnetic (TM)) and the other vector oriented orthogonal to the long axis of the cylinder (E-perpendicular or transverse electric (TE)) as shown in Figure 3-3.
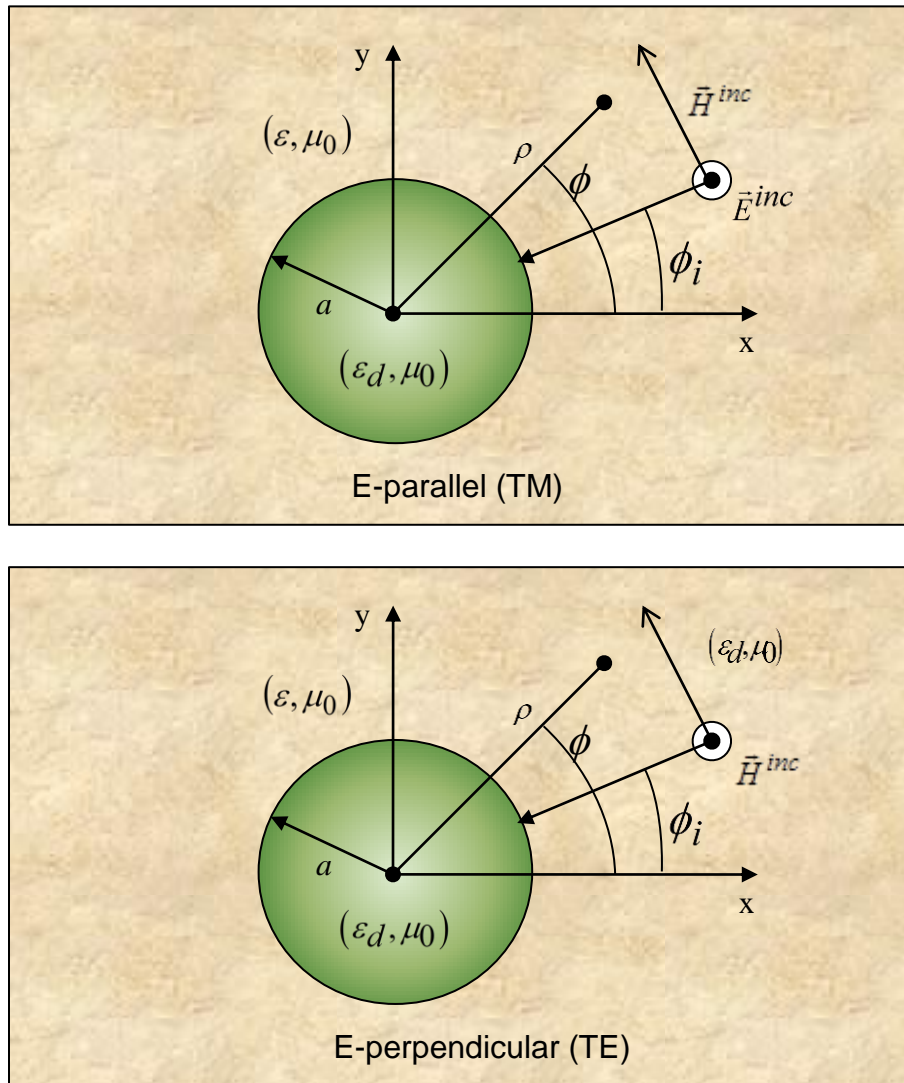
Figure 3-3. Definitions of E-parallel (TM) and E-perpendicular (TE) polarizations relative to a cylinder, as defined in [49]. TM polarization occurs when the electric field is parallel to the long axis of the cylinder. TE polarization occurs when the electric field is perpendicular to the long axis of the cylinder.

The scattered field is a function of the electrical properties of the cylinder and surrounding material, the distance from the cylinder, and the scattering angle ϕ, as defined in Figure 3-3. Since circular cylinders have a cylindrical shape, their scattering properties are conveniently described using Hankel and Bessel functions.

TM$_z$ polarization

A TM$_z$ uniform plane wave traveling in a medium with permittivity ε and permeability μ_0 is normally incident on a lossless dielectric circular cylinder of radius a, permittivity ε_d and permeability μ_0 as illustrated in Figure 3-3. The time dependence $e^{-j\omega t}$ is implied and suppressed throughout the derivation. The incident field $\vec{E}^i$ can be expressed as

$$\vec{E}^i = \hat{a}_z E_z^i = \hat{a}_z E_0 e^{jk_0\left(x\cos\phi_i + y\sin\phi_i\right)} = \hat{a}_z E_0 e^{jk_0\rho\left(\cos\phi\cos\phi_i + \sin\phi\sin\phi_i\right)}$$

$$= \hat{a}_z E_0 e^{jk_0\rho\cos\left(\phi-\phi_i\right)}$$

(3.3)

where E_0 is the amplitude of the incident wave, $k_0 = \omega\sqrt{\varepsilon\cdot\mu_0}$ is the wavenumber in the incident medium, ϕ_i is the incident angle, ϕ is the observation angle, and ρ is the observation distance. Using wave transformation from Cartesian to cylindrical coordinates [48],

$$e^{jx} = e^{j\rho\cos\phi} = \sum_{n=-\infty}^{\infty} j^n J_n(\rho)e^{jn\phi}$$

(3.4)

where $J_n(\cdot)$ is the Bessel function of the first kind of order n. The incident electric field can be expressed as

$$E_z^i = E_0 \sum_{n=-\infty}^{\infty} j^n J_n(k_0 \rho) e^{jn(\phi - \phi_i)} \tag{3.5}$$

The total field in the incident medium is the sum of the incident and the scattered fields, that is,

$$\vec{E} = \vec{E}^i + \vec{E}^S = \hat{z}(E_z^i + E_z^S) \tag{3.6}$$

The scattered field $\vec{E}_s$ can be represented by

$$E_z^S = \begin{cases} E_0 \sum_{n=-\infty}^{\infty} j^n a_n H_n^{(2)}(k_0 \rho) e^{jn(\phi - \phi_i)} & , \rho > a \\ \\ E_0 \sum_{n=-\infty}^{\infty} j^n c_n J_n(k_d \rho) e^{jn(\phi - \phi_i)} & , \rho < a \end{cases} \tag{3.7}$$

where a_n and c_n are unknown amplitude coefficients, $H_n^{(2)}(\cdot)$ is the Hankel function of the second kind of integer order n, and $k_d = \omega \sqrt{\varepsilon_d \mu_0}$ is the wavenumber inside the dielectric. These unknown amplitude coefficients can be found by applying the following boundary conditions at $\rho = a$:

$$E_z^i + E_z^{ref} = E_z^{tran} \tag{3.8}$$

$$H_\phi^i + H_\phi^{ref} = H_\phi^{tran} \tag{3.9}$$

For the electric field, using equations (3-3) and (3-5) into equation (3-6) we obtain

$$E^{tran} = E_0 \sum_{n=-\infty}^{\infty} j^n \left[J_n(k_0 a) + a_n H_n^{(2)}(k_0 a) \right] e^{jn(\phi - \phi_i)} \tag{3.10}$$

Simplifying and solving for c_n,

$$E_0 \sum_{n=-\infty}^{\infty} j^n c_n J_n(k_d a) \, e^{jn(\phi-\phi_i)} = E_0 \sum_{n=-\infty}^{\infty} j^n \left[J_n(k_0 a) + a_n H_n^{(2)}(k_0 a) \right] e^{jn(\phi-\phi_i)}$$

$$c_n J_n(k_d a) = J_n(k_0 a) + a_n H_n^{(2)}(k_0 a)$$

$$c_n = \frac{J_n(k_0 a) + a_n H_n^{(2)}(k_0 a)}{J_n(k_d a)} \tag{3.11}$$

Now, for the boundary condition for the magnetic field, $H_\phi^i + H_\phi^{ref} = H_\phi^{tran}$, we need to find

the H-field in each region. Using Faraday's equation

$$\vec{H} = -\frac{1}{j\omega\mu} \nabla \times \vec{E} = -\frac{1}{j\omega\mu} \left(\hat{a}_\rho \frac{1}{\rho} \frac{\partial \vec{E}}{\partial \phi} - \hat{a}_\phi \frac{\partial \vec{E}}{\partial \rho} \right) \tag{3.12}$$

$$H_\rho = -\frac{1}{j\omega\mu} \left[\hat{a}_\rho \frac{\partial \vec{E}}{\partial \phi} \right] \tag{3.13}$$

$$H_\phi = -\frac{1}{j\omega\mu} \left[-\hat{a}_\phi \frac{\partial E}{\partial \rho} \right] = \frac{1}{j\omega\mu} \frac{\partial E_z}{\partial \rho} \tag{3.14}$$

$$H_\phi^i = \frac{k_0 E_0}{j\omega\mu} \sum_{n=-\infty}^{\infty} j^n J_n'(k_0 \rho) e^{jn(\phi-\phi_i)} \tag{3.15}$$

$$H_\phi^{ref} = \frac{k_0 E_0}{j\omega\mu} \sum_{n=-\infty}^{\infty} j^n a_n H_n^{(2)'}(k_0 \rho) e^{jn(\phi-\phi_i)} \tag{3.16}$$

$$H_\phi^{tran} = \frac{k_d E_0}{j\omega\mu} \sum_{n=-\infty}^{\infty} j^n C_n J_n'(k_d \rho) e^{jn(\phi-\phi_i)} \tag{3.17}$$

where $J_n'(\cdot)$ is the derivative of the Bessel function of the first kind of order n and $H_n^{(2)\prime}(\cdot)$ is the derivative of the Hankel function of the second kind of integer order n. At the boundary of the cylinder ($\rho = a$) the total tangential magnetic field can be written as

$$\frac{k_0 E_0}{j\omega\mu} \sum_{n=-\infty}^{\infty} j^n \left[J_n'(k_0 a) + a_n H_n^{(2)\prime}(k_0 a) \right] e^{jn(\phi - \phi_i)} = \frac{k_d E_0}{j\omega\mu} \sum_{n=-\infty}^{\infty} j^n c_n J_n'(k_d a) e^{jn(\phi - \phi_i)}$$

Simplifying,

$$\sqrt{\varepsilon} \left[J_n'(k_0 a) + a_n H_n^{(2)\prime}(k_0 a) \right] = \sqrt{\varepsilon_d}\, c_n J_n'(k_d a)$$

$$\left[J_n'(k_0 a) + a_n H_n^{(2)\prime}(k_0 a) \right] = \sqrt{\varepsilon_d / \varepsilon}\, c_n J_n'(k_d a) \tag{3.18}$$

Using equation (3-9) and defining $\varepsilon_c = \varepsilon_d / \varepsilon$ as the contrast ratio of the permittivity of the dielectric and the permittivity of the medium,

$$J_n'(k_0 a) + a_n H_n^{(2)\prime}(k_0 a) = \sqrt{\varepsilon_d / \varepsilon} \left[\frac{J_n(k_0 a) + a_n H_n^{(2)}(k_0 a)}{J_n(k_d a)} \right] J_n'(k_d a)$$

$$J_n'(k_0 a) + a_n H_n^{(2)\prime}(k_0 a) = \sqrt{\varepsilon_c} \left[\frac{J_n(k_0 a) J_n'(k_d a) + a_n H_n^{(2)}(k_0 a) J_n'(k_d a)}{J_n(k_d a)} \right]$$

$$a_n H_n^{(2)\prime}(k_0 a) - \frac{\sqrt{\varepsilon_c}\, a_n H_n^{(2)}(k_0 a) J_n'(k_d a)}{J_n(k_d a)} = \frac{\sqrt{\varepsilon_c}\, J_n(k_0 a) J_n'(k_d a)}{J_n(k_d a)} - J_n'(k_0 a)$$

$$a_n \left[\frac{H_n^{(2)\prime}(k_0 a) J_n(k_d a) - \sqrt{\varepsilon_c}\, H_n^{(2)}(k_0 a) J_n'(\beta_d a)}{J_n(k_d a)} \right] =$$

$$\frac{\sqrt{\varepsilon_c}\, J_n(k_0 a) J_n'(k_d a) - J_n'(k_0 a) J_n(k_d a)}{J_n(k_d a)}$$

$$a_n = \frac{\sqrt{\varepsilon_c} J_n(k_0 a) J_n'(k_d a) - J_n'(k_0 a) J_n(k_d a)}{H_n^{(2)'}(k_0 a) J_n(k_d a) - \sqrt{\varepsilon_c} H_n^{(2)}(k_0 a) J_n'(k_d a)} \tag{3.19}$$

Substituting equation (3-17) into equation (3-9) we obtain

$$c_n = \frac{J_n(k_0 a)}{J_n(k_d a)} + \frac{H_n^{(2)}(k_0 a)}{J_n(k_d a)}\left[\frac{\sqrt{\varepsilon_c} J_n(k_0 a) J_n'(k_d a) - J_n'(k_0 a) J_n(k_d a)}{H_n^{(2)'}(k_0 a) J_n(k_d a) - \sqrt{\varepsilon_c} H_n^{(2)}(k_0 a) J_n'(k_d a)}\right]$$

$$= \frac{J_n(k_0 a) + \left[\dfrac{\sqrt{\varepsilon_c} J_n(k_0 a) J_n'(k_d a) - J_n'(k_0 a) J_n(k_d a)}{H_n^{(2)'}(k_0 a) J_n(k_d a) - \sqrt{\varepsilon_c} H_n^{(2)}(k_0 a) J_n'(k_d a)}\right] H_n^{(2)}(k_0 a)}{J_n(k_d a)}$$

$$= \frac{J_n(k_0 a) + \left[\dfrac{\sqrt{\varepsilon_c} H_n^{(2)}(k_0 a) J_n(k_0 a) J_n'(k_d a) - H_n^{(2)}(k_0 a) J_n'(k_0 a) J_n(k_d a)}{H_n^{(2)'}(k_0 a) J_n(k_d a) - \sqrt{\varepsilon_c} H_n^{(2)}(k_0 a) J_n'(k_d a)}\right]}{J_n(k_d a)}$$

$$c_n = \frac{J_n(k_0 a) H_n^{(2)'}(k_0 a) - H_n^{(2)}(k_0 a) J_n'(k_0 a)}{H_n^{(2)'}(k_0 a) J_n(k_d a) - \sqrt{\varepsilon_c} H_n^{(2)}(k_0 a) J_n'(k_d a)} \tag{3.20}$$

For the TM polarization normally incident on a dielectric cylinder, the scattering field is given by:

$$E_z^s = E_0 \sum_{n=-\infty}^{\infty} j^n \frac{\sqrt{\varepsilon_c} J_n(k_0 a) J_n'(k_d a) - J_n'(k_0 a) J_n(k_d a)}{H_n^{(2)'}(k_0 a) J_n(k_d a) - \sqrt{\varepsilon_c} H_n^{(2)}(k_0 a) J_n'(k_d a)}$$
$$\times H_n^{(2)}(k_0 \rho) e^{jn(\phi - \phi_i)} \tag{3.21}$$

To obtain the scattered field in the far-zone, the asymptotic expansion for large argument of the Hankel function is used [49], [50].

$$H_n^{(2)}(k_0 \rho) \overset{k_0 \rho \to \infty}{\cong} \sqrt{\frac{2j}{\pi k_0 \rho}} j^n e^{-jk_0 \rho} \tag{3.22}$$

From equation (3-5), the reflected field is

$$E_z^{ref} = E_0 \sum_{n=-\infty}^{\infty} j^n a_n H_n^{(2)}(k_0\rho)e^{jn(\phi-\phi_i)}$$

$$= -E_0 \sum_{n=-\infty}^{\infty} j^{-n} a_n H_n^{(2)}(k_0\rho)e^{jn(\phi-\phi_i)} \qquad (3.23)$$

Therefore, the far-zone approximation of the scattered field is given by

$$E_z^s = -E_0 \sqrt{\frac{2j}{\pi k_0\rho}} e^{-jk_0\rho} \sum_{n=-\infty}^{\infty} a_n e^{jn(\phi-\phi_i)} \qquad (3.24)$$

TE$_z$ polarization

The previous analysis is repeated for a TE$_z$ plane wave normally incident on a dielectric cylinder of radius a, permittivity ε_d and permeability μ_0 as shown in Figure 3-3. The TE polarization case is expressed in terms of magnetic fields for convenience and one may convert between electric and magnetic fields using Ampere's and Faraday's laws. The incident magnetic field can be written as

$$\vec{H}^i = \hat{a}_z H_0 e^{jk_0(x\cos\phi_i + y\sin\phi_i)} = \hat{a}_z H_0 \sum_{n=-\infty}^{\infty} j^n J_n(k_0\rho)e^{jn(\phi-\phi_i)} \qquad (3.25)$$

The corresponding incident electric field can be obtained by using Ampere's law, which reduces to

$$\vec{E}^i = \frac{1}{j\omega\varepsilon}\nabla \times \vec{H}^i = \frac{1}{j\omega\varepsilon}\left[\vec{a}_\rho \frac{1}{\rho}\frac{\partial H_z^i}{\partial \phi} - \vec{a}_\phi \frac{\partial H_z^i}{\partial \rho}\right] \qquad (3.26)$$

The components of the electric field are

43

$$\vec{E}_\rho^i = \frac{1}{j\omega\varepsilon}\frac{1}{\rho}\frac{\partial H_z^i}{\partial \phi} = \frac{H_0}{j\omega\varepsilon}\frac{1}{\rho}\sum_{n=-\infty}^{\infty} nj^{n+1}J_n(k_0\rho)e^{jn(\phi-\phi_i)} \qquad (3.27)$$

$$E_\phi^i = -\frac{1}{j\omega\varepsilon}\frac{\partial H_z^i}{\partial \rho} = -\frac{k_0 H_0}{j\omega\varepsilon}\sum_{n=-\infty}^{\infty} j^n J_n'(k_0\rho)e^{jn(\phi-\phi_i)} \qquad (3.28)$$

The scattered magnetic field has a similar form to that of the scattered electric field of equation

(3-5) for the TM$_z$ polarization. It can be written as

$$\vec{H}^s = \hat{a}_z H_z^s = \hat{a}_z H_0 \sum_{n=-\infty}^{\infty} d_n H_n^{(2)}(k_0\rho)e^{jn(\phi-\phi_i)} \qquad (3.29)$$

where d_n represents the unknown amplitude coefficient. The scattered electric fields are

$$E_\rho^s = \frac{1}{j\omega\varepsilon}\frac{1}{\rho}\frac{\partial H_z^s}{\partial \phi} = \frac{H_0}{j\omega\varepsilon}\frac{1}{\rho}\sum_{n=-\infty}^{\infty} nj H_n^{(2)}(k_0\rho)d_n e^{jn(\phi-\phi_i)} \qquad (3.30)$$

$$E_\phi^s = \frac{1}{j\omega\varepsilon}\frac{\partial H_z^s}{\partial \rho} = -\frac{k_0 H_0}{j\omega\varepsilon}\sum_{n=-\infty}^{\infty} d_n H_n^{(2)'}(k_0\rho)e^{jn(\phi-\phi_i)} \qquad (3.31)$$

Applying boundary conditions at $\rho = a$

$$E_\phi^i + E_\phi^{ref} = E_\phi^{tran} \qquad (3.32)$$

$$E_\rho^i + E_\rho^{ref} = E_\rho^{tran} \qquad (3.33)$$

$$H_z^i + H_z^{ref} = H_z^{tran} \qquad (3.34)$$

Solving for the ϕ component of the electric field

$$E_\phi^{tran} = -\frac{k_0 H_0}{j\omega\varepsilon} \sum_{n=-\infty}^{\infty} \left[j^n J_n'(k_0 a) e^{jn(\phi-\phi_i)} + d_n H_n^{(2)'}(k_0 a) e^{jn(\phi-\phi_i)} \right]$$

Simplifying,

$$\frac{-k_d H_0}{j\omega\varepsilon} \sum_{n=-\infty}^{\infty} j^n C_n J_n'(k_d a) e^{jn(\phi-\phi_i)} = -\frac{k_0 H_0}{j\omega\varepsilon} \sum \left[j^n J_n'(k_0 a) + d_n H_n^{(2)'}(k_0 a) e^{jn(\phi-\phi_i)} \right]$$

$$\frac{k_d}{\varepsilon_d} C_n J_n'(k_d a) = \frac{k_0}{\varepsilon} \left[J_n'(k_0 a) + d_n H_n^{(2)'}(k_0 a) \right]$$

$$C_n = \frac{k_0 \varepsilon_d}{k_d \varepsilon} \left[\frac{J_n'(k_0 a) + d_n H_n^{(2)'}(k_0 a)}{J_n'(k_d a)} \right]$$

$$C_n = \sqrt{\varepsilon_c} \left[\frac{J_n'(k_0 a) + d_n H_n^{(2)'}(k_0 a)}{J_n'(k_d a)} \right] \tag{3.35}$$

Applying the third boundary condition for the magnetic field $H_z^i + H_z^{ref} = H_z^{tran}$ and solving

for d_n,

$$H_z^{tran} = H_0 \sum_{n=-\infty}^{\infty} j^n J_n(k_0 a) e^{jn(\phi-\phi_i)} + H_0 \sum_{n=-\infty}^{\infty} j^n d_n H_n^{(2)}(k_0 a) e^{jn(\phi-\phi_i)}$$

$$H_0 \sum_{n=-\infty}^{\infty} C_n J_n(k_0 a) e^{jn(\phi-\phi_i)} = H_0 \sum_{n=-\infty}^{\infty} \left[j^n J_n(k_0 a) + j^n d_n H_n^{(2)}(k_0 a) \right] e^{jn(\phi-\phi_i)}$$

$$C_n J_n(k_d a) = J_n(k_0 a) + d_n H_n^{(2)}(k_0 a)$$

$$\sqrt{\varepsilon_c} \left[\frac{J_n'(k_0 a) + d_n H_n^{(2)'}(k_0 a)}{J_n'(k_d a)} \right] J_n(k_d a) = J_n(k_0 a) + d_n H_n^{(2)}(k_0 a)$$

$$\sqrt{\varepsilon_c}\, J_n'\left(k_0 a\right) J_n\left(k_d a\right) + d_n \sqrt{\varepsilon_c}\, H_n^{(2)'}\left(k_0 a\right) J_n\left(k_d a\right) =$$

$$J_n'\left(k_d a\right) J_n\left(k_0 a\right) + d_n J_n'\left(k_0 a\right) H_n^{(2)}\left(k_0 a\right)$$

$$d_n\left[\sqrt{\varepsilon_c}\, H_n^{(2)'}\left(k_0 a\right) J_n\left(k_d a\right) - J_n'\left(k_d a\right) H_n^{(2)}\left(k_0 a\right)\right] =$$

$$J_n'\left(k_d a\right) J_n\left(k_0 a\right) - \sqrt{\varepsilon_c}\, J_n'\left(k_0 a\right) J_n\left(k_d a\right)$$

$$d_n = \frac{J_n'\left(k_d a\right) J_n\left(k_0 a\right) - \sqrt{\varepsilon_c}\, J_n'\left(k_0 a\right) J_n\left(k_d a\right)}{\sqrt{\varepsilon_c}\, H_n^{(2)'}\left(k_0 a\right) J_n\left(k_d a\right) - J_n'\left(k_d a\right) H_n^{(2)}\left(k_0 a\right)} \tag{3.36}$$

For TE_z polarization, the scattered electric field can be summarize as

$$\vec{E}_s = \hat{\rho} E_\rho + \hat{\phi} E_\phi \tag{3.37}$$

where

$$E_\rho^s = \frac{E_0}{j\omega\varepsilon\eta} \frac{1}{\rho} \sum_{n=-\infty}^{\infty} n j d_n H_n^{(2)}\left(k_0\rho\right) e^{jn\left(\phi-\phi_i\right)} \tag{3.38}$$

$$E_\phi^s = -\frac{k_0 E_0}{j\omega\varepsilon\eta} \sum_{n=-\infty}^{\infty} d_n H_n^{(2)'}\left(k_0\rho\right) e^{jn\left(\phi-\phi_i\right)} \tag{3.39}$$

and $\eta = \sqrt{\dfrac{\mu_0}{\varepsilon}}$ is the intrinsic impedance of the incident medium. Field equations for both, TM and TE polarizations are expressed in terms of Bessel and Hankel functions. Before performing any calculations, we need to analyze the convergence of the series. The magnitude of the bistatic field for TM_z and TE_z polarization was calculated for various numbers of terms in the series expansion. The series was truncated when the percent difference between the results of consecutive modes was less than 0.01%. Results are shown in Figure 3-4.
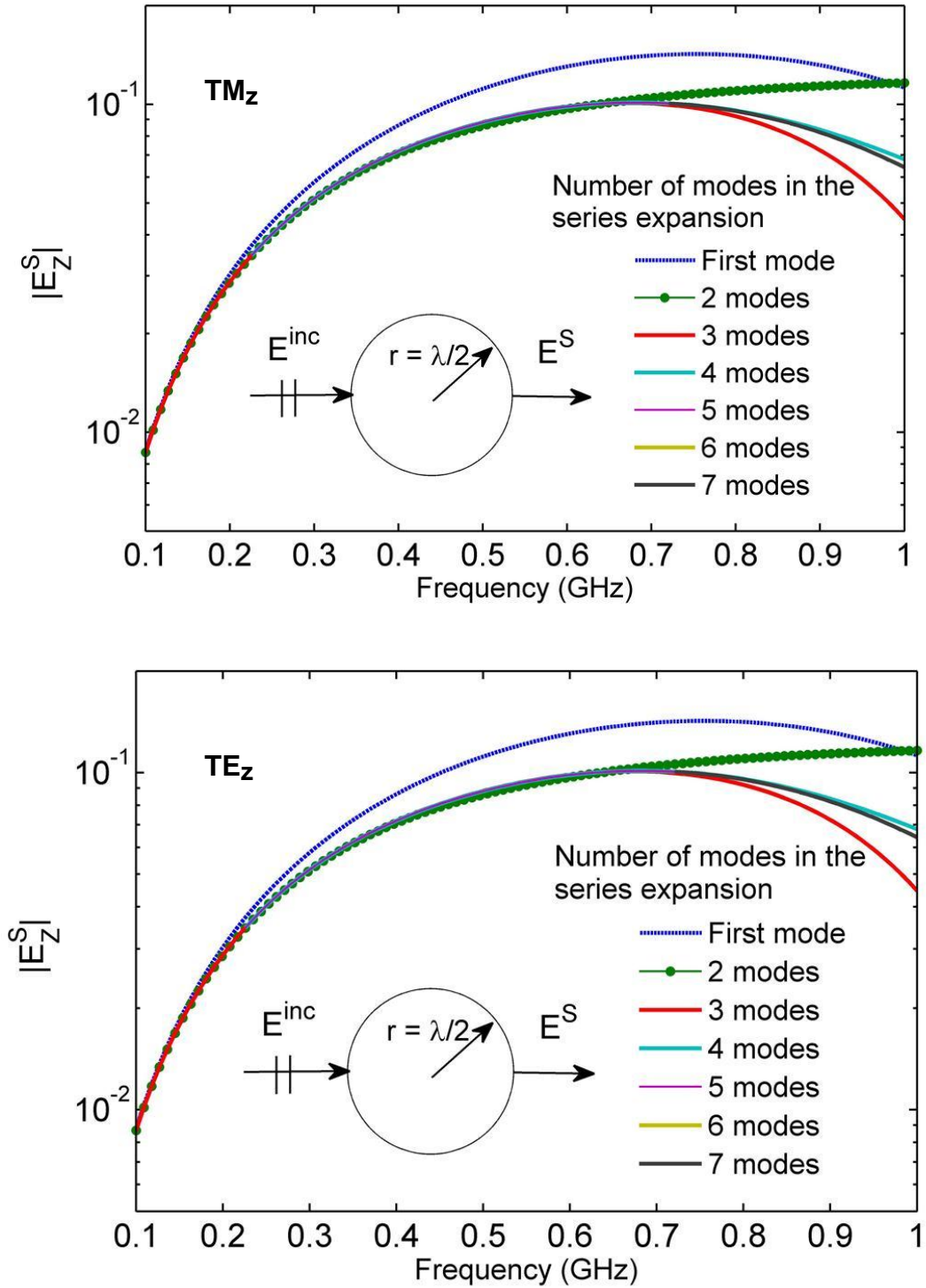
Figure 3-4. Magnitude of the bistatic scattering field for a dielectric cylinder with radius $\lambda/2$, surrounded by wet soil. Different numbers of modes were used to calculate the scattering field and analyze the convergence of the series expansion. The series was truncated when the percent difference between the results of consecutive modes was less than 0.01%.

Results for both polarizations showed that the required number of terms N in the series is approximately $N = 2k_0 r$, where k_0 is the wavenumber in the surrounding medium and r is the radius of the dielectric cylinder.

Scattering width

The radar cross-section (RCS) represents a convenient way to describe the strength of scattered fields observed in the far-field. The RCS is defined as the area intercepting the amount of power that when scattered isotropically, produces at the receiver a density that is equal to the density scattered by the actual target [51]. For 2D objects such as an infinite cylinder, the RCS is represented by the scattering width (SW) or alternatively the RCS per unit length [49].

$$SW = \lim_{r \to \infty} 2\pi r \frac{\left|E^s\right|^2}{\left|E^i\right|^2} \tag{3.40}$$

Most GPR surveys used to image the subsurface are conducted in common-offset mode using closely spaced antennas [52]. This results in a bistatic angle of approximately $0°$ (backscattered), depending on antenna separation and target depth. It is thus important to further investigate backscattered scattering widths as a function of cylinder radius. TM_z and TE_z scattering widths were calculated for the case of a dielectric cylinder with relative permittivity of 2.22 surrounded by a medium with permittivity of 17.0. This represents targets like hydrocarbons surrounded by wet loamy soil. Figure 3-5 illustrates backscattering width as a function of radius for TM and TE polarization for the intended target. The results show that, for small cylinders immersed in the intended higher permittivity medium, TM backscattering widths are greater than TE backscattering widths for most radii considered herein.
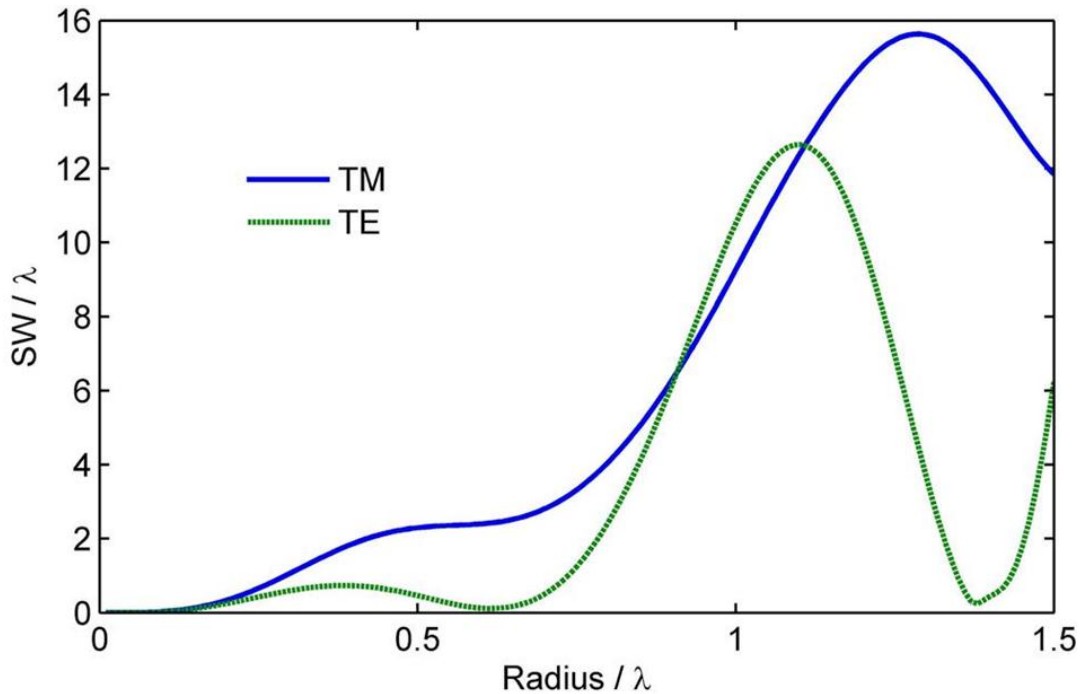
Figure 3-5. Backscattering widths as a function of radius, normalized by the wavelength (λ) of the incident field. TM backscattering widths are greater than TE backscattering widths for most cylinders.

Several features are observed in the scattering widths as a function of scattering angle for dielectric cylinders. As the radius of the cylinder becomes small compared to wavelength the scattering width amplitude oscillates less as one would expect since the contributions to the scattered field at any given observation angle has less phase difference (e.g. in the limit, all of the scattered field contributions emanate from the same point in space). The TM polarization scattering widths become nearly constant as a function of scattering angle. This is illustrated in Figure 3-6.
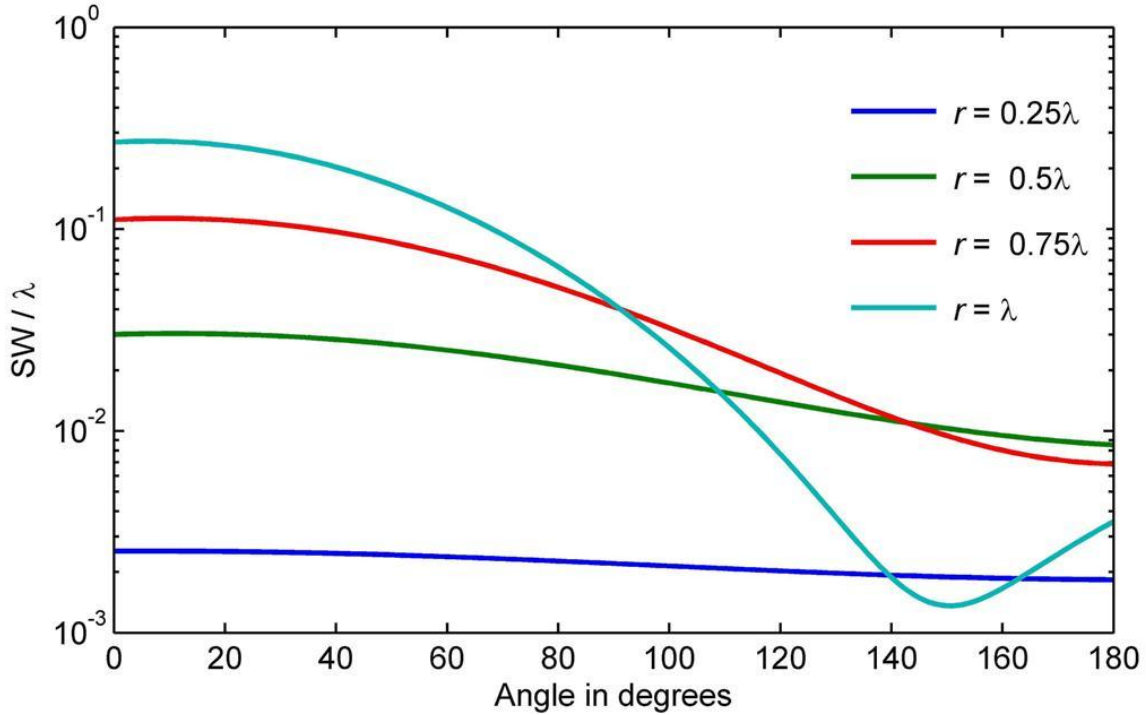
Figure 3-6. Scattering widths for high contrast dielectric cylinders, normalized by the wavelength (λ) of the incident field. As the radius of the cylinder becomes small compared to wavelength, TM scattering widths become nearly constant as a function of scattering angle.

Figure 3-7 shows the scattering width as a function of frequency for cylinders of different radii. The radii are varied from 0.05λ to λ at the highest frequency. The scattering width increases as the frequency increases for both, forward- and backscattering. Also, as the radius of the cylinder increases, more oscillations appear in the scattering width amplitudes.
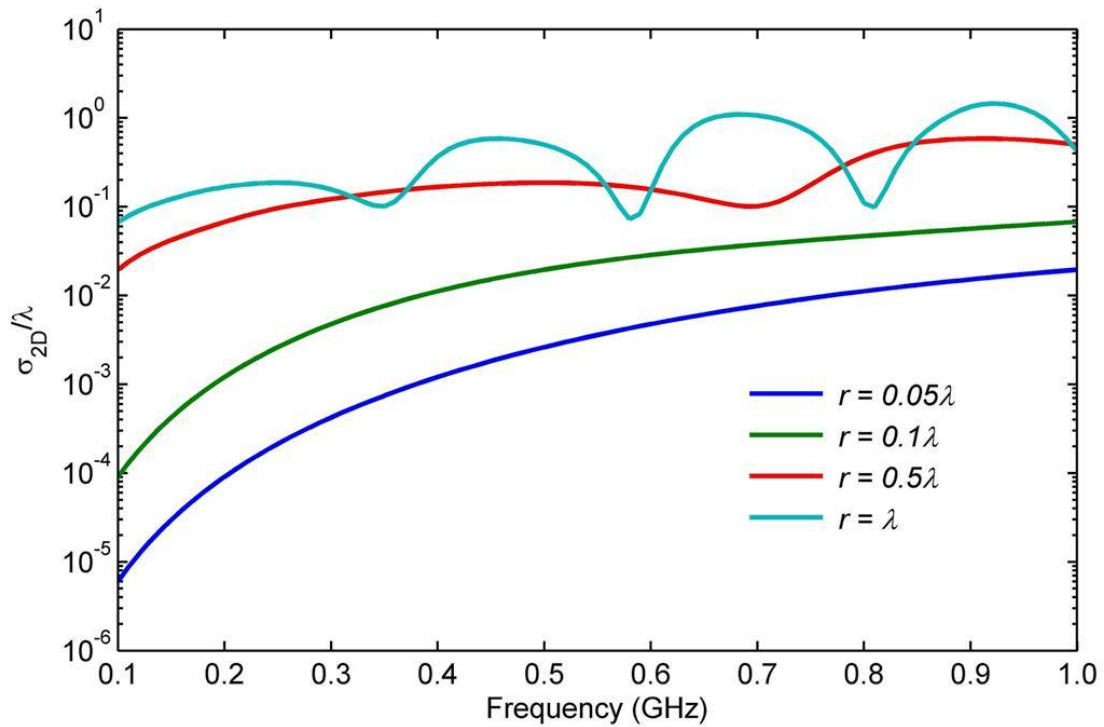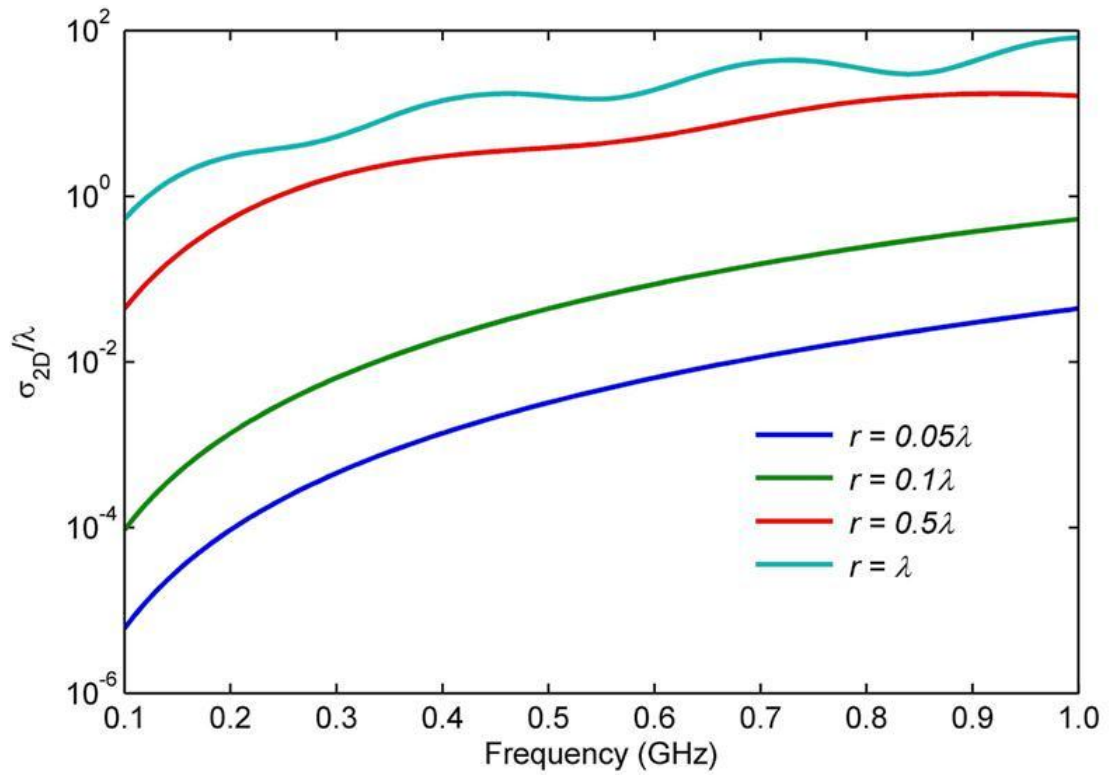
Figure 3-7. Scattering width as a function of frequency for cylinders of different radii. The radii are varied from 0.05λ to λ at the highest frequency. Forward (top) and back (bottom) scattering widths are illustrated.

The scattering width can also be plotted as a function of the contrast ratio ε_C as shown in Figure 3-8. The response is similar for high- and low-impedance dielectric cylinders. As the size of the cylinder increases, oscillations in the scattering width response increases. Also, if the contrast ratio approaches unity, the scattered fields will vanish, as expected.
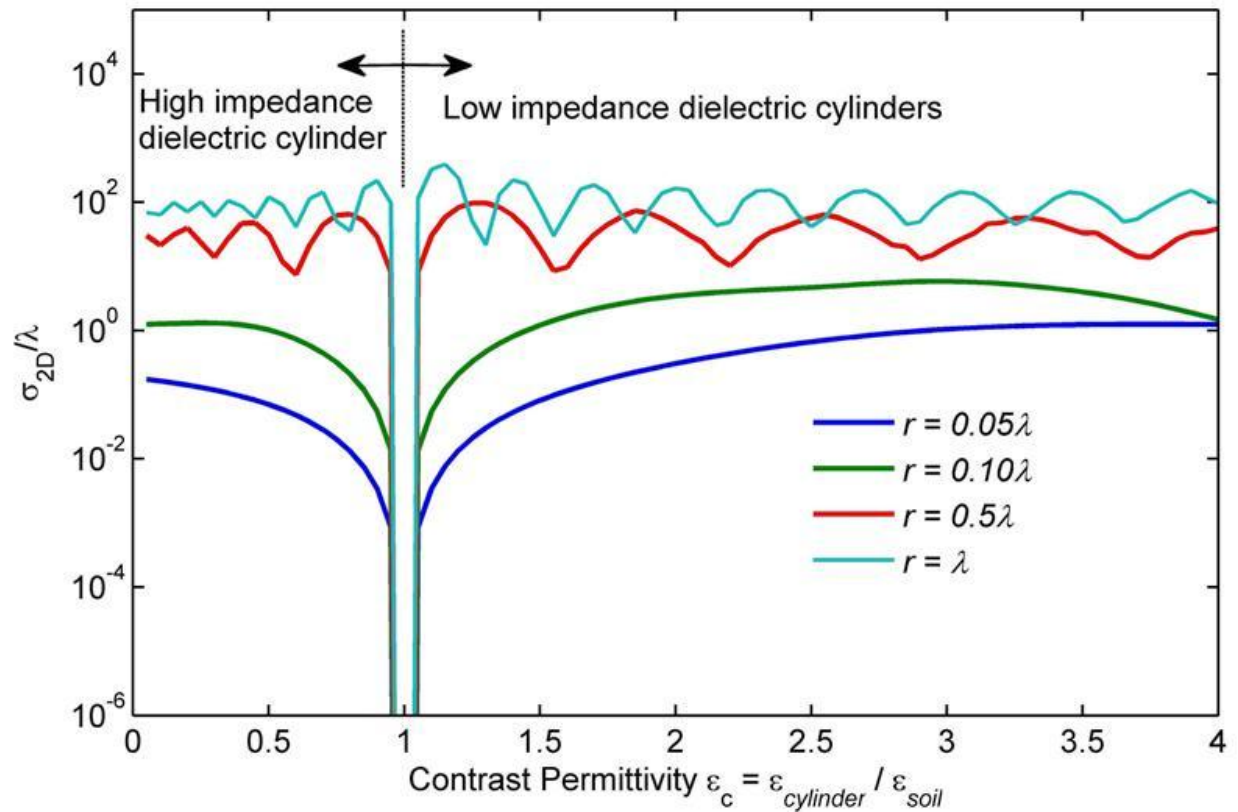
Figure 3-8. Scattering width as a function of the contrast ratio ε_C. Similar response is obtained for high- and low-impedance dielectric cylinders.

3.2.2 Layered dielectric cylinders: theory and analytical solutions

In this section, the equations needed for the calculation of the scattering field from an inhomogeneous spill are derived. The scattering field is calculated using a boundary-value mode-

matching approach presented by Kishk, Parrikar, and Elsherbeni in [46], called the KPE algorithm. The spill is assumed to be a system composed of a circular dielectric cylinder embedded into another and surrounded by a dielectric medium as shown in Figure 3-2. The system is illuminated by a cylindrical wave from a line source of infinite extent located at (ρ_0,ϕ_0) in a direction parallel to the cylinder axis. The TM_z wave traveling in a medium with permittivity ε_S and permeability μ_0 (Region 0) is incident on a layered dielectric circular cylinder of outer radius b with permittivity ε_1 (Region I), and inner radius a with permittivity ε_M (Region II) as illustrated in Figure 3-9.
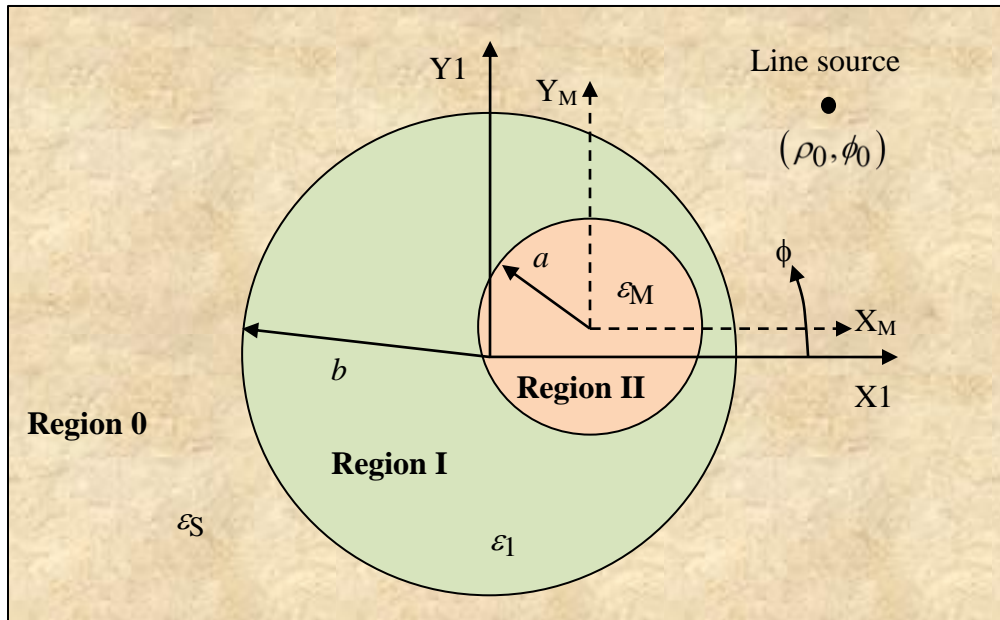
Figure 3-9. Geometry of the layered dielectric cylinders. The TM_z wave traveling in a medium with permittivity ε_S and permeability μ_0 (Region 0) is incident on a layered dielectric circular cylinder of outer radius b with permittivity ε_1 (Region I), and inner radius a with permittivity ε_M (Region II)

The fields in the dielectric regions are expressed in terms of a set of cylindrical harmonic functions with unknown coefficients. The time dependence $e^{j\omega t}$ is implied and suppressed throughout the derivation. The incident electric field E_z^i is given by [49]:

$$E_z^i(\rho,\phi) = -\frac{\eta_0 k_0 I}{4} H_0^{(2)}\left(k_0 |\vec{\rho} - \vec{\rho}_0|\right) \tag{3.41}$$

where I is the current of the line source, $k_0 = \omega\sqrt{\varepsilon_s \mu_0}$ is the wave number in the incident medium, ε_s is the permittivity of the soil, and $\eta_0 = \sqrt{\mu_0/\varepsilon_s}$ is the intrinsic impedance of the medium. E_z^i can be expressed in terms of cylindrical harmonic functions as

$$E_z^i(\rho,\phi) = \begin{cases} -\dfrac{\eta_0 k_0 I}{4} \displaystyle\sum_{n=-\infty}^{\infty} H_n^{(2)}(k_0\rho_0) J_n(k_0\rho) e^{jn(\phi-\phi_0)}, & \rho \le \rho_0 \\[4mm] -\dfrac{\eta_0 k_0 I}{4} \displaystyle\sum_{n=-\infty}^{\infty} H_n^{(2)}(k_0\rho) J_n(k_0\rho_0) e^{jn(\phi-\phi_0)}, & \rho \ge \rho_0 \end{cases} \tag{3.42}$$

where J_n and $H_n^{(2)}$ are the Bessel function of the first kind and Hankel function of the second kind, respectively. The line source excitation is given by

$$E_0 = -\frac{\eta_0 k_0 I}{4}. \tag{3.43}$$

The z-component of the total electric field in region 0 (soil) is expressed as

$$E_z^0(\rho_1,\phi_1) = E_0 \sum_{n=-\infty}^{\infty} \left[H_n^{(2)}(k_0\rho_0) J_n(k_0\rho_1) + B_n^0 H_n^{(2)}(k_0\rho_1) \right] e^{jn(\phi_1-\phi_0)} \tag{3.44}$$

54

where B_n^0 are the unknown scattering coefficients. The electric field inside each region p (p = I,

II) is expressed with respect to the (X_M, Y_M) coordinate system as

$$E_z^p\left(\rho_M,\phi_M\right)=E_0\sum_{n=-\infty}^{\infty}\left[A_n^p J_n\left(k_p\rho_M\right)+B_n^p H_n^{(2)}\left(k_p\rho_M\right)\right]e^{jn\phi_M}\quad(3.45)$$

where $k_p=\omega\sqrt{\varepsilon_p\mu_p}$ and A_n^p, B_n^p are the unknown scattering coefficients in each region. To

translate the field to the (X_1, Y_1) coordinate system, the addition theorem for cylindrical

functions was used [53]. In summary, the addition theorem establishes that

$$\begin{pmatrix}displaced\ wave\\of\ order\ \upsilon\end{pmatrix}=\sum_m J_m\left(kr_0\right)\times\begin{pmatrix}undisplaced\ wave\\of\ order\ \upsilon+m\end{pmatrix}.$$

Therefore, the translated field equation from the (X_M, Y_M) coordinate system to the (X_1, Y_1)

coordinate system is given by

$$E_z^p\left(\rho_p,\phi_p\right)=E_0\sum_{n=-\infty}^{\infty}\sum_{i=-\infty}^{\infty}J_{i-n}\left(k_p r_{pM}\right)$$

$$\cdot\left[A_n^p J_i\left(k_p\rho_p\right)+B_n^p H_i^{(2)}\left(k_p\rho_p\right)\right]e^{j\left[i\phi_p-(i-n)\phi_{pM}\right]}$$

(3.46)

where r_{pM} is the distance between the origin of the (X_1, Y_1) coordinate system and the origin of

the (X_M, Y_M) coordinate system and ϕ_{pM} is the angle between the origin of (X_1, Y_1) and the

origin of (X_M, Y_M) coordinate systems.

For the magnetic field, the z component of the total magnetic field in region 0 is given by

55

$$H_\phi^0 (\rho_1, \phi_1) = \frac{E_0}{j\eta_0} \sum_{n=-\infty}^{\infty} \left[H_n^{(2)} (k_0 \rho_0) J_n' (k_0 \rho_1) + B_n^0 H_n^{(2)'} (k_0 \rho_1) \right] e^{jn(\phi_1 - \phi_0)} \quad (3.47)$$

and inside each region p (p = I, II) is expressed with respect to the (X_M, Y_M) coordinate system

as

$$H_\phi^p (\rho_M, \phi_M) = \frac{E_0}{j\eta_p} \sum_{n=-\infty}^{\infty} \left[A_n^p J_n' (k_p \rho_M) + B_n^p H_n^{(2)'} (k_p \rho_M) \right] e^{jn\phi_M} \quad (3.48)$$

where η_0 and η_p are the intrinsic impedances of region 0 and region p, respectively. Translating

the equation to the (X_1, Y_1) coordinate system

$$H_\phi^p (\rho_p, \phi_p) = \frac{E_0}{j\eta_p} \sum_{n=-\infty}^{\infty} \sum_{i=-\infty}^{\infty} J_{i-n} (k_p r_{pM})$$

$$\cdot \left[A_n^p J_i' (k_p \rho_p) + B_n^p H_i^{(2)'} (k_p \rho_p) \right] e^{j\left[i\phi_p - (i-n)\phi_{pM} \right]} . \quad (3.49)$$

Boundary conditions

      The present case involves two embedded cylinders. There are two boundary surfaces

available on which the boundary conditions for the electric and magnetic fields are to be applied.

Boundary conditions at the external surface (p = I)

      At the outermost surface $\rho_I = r_I = b$ the boundary conditions are

$$E_z^0 (r_I, \phi_I) = E_z^I (r_I, \phi_I) \quad (3.50)$$

and

$$H_\phi^0(r_I, \phi_I) = H_\phi^I(r_I, \phi_I). \tag{3.51}$$

For the electric field,

$$E_0 \sum_{n=-\infty}^{\infty} \left[H_n^{(2)}(k_0 r_0) J_n(k_0 b) + B_n^0 H_n^{(2)}(k_0 b) \right] e^{jn(\phi_I - \phi_0)}$$

$$= E_0 \sum_{n=-\infty}^{\infty} \sum_{i=-\infty}^{\infty} J_{i-n}(k_I r_{IM}) \tag{3.52}$$

$$\cdot \left[A_n^I J_i(k_I b) + B_n^I H_i^{(2)}(k_I b) \right] e^{j\left[i\phi_I - (i-n)\phi_{IM} \right]}$$

Two complex exponential functions are said to be orthogonal over $[-\pi, \pi]$ if the inner product is

equal to zero. If $F(x) = e^{jnx}$ and $G(x) = e^{jkx}$, the inner product is

$$\langle F(x), G(x) \rangle = \int_{-\pi}^{\pi} F(x) \cdot G(x)^* dx$$

$$= \int_{-\pi}^{\pi} e^{j(n-k)x} dx \tag{3.53}$$

$$= \left[\frac{e^{j(n-k)x}}{j(n-k)} \right]_{-\pi}^{\pi} = 0$$

Using orthogonality of complex exponential functions and equating to zero yields

$$\left[H_q^{(2)}(k_0 r_0) J_q(k_0 b) + B_q^0 H_q^{(2)}(k_0 b) \right] e^{-jn\phi_0}$$

$$= \sum_{n=-\infty}^{\infty} J_{q-n}(k_I r_{IM}) \cdot \left[A_n^I J_q(k_I b) + B_n^I H_q^{(2)}(k_I b) \right] e^{-j(q-n)\phi_{IM}} . \tag{3.54}$$

Solving equation (3.53) for B_q^0 results in

$$B_q^0 = \frac{1}{H_q^{(2)}(k_0 b)} \cdot \left\{ H_q^{(2)}(k_0 r_0) J_q(k_0 b) + e^{-jq\phi_0} \sum_{n=-\infty}^{\infty} J_{q-n}(k_I r_{IM}) \right.$$

$$\left. \cdot \left[A_n^I J_q(k_I b) + B_n^I H_q^{(2)}(k_I b) \right] e^{-j(q-n)\phi_{IM}} \right\} . \tag{3.55}$$

Following the same procedure for the magnetic field and solving for B_q^0 yields

$$B_q^0 = \frac{1}{H_q^{(2)\prime}(k_0 b)} \cdot \left\{ -H_q^{(2)}(k_0 r_0) J_q'(k_0 b) + \frac{\eta_0}{\eta_I} e^{-jq\phi_0} \sum_{n=-\infty}^{\infty} J_{q-n}(k_I r_{IM}) \right.$$

$$\left. \cdot \left[A_n^I J_q'(k_I b) + B_n^I H_q^{(2)\prime}(k_I b) \right] e^{-j(q-n)\phi_{IM}} \right\} . \tag{3.56}$$

Equating (3.54) and (3.55) to eliminate B_q^0,

$$\frac{1}{H_q^{(2)}(k_0 b)} \cdot \left\{ H_q^{(2)}(k_0 r_0) J_q(k_0 b) + e^{-jq\phi_0} \sum_{n=-\infty}^{\infty} J_{q-n}(k_I r_{IM}) \right.$$

$$\left. \cdot \left[A_n^I J_q(k_I b) + B_n^I H_q^{(2)}(k_I b) \right] e^{-j(q-n)\phi_{IM}} \right\}$$

(3.57)

$$= \frac{1}{H_q^{(2)\prime}(k_0 b)} \cdot \left\{ -H_q^{(2)}(k_0 r_0) J_q'(k_0 b) + \frac{\eta_0}{\eta_I} e^{-jq\phi_0} \sum_{n=-\infty}^{\infty} J_{q-n}(k_I r_{IM}) \right.$$

$$\left. \cdot \left[A_n^I J_q'(k_I b) + B_n^I H_q^{(2)\prime}(k_I b) \right] e^{-j(q-n)\phi_{IM}} \right\}$$

or, rearranged (3.57) becomes,

$$\sum_{n=-\infty}^{\infty} \left\{ J_{q-n}(k_I r_{IM}) e^{-jq\phi_0 - j(q-n)\phi_{IM}} \right. .$$

$$\left. \cdot \left[\left(\frac{J_q(k_I b)}{H_q^{(2)}(k_0 b)} - \frac{\eta_0}{\eta_I} \frac{J_q'(k_I b)}{H_q^{(2)\prime}(k_0 b)} \right) A_n^I + \left(\frac{H_q^{(2)}(k_I b)}{H_q^{(2)}(k_0 b)} - \frac{\eta_0}{\eta_I} \frac{H_q^{(2)\prime}(k_I b)}{H_q^{(2)\prime}(k_0 b)} \right) B_n^I \right] \right\}$$

(3.58)

$$= H_q^{(2)}(k_0 r_0) \left[\frac{J_q(k_0 b)}{H_q^{(2)}(k_0 b)} - \frac{J_q'(k_0 b)}{H_q^{(2)\prime}(k_0 b)} \right] .$$

Boundary conditions at the core surface ($p = II$)

At the surface of the core (e.g. inner) cylinder, continuity of the tangential components of the electric and magnetic fields is enforced. For the electric field at $\rho_{II} = r_{II} = a$

$$E_z^{II}(r_{II}, \phi_{II}) = E_z^I(r_{II}, \phi_{II})$$

(3.59)

Therefore,

$$\sum_{n=-\infty}^{\infty} \left[A_n^{II} J_n(k_{II}a) + B_n^{II} H_n^{(2)}(k_{II}a) \right] e^{jn\phi_{II}}$$

$$\text{(3.60)}$$

$$= \sum_{n=-\infty}^{\infty} \left[A_n^I J_n(k_I a) + B_n^I H_n^{(2)}(k_I a) \right] e^{jn\phi_{II}} .$$

The fields at the core cylinder are to be finite. Therefore, the condition $B_n^{II} = 0$ is imposed.

Simplifying (3.60) yields,

$$\sum_{n=-\infty}^{\infty} \left[A_n^{II} J_n(k_{II}a) \right] e^{jn\phi_{II}} = \sum_{n=-\infty}^{\infty} \left[A_n^I J_n(k_I a) + B_n^I H_n^{(2)}(k_I a) \right] e^{jn\phi_{II}} \qquad \text{(3.61)}$$

Applying orthogonality of exponential functions (3.53) and equating to zero,

$$J_q(k_{II}a) A_q^{II} - J_q(k_I a) A_q^I - H_q^{(2)}(k_I a) B_q^I = 0 . \qquad \text{(3.62)}$$

Following the same procedure for the magnetic field,

$$H_\phi^{II}(r_{II}, \phi_{II}) = H_\phi^I(r_{II}, \phi_{II}) \qquad \text{(3.63)}$$

and

$$\frac{1}{\eta_{II}} J_q'(k_{II}a) A_q^{II} - \frac{1}{\eta_I} J_q'(k_I a) A_q^I - \frac{1}{\eta_I} H_q^{(2)\prime}(k_I a) B_q^I = 0 . \qquad \text{(3.64)}$$

Using equations (3.62) and (3.64) to eliminate A_q^{II} yields

$$A_n^{II} = \frac{J_n(k_I a)}{J_n(k_{II}a)} A_n^I + \frac{H_n^{(2)}(k_I a)}{J_n(k_{II}a)} B_n^I \qquad \text{(3.65)}$$

and

$$A_n^{II} = \frac{\eta_{II}}{\eta_I} \frac{J_n'(k_I a)}{J_n'(k_{II} a)} A_n^I + \frac{\eta_{II}}{\eta_I} \frac{H_n^{(2)'}(k_I a)}{J_n'(k_{II} a)} B_n^I. \tag{3.66}$$

Equating (3.65) and (3.66),

$$\left[\frac{J_n(k_I a)}{J_n(k_{II} a)} - \frac{\eta_{II}}{\eta_I} \frac{J_n'(k_I a)}{J_n'(k_{II} a)} \right] A_n^I + \left[\frac{H_n^{(2)}(k_I a)}{J_n(k_{II} a)} - \frac{\eta_{II}}{\eta_I} \frac{H_n^{(2)'}(k_I a)}{J_n'(k_{II} a)} \right] B_n^I = 0. \tag{3.67}$$

Equations (3.58) and (3.67) constitute a system of linear equations of the unknown coefficients A_n^I and B_n^I. Once these equations are solved, values for A_n^I and B_n^I are used in equation (3.55) or (3.56) to compute the scattering coefficients B_n^0. The values of the scattering coefficients are then used to compute the fields in each region due to a line source excitation.

As established in section 3.2.1, an important parameter in scattering is the scattering width. The scattering width is obtained by calculating the ratio of the scattered field in the far zone to the incident field.

$$\sigma(\phi) = \lim_{\rho \to \infty} 2\pi\rho \left| \frac{E_z^s(\rho,\phi,\phi_0)}{E_z^i(\rho,\phi,\phi_0)} \right|^2 \tag{3.68}$$

From equation (3-44), the scattered field is

$$E_z^s(\rho_1,\phi_1) = E_0 \sum_{n=-\infty}^{\infty} B_n^0 H_n^{(2)}(k_0 \rho_1) e^{jn(\phi_1-\phi_0)} \tag{3.69}$$

61

where the value of E_0 depends on the excitation (line source or plane wave). Using the large argument of the Hankel function and normalizing the resulting expression by a factor of $E_0\left(\sqrt{2j/\pi k\rho}\right)e^{-jk\rho}$, yields

$$E_z^s(\phi, \phi_o) = \sum_{n=-\infty}^{\infty} B_n^0 j^n e^{jn(\phi-\phi_0)}. \qquad (3.70)$$

For the composite cylinder, the scattering cross-section is given by

$$\sigma(\phi) = \frac{2}{\pi}\left|\sum_{n=-\infty}^{\infty} B_n^0 j^n e^{jn(\phi-\phi_0)}\right|^2. \qquad (3.71)$$

Near-field distribution and scattering width for the composite cylinder are computed in the next section for both concentric and eccentric configurations.

3.3   Simulation of electromagnetic scattering from an underground hydrocarbon spill

The expressions presented in section 3.2 were used to simulate the electromagnetic scattering from an underground hydrocarbon spill. The spill is assumed to be a system composed of a circular dielectric cylinder embedded into another and surrounded by a dielectric medium as shown in Figure 3-2. The center frequency used is 500 MHz. This frequency is low enough for good penetration into the soil, and high enough for good resolution of small objects. An object is considered small if its radius is less or equal to the wavelength of the incident wave. Even though a center frequency of 500 MHz is used, the system is assumed to radiate substantial energy from 100 MHz to 1 GHz. Different sizes and configurations of contaminated spills were simulated.

Results for concentric and eccentric configurations illuminated by a plane and a line source are presented.

3.3.1 Homogeneous spills illuminated by a plane wave

The expressions for the electric fields in each region were verified using known configurations. First, the case of two concentric cylinders made of the same material in free space was considered. This was achieved by letting $\varepsilon_2 = \varepsilon_1$ and $\mu_2 = \mu_1$. The incident field is a plane wave with a frequency of 500 MHz. The incident wave has amplitude of one and is traveling along the +y direction. As the wave propagates along +y direction, it is disturbed by a dielectric circular cylinder with $\varepsilon_r = 2.2 - j0$ at 500 MHz and radius equal to 1 wavelength of the incident wave. A target with permittivity of $2.2\varepsilon_0$ represents oil contamination. The scattering width for TM excitation is presented in Figure 3-10(a). These results are as expected for a dielectric cylinder in free space. The electric field magnitude scattered by the homogeneous dielectric cylinder in air is presented in Figure 3-10(b). The incident plane wave is diffracted by the dielectric cylinder, creating a maximum peak in the forward direction and standing waves appear in the backward direction. The peak observed at the back side of the cylinder decreases rapidly, leaving a shadow area in the forward direction.

Now, soil dielectric characteristics are considered to analyze the GPR response from the dielectric target. Figures 3-11 and 3-12 show the modeled scattered field from the same dielectric target in two different backgrounds: dry and wet soil. The scattering width for the system of homogeneous wet soil and a spill with a radius equal to the incident wavelength in wet soil at 500 MHz is shown in Figure 3-13.
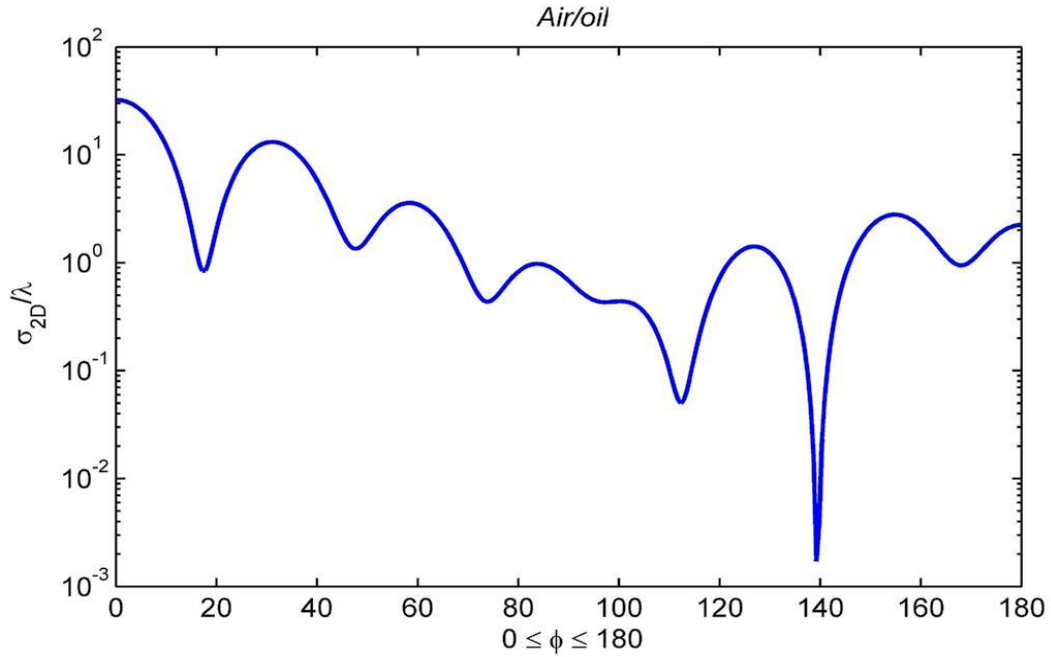
(a)
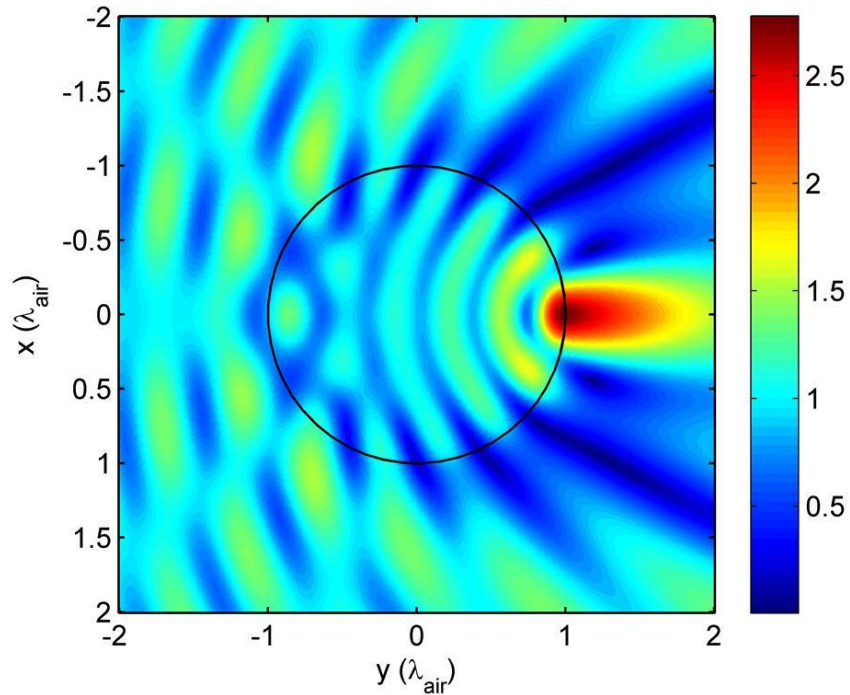
(b)

Figure 3-10. Scattering by a homogeneous cylinder in air. (a) Scattering width σ_{2D} / λ as a function of scattering angle ϕ. $\phi_0 = 180^\circ$, $\varepsilon_r = 2.2 - j0$, and $r = \lambda$. (b) The simulated electric field magnitude. The black line denotes the cylinder location.
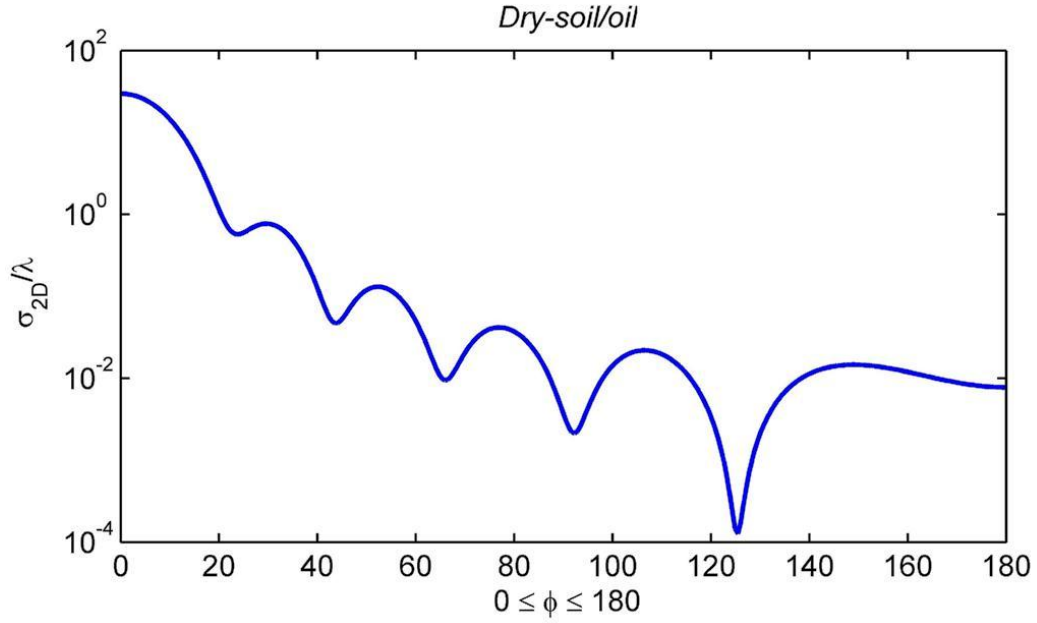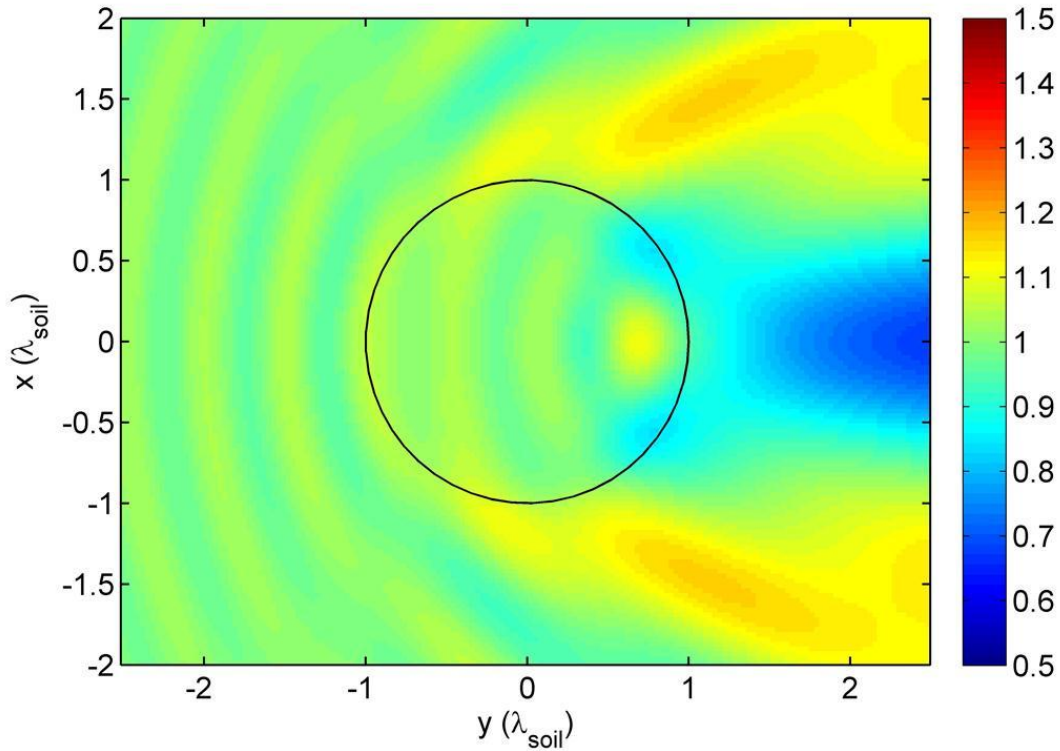
Figure 3-11. Scattering by a homogeneous oil spill in dry soil. (a) Scattering width σ_{2D} / λ as a function of scattering angle ϕ. $\phi_0 = 180°$, $\varepsilon_r = 2.2 - j0$, and $r = \lambda$. (b) The simulated electric field magnitude. The black line denotes the cylinder location.
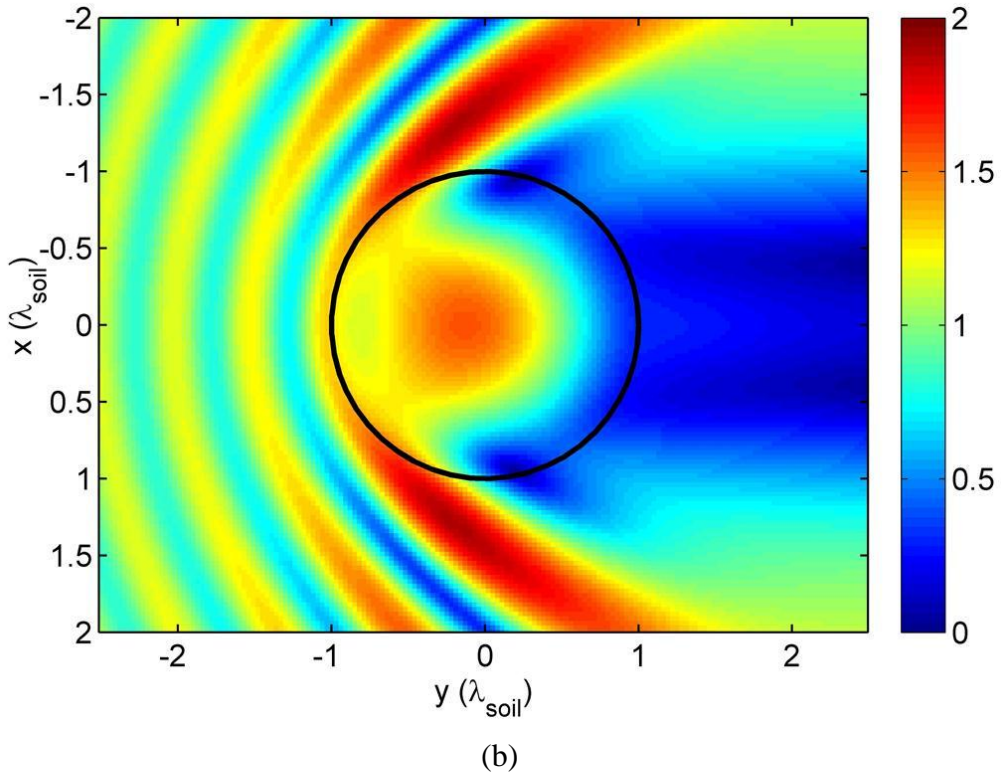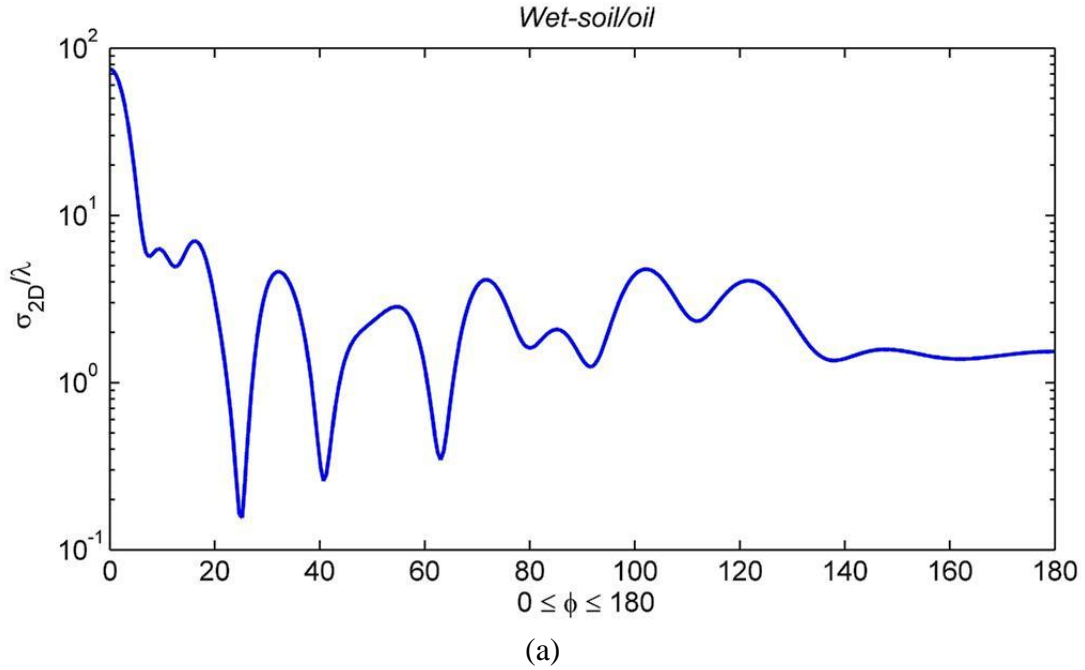
Figure 3-12. Scattering by a homogeneous oil spill in wet soil. (a) Scattering width σ_{2D} / λ as a function of scattering angle ϕ. $\phi_0 = 180°$, $\varepsilon_r = 2.2 - j0$, and $r = \lambda$. (b) The simulated electric field magnitude. The black line denotes the cylinder location.
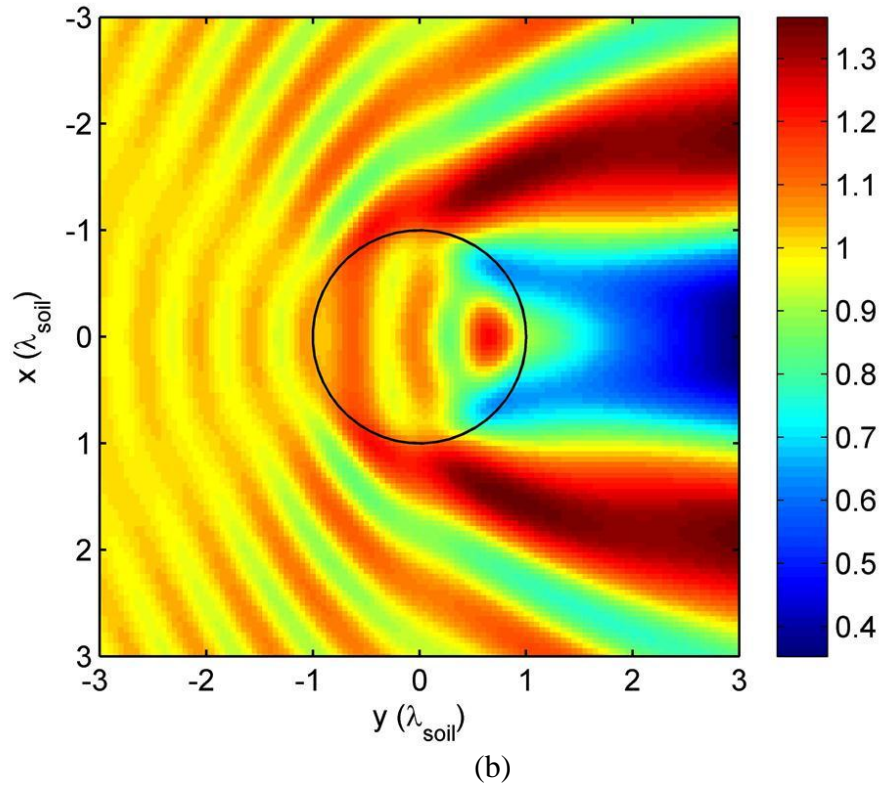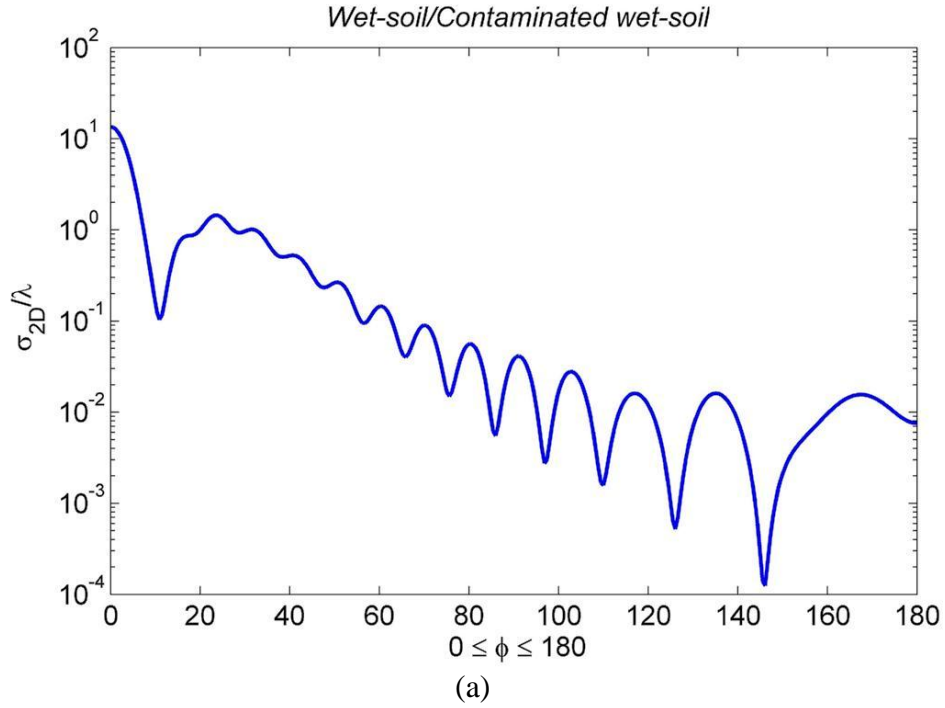
Figure 3-13. Scattering by a homogeneous wet-contaminated spill in wet soil. (a) Scattering width σ_{2D} / λ as a function of scattering angle ϕ. $\phi_0 = 180^\circ$, $\varepsilon_r = 12 - j0$, and $r = \lambda$. (b) The simulated electric field magnitude. The black line denotes the cylinder location.

Note that the field distribution in Figures 3-11(b) and 3-12(b) from the dry and wet soil

background cases, both viewed in cross section, are completely different. The dielectric constant

differences between dry and wet soil generate remarkable differences in these two cases. When

the soil is wet, the permittivity increases and more contrast between the soil and the spill is

obtained. In the vadose region, the soil and contaminated soil is mostly uniformly wet. Assuming

that the soil has 25% water content, the measured value of relative permittivity is approximately

17. The same amount of water content in the contaminated soil has a relative permittivity value

of 12. The scattering width for the system of homogeneous wet soil and a spill with a radius

equal to the incident wavelength in wet soil at 500 MHz is shown in Figure 3-13. Notice that the

magnitude of the signal is attenuated at this incident frequency. Soil moisture increases the radar

attenuation rates, limiting radar performance.

3.3.2 Inhomogeneous spill illuminated by a plane wave

A more realistic approach to the problem is to assume that the spill is not homogeneous,

but composed of separated layers with different permittivity. To simulate this, the spill is

assumed to be a layered dielectric circular cylinder of outer radius b with permittivity ε_1, and

inner radius a with permittivity ε_2 as illustrated in Figure 3-9.

The first configuration analyzed is a concentric cylinder with small radius relative to the

wavelength in wet soil of the incident wave. The spill has a relative permittivity of $\varepsilon_1 = 12$ in the

outer layer, corresponding to contaminated soil with 25% water content and 25% oil content, and

$\varepsilon_2 = 2.2$ in the core region. The permittivity of 2.2 corresponds to fully contaminated soil or soil

with more than 50% oil. The pores of the soil in the core region are assumed to be saturated with

oil and the water had been displaced to the outer region. The total radius of the spill is 2λ and the

core region radius is equal to λ of the field wave in wet soil. The simulated electric field

magnitude for an incident plane wave with a frequency of 500 MHz is shown in Figures 3-14.

The scattering pattern in the wet soil region is similar to the scattering pattern for a homogeneous

cylinder, but a reduction in the scattered field magnitude is observed in the direction of

propagation at x = 0. There is a significant contrast between the outer cylinder and the core

cylinder. The change in wavelength is observed. This difference in permittivity produces a well-

defined shadow area in the forward direction that starts in the outer cylinder. The wave fronts do

not reform after passing through the contaminated region, making this a useful characteristic for

determining the concentration of contaminant in the soil.
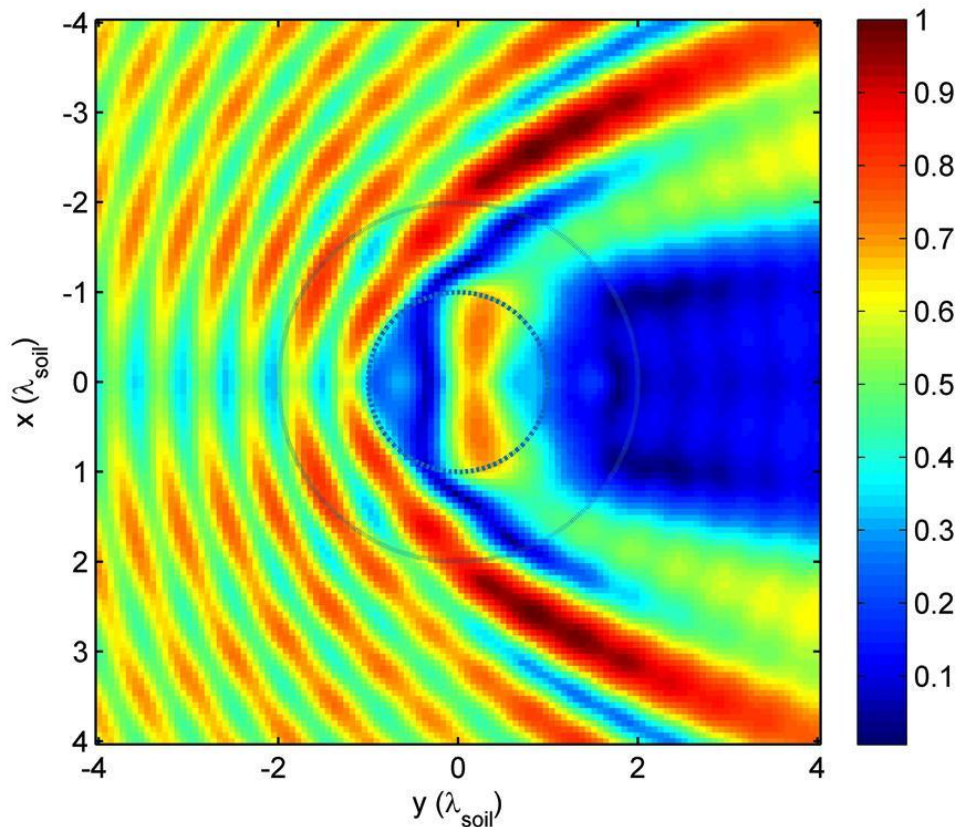
Figure 3-14. Simulated electric field magnitude for a layered small spill in wet soil at 500 MHz.
The inner circle represents pure contamination of oil ($\varepsilon_r = 2.2$) and the outer
cylinder represents wet-contaminated soil ($\varepsilon_r = 12$). The cylinders are surrounded
by wet soil.

Not all oil spills spread radially from the source. Depending on the soil and other parameters, contamination could spread at different rate in different directions. A spill with a shifted core region is illustrated in Figure 3-15. As before, the core is assumed to be fully contaminated soil and the water particles are pushed to the surroundings. The size of the core is 1/3 the size of the total contaminated area. There is a shadow area behind the core cylinder. When the wave transition into the wet soil area, the wave fronts start to regenerate. The direction of propagation of these wave fronts is deflected by the position of the core.
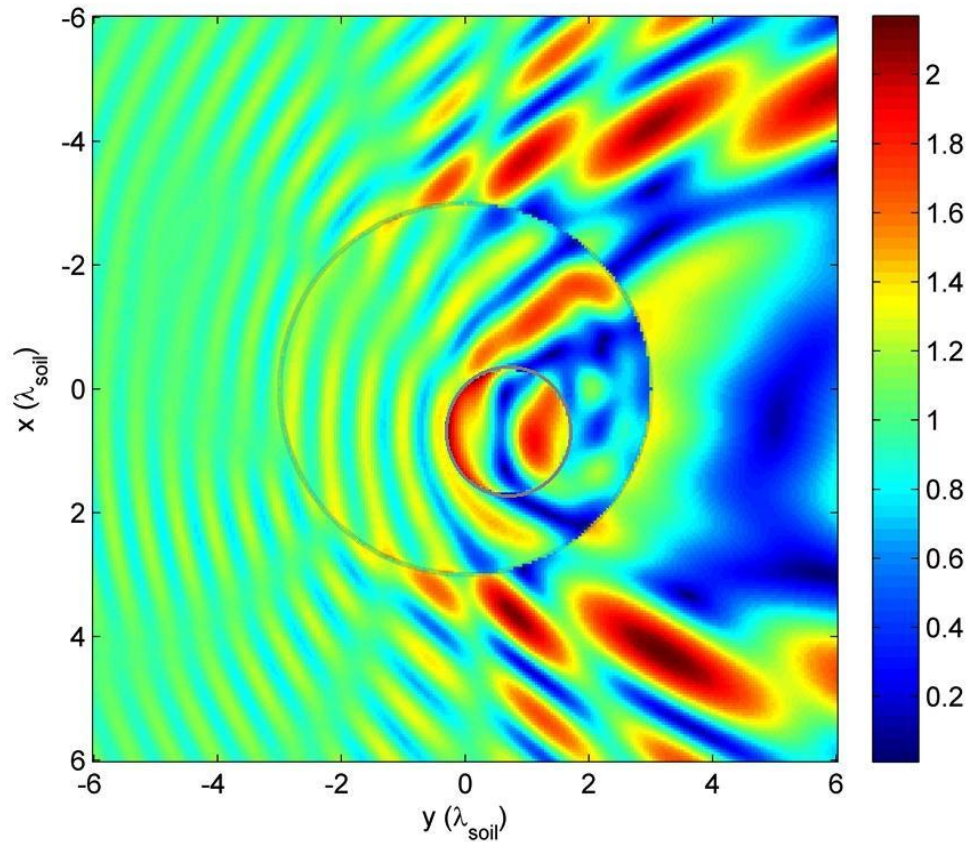
Figure 3-15. Simulated electric field magnitude for an eccentric spill in wet soil at 500 MHz. The inner circle represents pure contamination of oil ($\varepsilon_r = 2.2$) and the outer cylinder represents wet-contaminated soil ($\varepsilon_r = 12$). The cylinders are surrounded by wet soil.

3.3.3 Line source illumination

The electric field magnitude for a small spill in the vadose region illuminated by a line source with a frequency of 500 MHz is shown in Figure 3-16 for the homogeneous case. The wet-contaminated soil has $\varepsilon_r = 12$ and radius equal to one wavelength of the incident wave is assumed. The wet soil has a relative permittivity of 17. The wave travels from a high permittivity medium to a lower permittivity target.
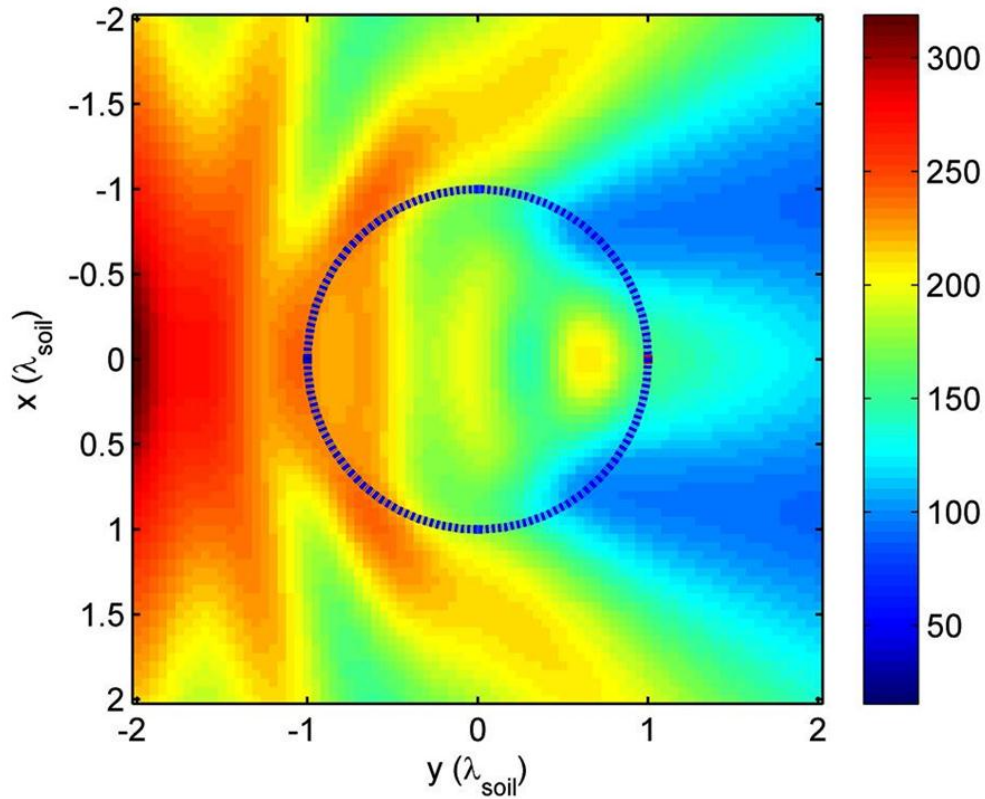
Figure 3-16. Electric field magnitude for a spill in a vadose region. The blue dashed line represents the position of the spill. The line source is located at $3\lambda_{soil}$ from the spill.

A concentric spill with a relative permittivity of $\varepsilon_1 = 12$ in the outer layer, and $\varepsilon_2 = 2.2$ in the core region is now presented. As before, the pores of the soil in the core region are

assumed to be saturated with oil and the water had been displaced to the outer region. The total

radius of the spill is 2λ and the core region radius is λ of the field wave in wet soil. The electric

field magnitude for an incident plane wave with a frequency of 500 MHz is shown in Figure 3-

17. Standing waves appear in the wet-contaminated region of the spill due to backward scattering

from the core region. At the core, a single period of the wave can be seen, with minima and

maxima amplitude.
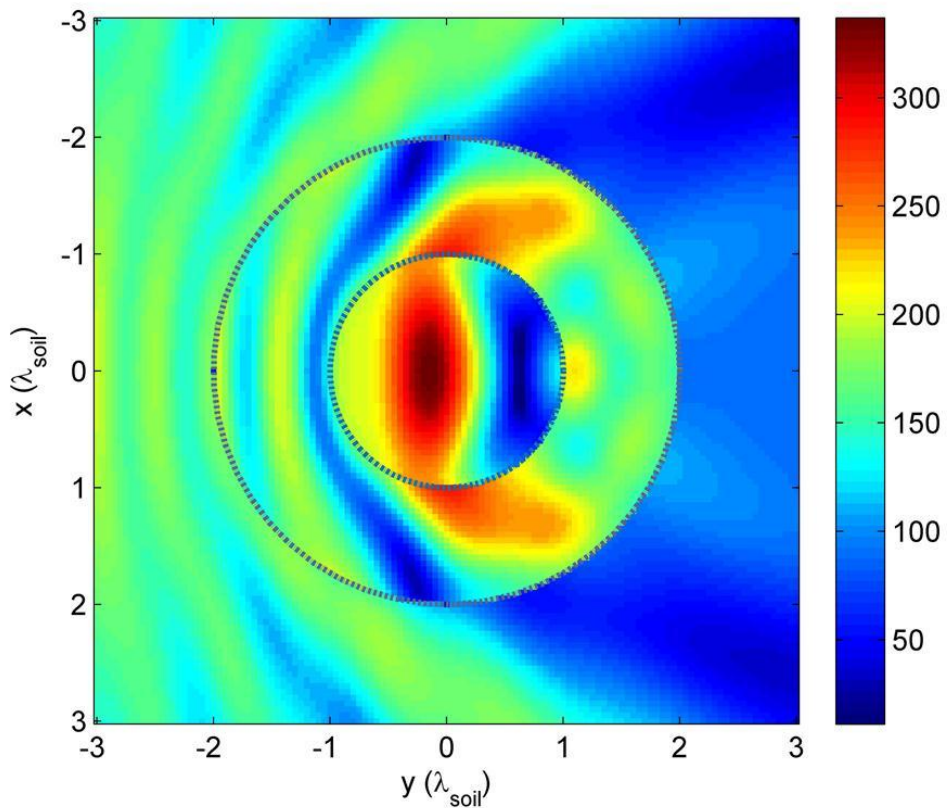
Figure 3-17. Simulated electric field magnitude for a concentric spill in wet soil illuminated by a
line source with frequency of 500 MHz. The inner circle represents pure
contamination of oil ($\varepsilon_r = 2.2$) and the outer cylinder represents wet-contaminated
soil ($\varepsilon_r = 12$).

An eccentric spill with its core region located at the bottom-right side of the contaminated

area was simulated to inspect its scattering characteristics. The size of the core is 1/3 the size of

the total spill. The shadow area behind the spill is disturbed by the scattering from the core that is

closer to the spill's boundary. The waves are deflected in the direction of the shifted core. This is

shown in Figure 3-18.
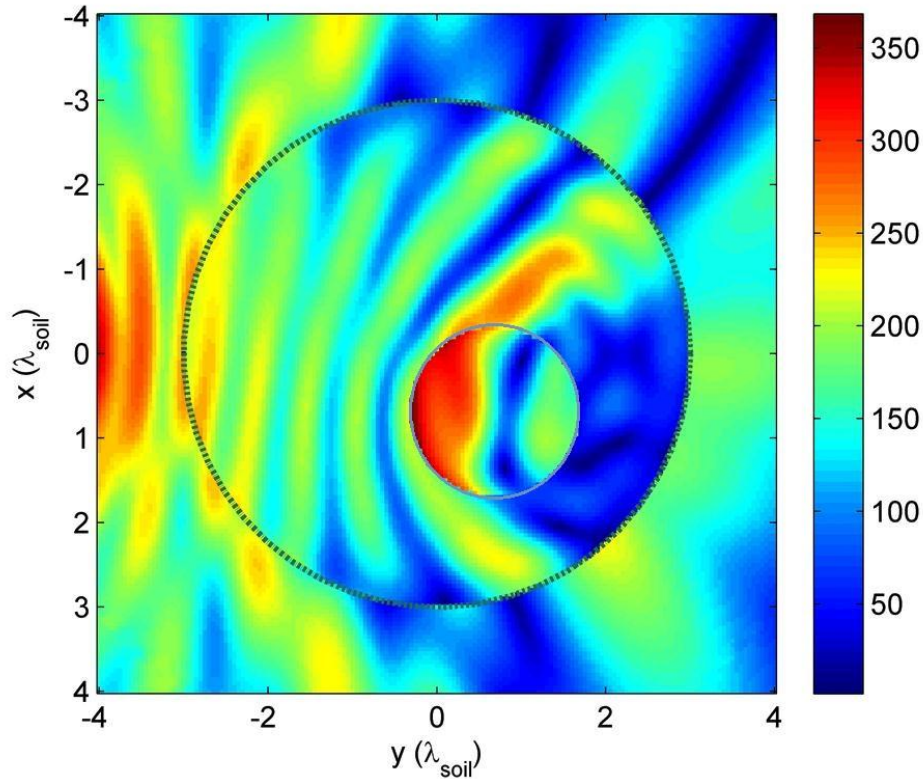
Figure 3-18. Simulated electric field magnitude for an eccentric spill in wet soil at 500 MHz. The
inner circle represents pure contamination of oil ($\varepsilon_r = 2.2$) and the outer cylinder
represents wet-contaminated soil ($\varepsilon_r = 12$).

In this chapter, solutions for scattering from a dielectric cylinder of infinite length were

reviewed. Values of permittivity obtained using the coaxial waveguide presented in Chapter 2

were used for a computer simulation of the electric field magnitude in a contaminated

underground system. Scattered field matrices obtained will be used as input parameter in the

inversion algorithm presented in Chapter 4.

CHAPTER 4

INVERSION ALGORITHM

4.1   Introduction

In this chapter, an inversion algorithm for underground spill localization is presented. Inversion techniques in the frequency domain are more common for microwave medical and ultrasound imaging modalities, but have also been applied to stepped frequency GPR [54],[55]. The most common form of single frequency inversion is tomographic [56]. Tomography generates an image of the entire illuminated region, making it useful for characterizing variations of material type. Cross-well radar (CWR) tomography, otherwise known as cross-borehole ground-penetrating radar (cross-borehole GPR) is a minimally invasive method that uses high frequency electromagnetic waves transmitted and received by antennas in the subsurface to image objects of contrasting dielectric properties [57]. Cross-borehole GPR measures transmission as well as reflection signals, making it better suited for frequency domain inversion [58],[59]. A 2D diffraction tomography inversion algorithm and results calculated using synthetic data are presented in this chapter.

4.2   Diffraction Tomography

Diffraction tomography (DT) is based on the determination of the dielectric properties of an object. The response of the object from both the electric and the magnetic field must be evaluated, as well as the interaction between the sample and the probe. DT was first proposed by Wolf in [60] and is now widely used in various forms for such applications as medical imaging, optical imaging, geophysical tomography and radar imaging [60]-[66]. The principle of DT is

based on the derivation of a linear relation between the spatial Fourier transform of the contrast function and the scattered field for weak scatterers [61]-[63],[67],[68]. A generalized DT algorithm for multi-frequency multi-monostatic Ground Penetrating Radar (GPR) measurement configuration was first proposed by Deming and Devaney in [67]. Most of the related works on DT were originally focused on freespace synthetic aperture radar (SAR) imaging [65],[66] and later on subsurface imaging [67]-[69].

The information bearing signals associated with tomographic imaging are scattering, diffraction and significant attenuation, making many conventional imaging techniques not applicable [69]. The success of diffraction tomography techniques relies on three assumptions: linearity, number of transmitters and receivers, and frequencies used [70]. Linearized diffraction tomography is based on linear approximation of the scattered field such as Born- or Rytov-type approximations [71]. Both approximations can produce excellent reconstructions for small objects with small refractive index changes. In many cases, the linearity assumption fails; however, for geophysical applications and other cases, the target can be considered a weak scatterer and therefore the linear assumption holds [72], [73]. From a resolution point of view, the best way to implement diffraction tomography is by using the highest possible number of receiver/transmitter units, together with the highest number of frequencies available. Different constraints, like economic, safety, operating, geometric or physical, limit the number of receiving and/or transmitting units, leading to insufficient or incomplete data sampling which reduces the resolution or fidelity of the reconstructed image. Although frequency is not an intrinsic problem of diffraction tomography, it drastically limits the resolution attainable in the reconstruction process. As presented in [71], Born and Rytov approximations are valid only if the inhomogeneities in the medium are relatively small compared with the wavelength of the

incident field. On the other hand, attenuation in a lossy medium is heavily dependent on frequency: higher frequencies yield higher losses. In some applications, such as geophysical and biomedical imaging, the choice of the frequency is essentially based on the highest possible value such that scattered fields can still be detected above a certain signal-to-noise ratio (SNR) [74].

The solution is to make some necessary approximations, and usually, a Born-type approximation is used, which gives an approximate measurement of the scattering [71]. With this approximation, and the use of scattered waves collected by an array of receivers, the Fourier diffraction slice theorem can be used [75]. In this method, a plane wave propagates through the object, and scattering occurs along with diffraction either from edges, corners, creeping waves, etc. The field is measured along a parallel line and the Fourier Transform is applied to the measured data. The Fourier transformed data forms an arc through the origin in the frequency domain. The theory of this method is explained in the next section.

4.3   Fourier Diffraction Theorem

The Fourier Diffraction theorem is a fundamental theorem for the comprehension of the object reconstruction [71]. This theorem is based on the principle that objects with large inhomogeneities when compared to a wavelength of the incident field, cannot be analyzed using ray theory. Instead, one must resort directly to wave propagation and diffraction phenomena [76]. The Fourier Diffraction theorem relates the Fourier transform of the measured forward scattered field with the Fourier transform of the contrast profile of the object under test, which is the magnitude to be imaged. The Fourier Diffraction Theorem can be stated as:

When a 2D object is illuminated by a plane wave as shown in Figure 4.1, the 2D Fourier transform of the forward scattered field measured along a line perpendicular to the

76

direction of propagation of the wave (line TT' in Figure 4-1) gives the values of the 2D

Fourier transform of the contrast evaluated along a circular arc centered in $-k_0$ and radius

k_0 in the frequency domain [76].
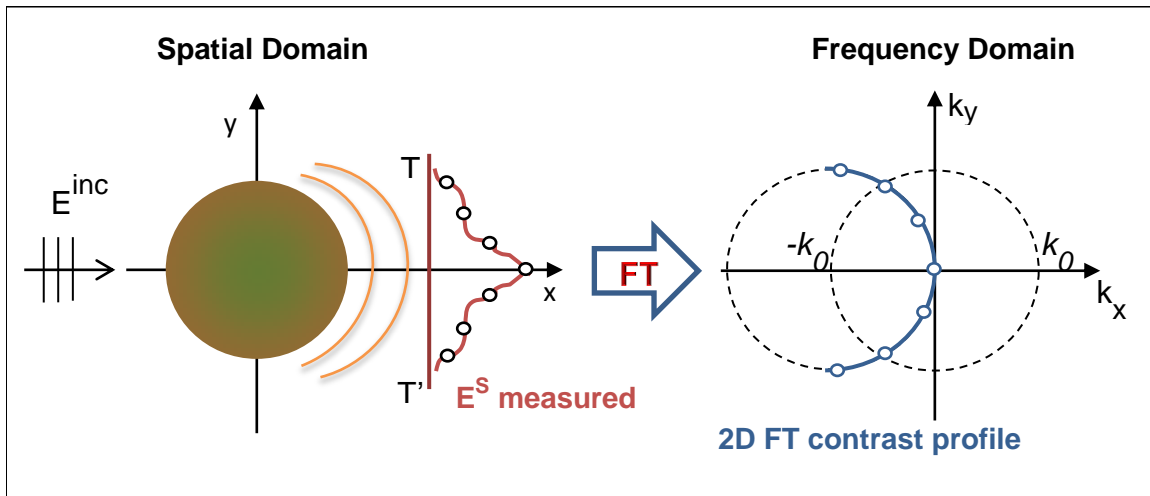
Figure 4-1. Illustration of the Fourier Diffraction Theorem. When 2D object is illuminated by a plane wave, the 2D Fourier transform (FT) of the scattered field measured along the line TT' gives the values of the 2D Fourier transform of the contrast evaluated along a circular arc centered in $-k_0$ and radius k_0 in the frequency domain.

Some important remarks of this theorem can be summarized as follows [69]:

- **Transmission and reflection measurement geometries**. When measuring scattered fields with a planar system in transmission, only the components of the angular spectrum propagating according to the direction of incidence can be measured, whereas the backscattering is lost. These forward components are associated with the right half of the circle in the spectral domain. In contrast, if another measurement line is placed in the opposite side of the object under test, or in reflection configuration, both forward and backscattered fields can be acquired and points over the entire circle in the spectral domain will be recovered. Accordingly, for a circular geometry, both

the forward and backward scattered fields can be measured and the Fourier transform of the contrast profile will be obtained over the entire shifted circle in the spectral domain. However, in practice, backscattered fields are difficult to measure near the transmitting element, and the resolution is not as good as theoretically expected.

- **Low pass filtering**. The Fourier transform of the contrast profile will be zero for the angular spatial frequencies greater than $2k_0$. For angular spatial frequencies smaller than $2k_0$ this magnitude will be placed along a circle in the transformed domain.

- **Multiview**. By changing the incidence angle, the reconstruction of the contrast profile will be obtained in shifted circles of the same radius, all with its center placed along a circle of radius k_0 centered in the origin of coordinates.

- **Multifrequency**. By changing the illuminating frequency, circles of different radius centered along the same direction are obtained.

- **Limit**. Given that the radius of the circle in spectral domain is $k_0 = \dfrac{2\pi f}{c}$ (in air), when $f \to \infty$ the circle degenerates into a line. In practice, this approximation is valid in X-rays, which simplifies greatly the reconstruction procedure in X-ray imaging systems.

The importance of the theorem is that if an object is illuminated by plane waves from many directions over 360°, the resulting circular arcs in the transformed-plane will fill up the frequency domain. The image function may be recovered by Fourier inversion [69].

In this work, a 2D geometry is assumed and hence objects under investigation and electromagnetic fields are invariant with respect to the z-axis. If vertically polarized antennas

relative to the z-axis direction are used, all electric field and current vectors are z-directed, and accordingly we can use the scalar field equations [77], [78].

Let $E_T(\vec{r})$ represent the total electric field measured at one receiving antenna in presence of the object under test, and $E_i(\vec{r})$ the incident field. The scattered field can be defined as:

$$E_S(\vec{r}) = E_T(\vec{r}) - E_i(\vec{r}) \tag{4.1}$$

In terms of the equivalent electric current radiating in the external medium, the scattering field can be expressed as:

$$E_S(\vec{r}) = -\iint_S j\omega\mu_0 J(\vec{r}) G(\vec{r} - \vec{r}') d\vec{r}' \tag{4.2}$$

where $G(\vec{r} - \vec{r}')$ is the Green's function and

$$J(\vec{r}) = -j\omega\big(\varepsilon(\vec{r}) - \varepsilon_0\big) E_T(\vec{r}) \tag{4.3}$$

is the equivalent induced electric current. The 2D Fourier transform of the induced electric current can be defined as:

$$\tilde{J}(\vec{K}) = \mathsf{F}\{J(\vec{r})\} = \iint_S J(\vec{r}) e^{j\vec{k}\vec{r}} d\vec{r} \tag{4.4}$$

For weakly scattering objects, Born-type approximations can be used [79], [80]. The simplest approximation is the first-order Born approximation, which assumes that the scattered electric field can be written only in terms of the incident field, which is known. Assume that the cylinder is illuminated by a plane wave incident at an angle θ_0, the incident electric field is

$$E_i(\vec{r}) = e^{-jk_0\hat{\theta}_0\vec{r}} \tag{4.5}$$

where $k_0 = \omega\sqrt{\mu_0\varepsilon_0}$ is the wavenumber in the surrounding medium. Note that for this work, the surrounding medium is not assumed to be free-space and hence the wavenumber and permittivity is not that of free-space; however, the surrounding medium is assumed to be non-magnetic. The quantity to be imaged is the contrast profile, defined as

$$C(\vec{r}) = 1 - \frac{\varepsilon(\vec{r})}{\varepsilon_0} = -\frac{\varepsilon(\vec{r}) - \varepsilon_0}{\varepsilon_0} \tag{4.6}$$

Inserting (4.5) into (4.4), we obtain

$$J(\vec{r}) = -j\omega\left(\varepsilon(\vec{r}) - \varepsilon_0\right)E_T(\vec{r}) = j\omega\varepsilon_0 C(\vec{r})e^{-jk_0\hat{\theta}_0\vec{r}} \tag{4.7}$$

Applying the 2D transform to (4.7),

$$\tilde{J}(\vec{K}) = \mathsf{F}\{J(\vec{r})\} = j\omega\varepsilon_0\iint_S C(\vec{r})e^{-jK_0\hat{\theta}_0\vec{r}}e^{j\vec{k}\vec{r}}\,d\vec{r}$$

$$= j\omega\varepsilon_0\iint_S C(\vec{r})e^{j\left(\vec{k}-k_0\hat{\theta}_0\right)}d\vec{r} = j\omega\varepsilon_0\tilde{C}\left(\vec{k}-k_0\hat{\theta}_0\right) \tag{4.8}$$

where $\tilde{C}\left(\vec{k}-k_0\hat{\theta}_0\right) = \iint_S C(\vec{r})e^{j\left(\vec{k}-k_0\hat{\theta}_0\right)}d\vec{r}$ is the 2D Fourier transform of the contrast profile evaluated over a circle of radius k_0 and center $-k_0\hat{\theta}_0$ in the Fourier space, as illustrated in Figure 4-2.
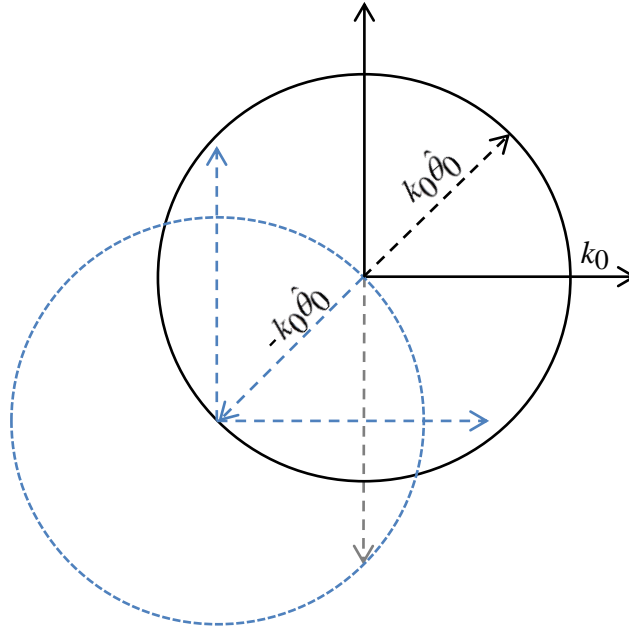
Figure 4-2. Fourier domain for an incident plane wave. Under Born approximation, the 2D Fourier transform of the contrast profile is obtained in the transformed domain over a circumference shifted on the direction opposite to the incident plane wave.

The reconstruction of (4.8) gives information of the 2D Fourier transform of the contrast profile only over a circumference of radius k_0 shifted a distance of k_0 in the direction opposite to the propagation of the incident field. In order to obtain the whole reconstruction of the object, different directions of incidence must be considered, as illustrated in Figure 4-3. In other words, by transmitting from one of the antennas and receiving from the rest and repeating this procedure for all transmitters, a two-dimensional sampling inside a circle of radius $2k_0$ in the spectral domain will be obtained. Accordingly, the reconstructed contrast profile calculated through the inversion of $\tilde{C}(\vec{k})$ will be a low-pass filtered version of the original one.
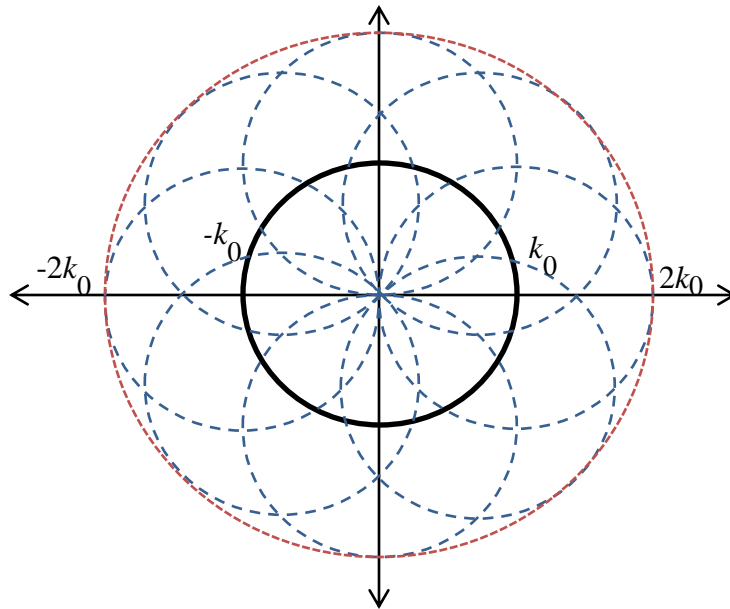
Figure 4-3. Multiview Fourier domain. Different directions of illumination are necessary to obtain the reconstruction of the object. The 2D Fourier transform of the contrast profile is obtained inside a circle of radius $2k_0$ centered at the origin.

Two configurations are commonly used for obtaining different directions of illumination: planar and circular arrays. In this work, a circular array, like the one shown in Figure 4-4, is used. For two-dimensional fields, the incident field is a cylindrical wave. The spectral formulation for planar systems can be applied in circular geometries, if a synthetic aperture approach is made. Specifically, to create a plane wave by superposing the existing cylindrical waves created by each source located along the circular antenna array.

Let's assume that the incident field in Figure 4-4 is a plane wave defined as $\vec{E}_i\left(\vec{r}, \hat{\theta}_0\right) = e^{-jk_0\hat{\theta}_0\vec{r}}$. The electric equivalent current induced in the cylinder by the incident field is $\vec{J}_b$. The current $\vec{J}_b$ radiates the scattered field $\vec{E}_s$ that is measured at the receivers.
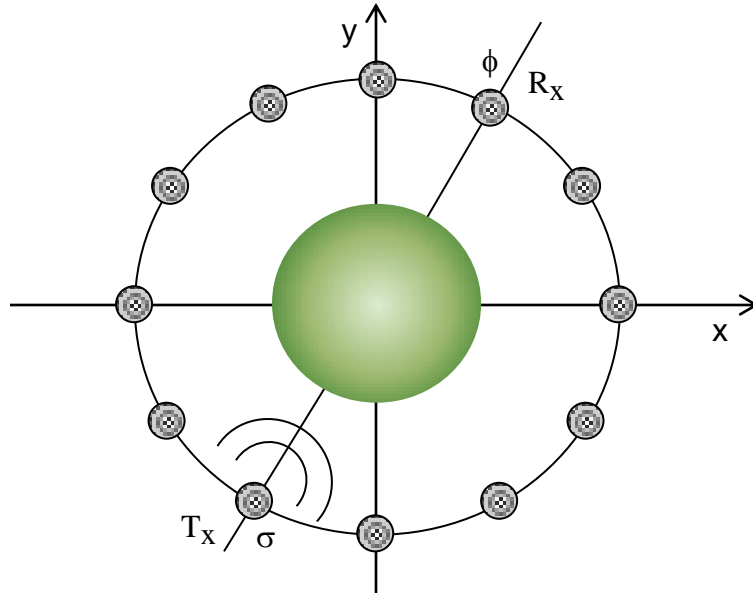
Figure 4-4. Circular array of antennas. Different directions of illumination can be obtained by transmitting with each one of the elements. The transmitter is T_X and all others are the receivers R_X.

The 2D Fourier transform of the induced current is

$$\tilde{J}_b\left(k_0\hat{\theta}\right) = \int_{v_a} \vec{J}_a \cdot \vec{E}_s dv_a \tag{4.9}$$

where $\vec{J}_a$ is the current in the transmitter, v_a is the circular path defined by the array, and

$$\tilde{J}_b\left(k_0\hat{\theta}\right) = \int \vec{J}_b e^{jk_0\hat{\theta}\vec{r}} d\vec{r} \tag{4.10}$$

Using (4.7), we obtain

$$\vec{J}_b\left(\vec{r}\right) = j\omega\varepsilon_0 C\left(\vec{r}\right) e^{-jk_0\hat{\theta}_0\vec{r}} \tag{4.11}$$

Then, $\tilde{J}_b\left(k_0\hat{\theta}\right)$ can be expressed in terms of the contrast profile

$$\tilde{J}_b\left(k_0\hat{\theta}\right) = j\omega\varepsilon_0\int C(\vec{r})e^{-jk_0\hat{\theta}_0\vec{r}} \cdot e^{jk_0\hat{\theta}_0\vec{r}}\,d\vec{r} = j\omega\varepsilon_0\tilde{C}\left(k_0\left(\hat{\theta}-\hat{\theta}_0\right)\right) \qquad (4.12)$$

For a circular antenna array of radius R centered in the xy-plane

$$j\omega\varepsilon_0\tilde{C}\left(k_0\left(\hat{\theta}-\hat{\theta}_0\right)\right) = \int_0^{2\pi} J_a\left(\phi,\theta\right)\vec{E}_s\left(\phi,\hat{\theta}_0\right)R\,d\phi \qquad (4.13)$$

It can be demonstrated that the current producing a plane wave propagating in the $\hat{\theta}$ direction can be expressed as the summation of cylindrical modes [81]:

$$I\left(\phi-\hat{\theta}\right) = \frac{-2}{\omega\mu_0R\pi}\sum_{n=-\infty}^{\infty}\frac{j^n}{H_n^{(2)}\left(k_0R\right)}e^{jn\left(\phi-\hat{\theta}\right)} \qquad (4.14)$$

where $I\left(\phi-\hat{\theta}\right)$ is the amplitude of the current distribution of the transmitter at an angular position ϕ along the antenna. Equation (4.13) can be written as,

$$j\omega\varepsilon_0\tilde{C}\left(k_0\left(\hat{\theta}-\hat{\theta}_0\right)\right) = \int_0^{2\pi} I\left(\phi-\hat{\theta}\right)\vec{E}_s\left(\phi,\hat{\theta}_0\right)R\,d\phi \qquad (4.15)$$

When the incident field is a cylindrical wave, the plane wave $\vec{E}_i\left(\vec{r},\hat{\theta}_0\right) = e^{-jk_0\hat{\theta}_0\vec{r}}$ can be expanded as the superposition of cylindrical waves $\vec{E}_i\left(\vec{r},\sigma\right)$ generated by line sources $I\left(\sigma+\hat{\theta}_0\right)$ located at an angular position σ in the array.

$$\vec{E}_i\left(\vec{r},\hat{\theta}_0\right) = \int_0^{2\pi} I\left(\sigma+\hat{\theta}_0\right)\vec{E}_i\left(\vec{r},\sigma\right)R\,d\sigma \qquad (4.16)$$

84

The corresponding scattered field can be expressed as

$$\vec{E}_s\left(\phi,\hat{\theta}_0\right) = \int_0^{2\pi} I\left(\sigma + \hat{\theta}_0\right)\vec{E}_s\left(\phi,\sigma\right)R d\sigma \tag{4.17}$$

where $\vec{E}_s\left(\phi,\hat{\theta}_0\right)$ is the scattered field measured at position ϕ generated by an incident cylindrical wave produced by a line source located at σ and $I\left(\sigma + \hat{\theta}_0\right)$ is

$$I\left(\sigma + \hat{\theta}_0\right) = \frac{-2}{\omega\mu_0 R\pi} \sum_{m=-\infty}^{\infty} \frac{j^m}{H_m^{(2)}\left(k_0 R\right)} e^{jm\left(\sigma+\hat{\theta}_0\right)} \tag{4.18}$$

Using (4.15) and (4.17), the 2D Fourier transform of the contrast profile is

$$\tilde{C}\left(k_0\left(\hat{\theta}-\hat{\theta}_0\right)\right) = \frac{1}{j\omega\varepsilon_0} R^2 \int_0^{2\pi}\int_0^{2\pi} \vec{E}_s\left(\phi,\sigma\right)I\left(\phi-\hat{\theta}\right)I\left(\sigma+\hat{\theta}_0\right)d\phi d\sigma \tag{4.19}$$

The term $I\left(\phi-\hat{\theta}\right)I\left(\sigma+\hat{\theta}_0\right)$ in equation (4.19) can be defined as

$$I(\phi,\sigma) = I\left(\phi-\hat{\theta}\right)I\left(\sigma+\hat{\theta}_0\right)$$

$$= \left(\frac{2}{\omega\mu_0 R\pi}\right)^2 \sum_{n=-\infty}^{\infty}\sum_{m=-\infty}^{\infty} \frac{j^n}{H_n^{(2)}\left(k_0 R\right)} e^{jn\left(\phi-\hat{\theta}\right)} \frac{j^m}{H_m^{(2)}\left(k_0 R\right)} e^{jm\left(\sigma+\hat{\theta}_0\right)} \tag{4.20}$$

4.4   Reconstruction Algorithm

The circular array consists of N antennas in the xy-plane. As noted above, a sample of the scattering field $\vec{E}_s\left(\phi,\sigma\right)$ can be obtained by transmitting alternatively with each antenna and receiving each time with the other N-1 antennas.

Equation (4-19) can be seen as a 2D convolution between the scattered field and the current that generates a plane wave existing along the circular array. This convolution can be calculated as the inverse Fourier transform of the product between the corresponding spectra.

$$\vec{E}_S(\phi,\sigma) * I(\phi,\sigma) = \mathsf{F}^{-1}\{\tilde{E}_S(\phi,\sigma) \cdot \tilde{I}(\phi,\sigma)\}$$ (4.21)

For an array of transmitting and receiving antennas placed along a circle of radius R, the spectrum of the scattered field can be calculated as

$$\tilde{E}_S(r,t) = \int\limits_{-\infty}^{\infty}\int\limits_{-\infty}^{\infty} E_S(\phi,\sigma)e^{-jr\phi}e^{-jt\sigma}$$

$$= \int\limits_{-\infty}^{\infty}\int\limits_{-\infty}^{\infty} -\frac{k_0^2 I}{4\omega\varepsilon_0} \sum_{n=-\infty}^{\infty} a_n\left(H_n^{(2)}(k_0 R)\right)^2 e^{jn(\phi-\sigma)}e^{-jr\phi}e^{-jt\sigma}d\phi d\sigma$$

$$= -\frac{k_0^2 I}{4\omega\varepsilon_0} \sum_{n=-\infty}^{\infty} a_n\left(H_n^{(2)}(k_0 R)\right)^2 \int\limits_{-\infty}^{\infty}\int\limits_{-\infty}^{\infty} e^{j(n-r)\phi}e^{-j(n-t)\sigma}d\phi d\sigma$$

$$= -\frac{k_0^2 I}{4\omega\varepsilon_0} \sum_{n=-\infty}^{\infty} a_n\left(H_n^{(2)}(k_0 R)\right)^2 \delta(n-r)\delta(n+t)$$

$$\tilde{E}_S(r,t) = \begin{cases} -\dfrac{k_0^2 I}{4\omega\varepsilon_0} a_t\left(H_n^{(2)}(k_0 R)\right)^2 & t=-r \in \square \\ \\ 0 & otherwise \end{cases}$$ (4.22)

where a_n is defined in (3.19). The Fourier transform of the current $I(\phi,\sigma)$ defined in (4.20) can

be calculated as follows. Rearranging (4.20) we obtain,

86

$$I(\phi,\sigma) = \left(\frac{2}{\omega\mu_0 R\pi}\right)^2 \sum_{n=-\infty}^{\infty} \sum_{m=-\infty}^{\infty} \frac{j^{(n+m)}}{H_n^{(2)}(k_0 R) H_m^{(2)}(k_0 R)} e^{jn\phi} e^{jm\sigma} \tag{4.23}$$

The corresponding Fourier transform of (4.23) is

$$\tilde{I}(r,t) = \left(\frac{2}{\omega\mu_0 R\pi}\right)^2 \sum_{n=-\infty}^{\infty} \sum_{m=-\infty}^{\infty} \frac{j^{(n+m)}}{H_n^{(2)}(k_0 R) H_m^{(2)}(k_0 R)} \int_{-\infty}^{\infty}\int_{-\infty}^{\infty} e^{jn\phi} e^{jm\sigma} e^{-jr\phi} e^{-jt\sigma} d\phi d\sigma$$

$$= \left(\frac{2}{\omega\mu_0 R\pi}\right)^2 \sum_{n=-\infty}^{\infty} \sum_{m=-\infty}^{\infty} \frac{j^{(n+m)}}{H_n^{(2)}(k_0 R) H_m^{(2)}(k_0 R)} \delta(n-r)\delta(m-t)$$

$$\tilde{I}(r,t) = \begin{cases} \left(\dfrac{2}{\omega\mu_0 R\pi}\right)^2 \dfrac{j^{(r+t)}}{H_r^{(2)}(k_0 R) H_t^{(2)}(k_0 R)} & t,r \in \square \\ \\ 0 & otherwise \end{cases} \tag{4.24}$$

Therefore, the discrete version of equation (4.19) is

$$\tilde{C}\left(k_0\left(\hat{\theta}-\hat{\theta}_0\right)\right) = \frac{R^2}{j\omega\varepsilon_0}\left(\frac{2\pi}{N}\right) \mathsf{F}^{-1}\left\{\tilde{E}_s(\phi,\sigma) * \tilde{I}(\phi,\sigma)\right\} \tag{4.25}$$

where F^{-1} is the inverse Fourier transform. The contrast profile can be obtained by computing the inverse Fourier transform of (4.25). Defining

$$A = -\frac{k_0^2 I}{4\omega\varepsilon_0} \tag{4.26}$$

and

$$B = \left(\frac{2}{\omega \mu_0 R \pi} \right)^2 \tag{4.27}$$

The product of the spectra $\tilde{E}_s(r,t) \cdot \tilde{I}(r,t)$ can be calculated as

$$\tilde{f}(r,t) = \tilde{E}_s(r,t) \cdot \tilde{I}(r,t)\Big|_{t=-r} = ABa_t \frac{\left(H_t^{(2)}(k_0 R) \right)^2}{H_r^{(2)}(k_0 R) H_{-t}^{(2)}(k_0 R)}$$

$$\tilde{f}(r,t) = \begin{cases} ABa_t \dfrac{H_t^{(2)}(k_0 R)}{H_{-t}^{(2)}(k_0 R)} & t = -r \in \square \\ 0 & otherwise \end{cases} \tag{4.28}$$

Calculating the inverse Fourier transform of (4.28), we obtain

$$f(\phi,\sigma) = \sum_{r=-\infty}^{\infty} \sum_{t=-\infty}^{\infty} \tilde{f}(r,t) e^{jr\phi} e^{jt\sigma} \Bigg|_{t=-r} = AB \sum_{t=-\infty}^{\infty} (-1)^t a_t e^{j(\phi-\sigma)t} \tag{4.29}$$

The contrast profile is

$$C\left(k_0 (\hat{\theta} - \hat{\theta}_0) \right) = \frac{1}{j\omega\varepsilon_0} R^2 f(\theta,\theta_0) = \frac{jI}{(k_0\pi)^2} \sum_{t=-\infty}^{\infty} (-1)^t a_t e^{j(\hat{\theta}-\hat{\theta}_0)t} \tag{4.30}$$

For a given frequency, a sampled version of the spectrum of the contrast profile inside a circle of radius $2k_0$ is obtained. In order to improve the quality of the image, a set of multiple frequencies can be combined [82]. Previously reported results lead to the conclusion that configurations with large contrast with respect to the surrounding medium can be reconstructed with an acceptable resolution by using multiple-frequency reconstruction [83][84][72]. At each

new frequency, the final result for the previous frequency is used to estimate the unknown permittivity profile. To avoid destructive frequency-dependent interferences, the average of the magnitudes of the images is used. The total contrast is given by

$$C = \sum_{f=f_{min}}^{f_{max}} \left| \mathsf{F}^{-1}\left(\tilde{C}_{k_0} \right) \right| \tag{4.31}$$

where F^{-1} is the inverse Fourier transform. Using average magnitudes produces some loss of quantitative dielectric properties information, but the size and location is preserved.

4.5   Results

The algorithm implementation was done using Matlab. The starting point of the algorithm is the scattered field measurement obtained from simulations of the cylinders presented in Chapter 3. This data is organized as a third-order matrix of dimensions $N_T \times N_R \times N_f$, where the number of transmitting and receiving antennas is the same ($N_T = N_R$) and N_f is the number of frequencies acquired. In practice, the number of antennas is limited as well as the number of frequencies. The following results are for a frequency range of 300 to 800 MHz for three separate antenna configurations: 16, 32, and 64 antennas equally-spaced in an angular sense forming a circular array. Simulations were performed for concentric and eccentric spill configurations as presented in Chapter 3.

For the centered configuration, the spill has a relative permittivity of $\varepsilon_1 = 12$ in the outer layer, corresponding to contaminated soil with 25% water content and 25% oil content, and $\varepsilon_2 = 2.2$ in the core region, corresponding to a fully contaminated soil. The surrounding medium has a relative permittivity of 17, corresponding to wet soil. The contrast of the cylinders is

constant and purely real. Using (4.6) for the large cylinder, representing the outer region of contaminated soil, the contrast is 0.294. For the small cylinder, or core region, the contrast is 0.8167. The original contrast profile and reconstructed results are shown in Figures 4-5 and 4-6.
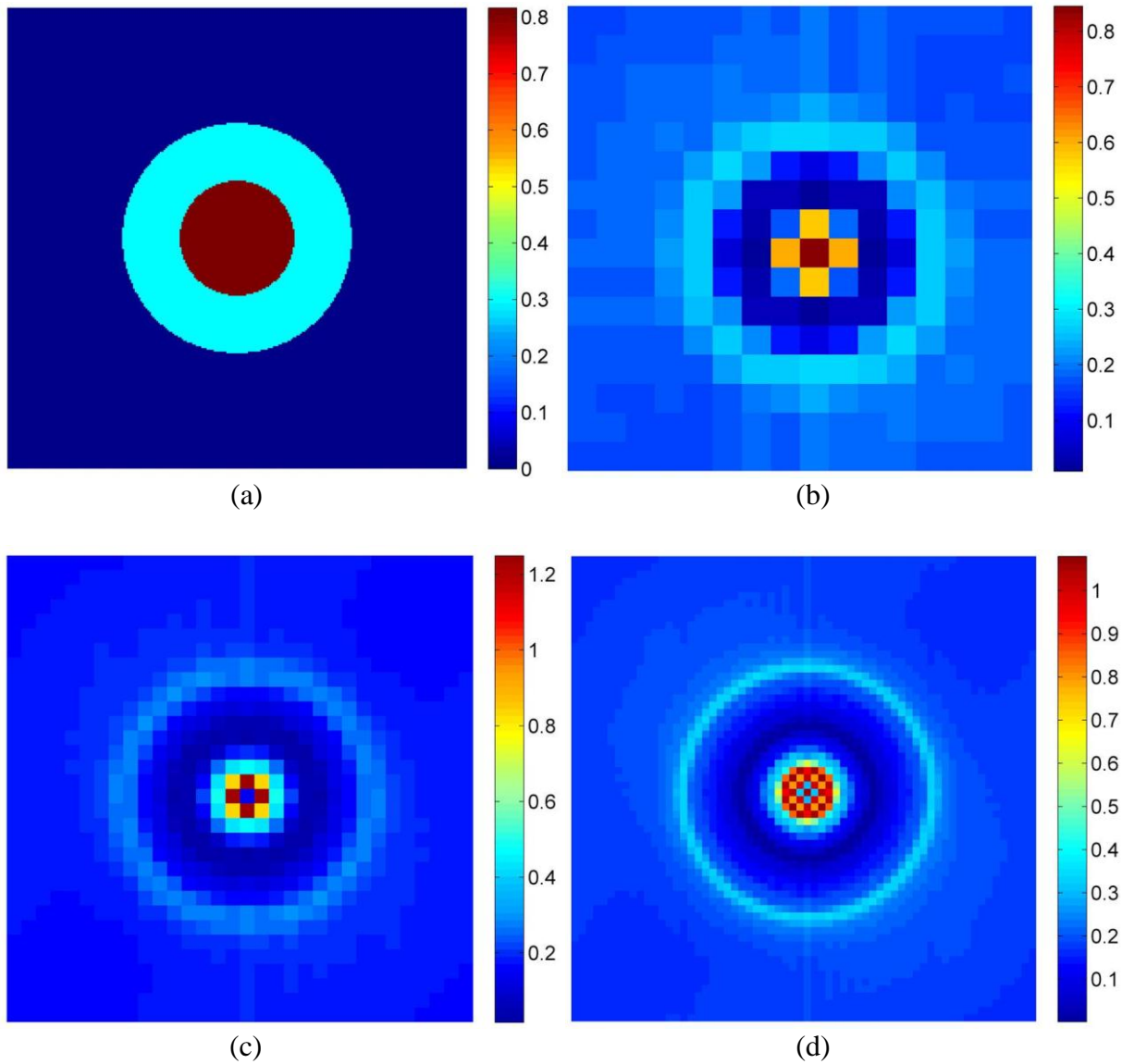
Figure 4-5. Contrast profile for a centered spill configuration. The contrast of the cylinders is constant and purely real. For the large cylinder the contrast is 0.294. For the small cylinder, or core region, the contrast is 0.8167. (a) Original image. (b) Reconstructed profile with 16 antennas. (c) Reconstructed profile with 32 antennas. (d) Reconstructed profile with 64 antennas.
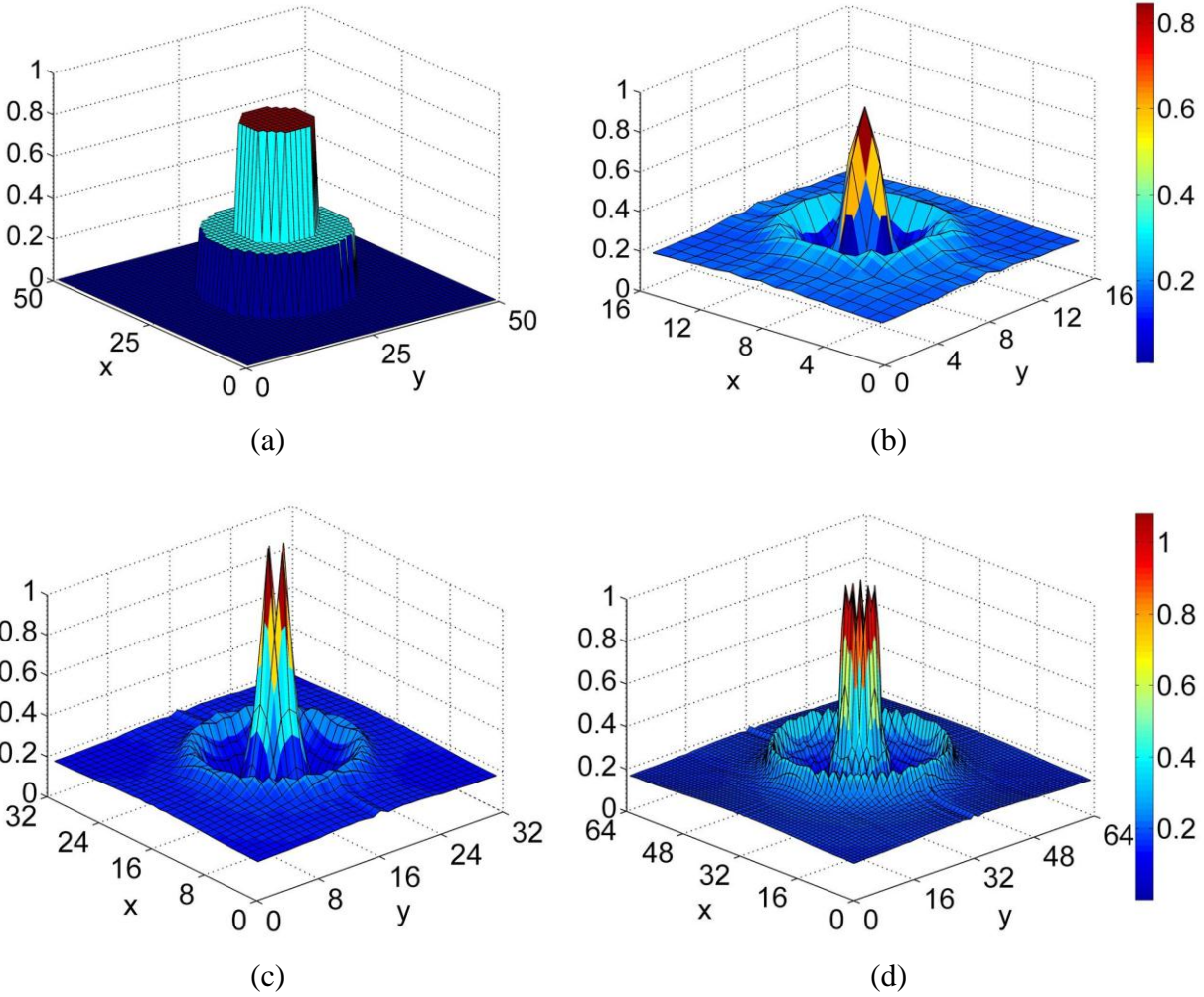
Figure 4-6. Contrast profile for a centered spill configuration. For the large cylinder the contrast is 0.294. For the small cylinder, or core region, the contrast is 0.8167. (a) Original image contrast profile. (b) Reconstructed profile with 16 antennas. (c) Reconstructed profile with 32 antennas. (d) Reconstructed profile with 64 antennas.

Results for the centered configuration showed that the algorithm can detect the spill with a poor resolution. The contrast profile is partially reconstructed, with expected contrast values at the boundary of the outer cylinder. The core cylinder is detected with a high contrast profile at the center and a contrast of almost zero at the boundary. As the number of antennas increases, the boundaries are better defined for both cylinders. Notice in Figure 4-6 that the surrounding

91

medium shows a contrast profile of approximately 0.18 instead of zero. The size of the spill is preserved.

For the eccentric case, the same contrast profile was used. Results are shown in Figures 4-7 and 4-8.
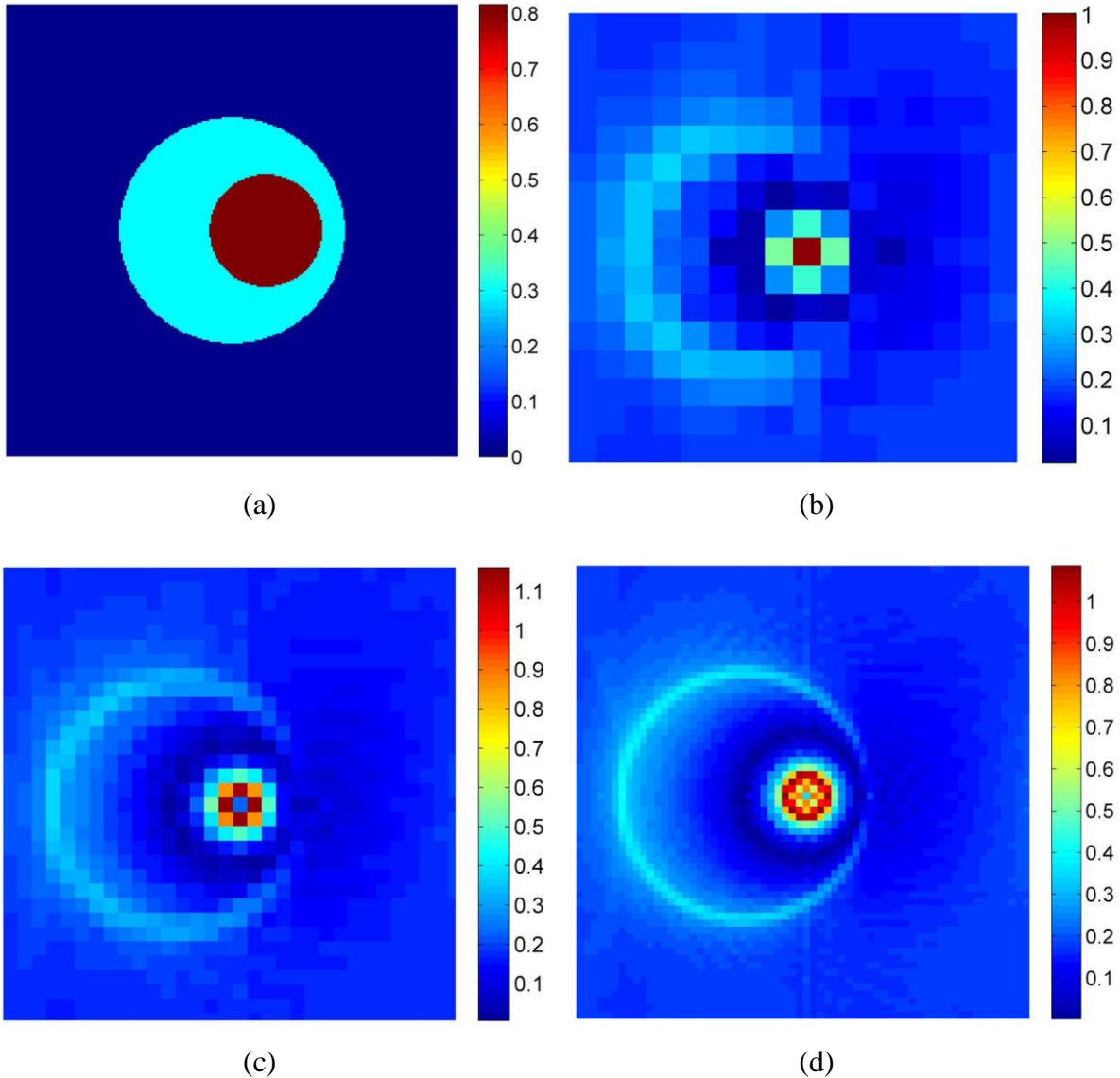
Figure 4-7. Contrast profile for an eccentric spill configuration. The contrast of the cylinders is constant and purely real. For the large cylinder the contrast is 0.294. For the small cylinder, or core region, the contrast is 0.8167. (a) Original image. (b) Reconstructed profile with 16 antennas. (c) Reconstructed profile with 32 antennas. (d) Reconstructed profile with 64 antennas.
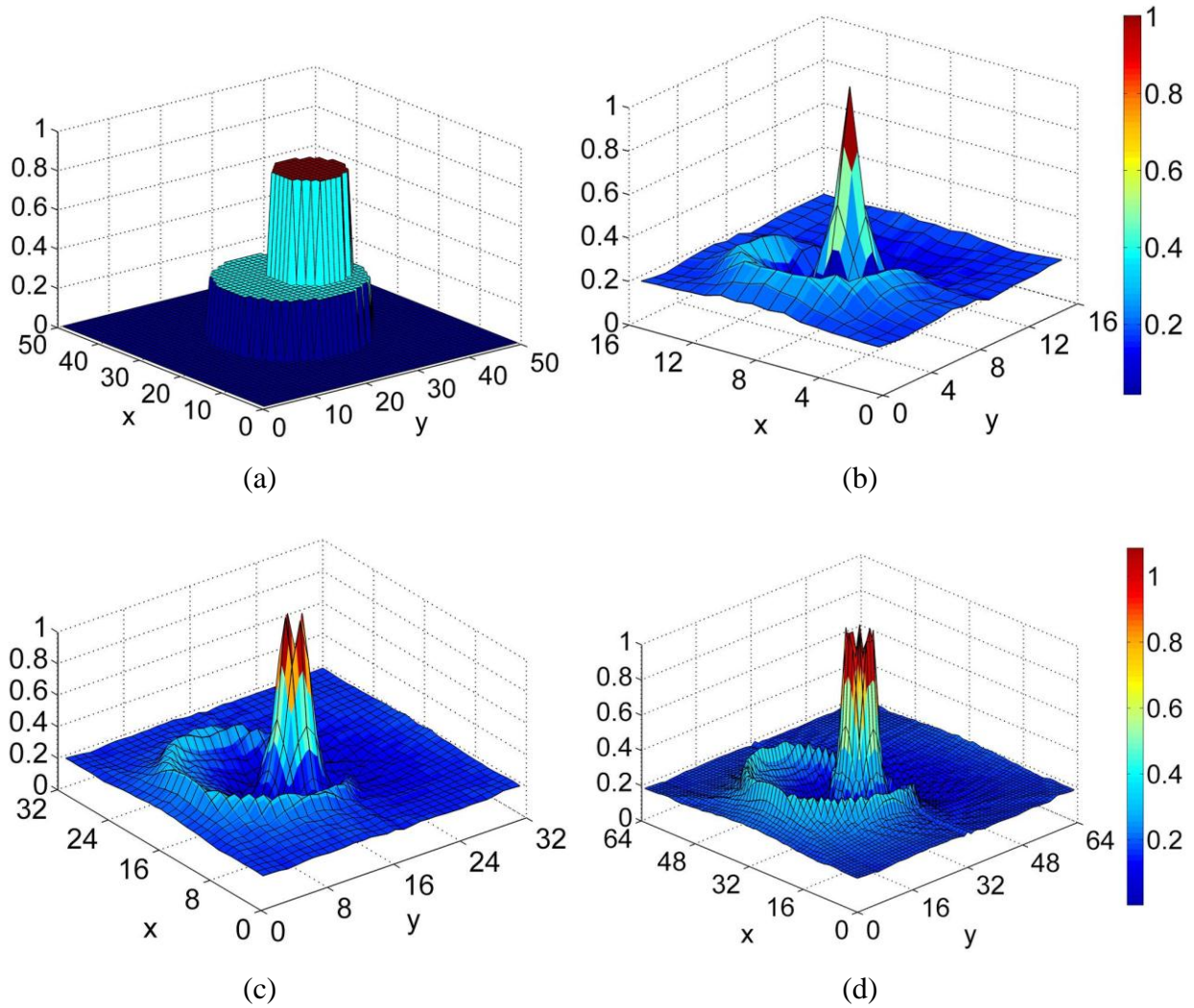
Figure 4-8. Contrast profile for a centered spill configuration. The contrast of the cylinders is constant and purely real. For the large cylinder the contrast is 0.294. For the small cylinder, or core region, the contrast is 0.8167. (a) Original image. (b) Reconstructed profile with 16 antennas. (c) Reconstructed profile with 32 antennas. (d) Reconstructed profile with 64 antennas.

Reconstructed profile for the eccentric case showed that the image is affected by the position of the core cylinder. The outer cylinder is blended with the core cylinder and the contrast profile is not obtained. Hence, if the material within the resolution cell is a blend of the two materials, the resulting image is blurred. This is to be expected with any non-parametric

imaging algorithm. Parametric algorithms, which are beyond the scope of this research, utilize *a priori* information to sharpen the image. Such information involving the permittivity profile is generally not available for the remote sensing scenario under investigation herein. Also, the reconstructed image is shifted to the side opposite to the position of the core. In other words, the reconstructed image is centered with the core cylinder. As before, the surrounding medium appears with a contrast of 0.18.

In both cases, the reconstructed images conserve the size of the spill and the boundaries are well defined. At the boundary of the outer cylinder, the contrast profile obtained with 64 antennas, has an average value of 0.2798. This is close to the original contrast of 0.294. The maximum value obtained at the core cylinder for the same number of antennas is 0.849.

The inversion method presented in this chapter can be used for detection of spills based on the contrast between contaminated soils. The results of the simulation model are, at least from a geometrical standpoint, acceptable. The algorithm is able to determine the position of the spill and the core cylinder. The contrast and therefore, permittivities of the soil and contaminated soil can be determined by the color variance in the images.

CHAPTER 5

CONCLUSIONS AND FUTURE WORK

The primary goal of this work was to simulate a contaminated region and determine its physical limits within a tolerable level of certainty given the characteristics of the soil in question without the environmental and financial cost of physical experimentation. To achieve this, the first part of this study focused in the determination of the dielectric properties of soil and contaminated soil. A coaxial waveguide for measuring the complex permittivity and permeability of soil and contaminated soil was designed and tested successfully. Different from existing sample holders, the new sample holder was fabricated to accommodate significant volumetric samples of material. This type of sample holder is attractive for large measurement programs were larger samples are needed.

Air and Plexiglas samples were measured to verify the reliability and accuracy of the measurement system. Results obtained for air, Plexiglas, and the dry soil samples were as expected. The increase in relative permittivity for the soil with moisture was reasonable.

The measured contrast between dry soil and dry soil contaminated with oil was within the nominal uncertainty of the experiment and hence it is not expected that a rise in permittivity for dry soil contaminated with fairly high volumetric concentrations of oil will allow sufficient contrast for either radio frequency bore-hole or GPR mapping. There was however a significant difference between the measured permittivity for wet soil and that of wet soil contaminated with oil as shown in Table 5-1. Hence, it is reasonable that this permittivity contrast can be used as a discriminator for detecting contamination plumes. This is significant since contamination in an aquifer is one of the most environmentally challenging issues facing the world.

Table 5-1. Percent difference for permittivity values of wet- and wet-contaminated soils.

Real relative permittivity (Average)	Moisture Content	
	10%	25%
Wet soil	6.9148	17.2000
Wet–contaminated soil	5.5271	11.7855
% DIFFERENCE	22.3%	37.36%

The ground-truth obtained in these experiments was used to simulate contaminants in soil and determine the scattering characteristics of NAPL's spills. The problem is two-dimensional and the effects of various geometrical and electrical parameters were examined. Results for plane wave and line source excitations for homogeneous and inhomogeneous spills were obtained.

Scattered field matrices obtained was used as input parameter in the inversion algorithm. The inversion algorithm is based in the Fourier Diffraction theorem and, in order to improve the quality of the image, a set of multiple frequencies are combined. To avoid destructive frequency-dependent interferences, the average of the magnitudes of the images was used. Using average magnitudes produces some loss of quantitative dielectric properties information, but the size and location is preserved. The results obtained for concentric and eccentric spills showed that the reconstructed images conserved the size of the spill and the boundaries were well defined. At the boundary of the outer cylinder, the contrast profile obtained with 64 antennas, has an average value of 0.2798. This is close to the original contrast of 0.294. The maximum value obtained at the core cylinder for the same number of antennas is 0.849, close to the original contrast of 0.817.

The inversion method presented can be used for detection of spills based on the contrast between contaminated soils. The results of the simulation model were, at least from a geometrical standpoint, acceptable. The algorithm was able to determine the position of the spill and the core cylinder. The contrast and therefore, permittivities of the soil and contaminated soil can be determined by the color variance in the images.

There are several directions in which this work may be extended. The influence of variations in the background medium must be further investigated in order to improve the accuracy of the system. Larger spills with respect to wavelength should be analyzed. Also, the effects of increasing bandwidth without increasing the number of transmitters/receivers should be analyzed. Concerning experimental measurements, it would be interesting to test the algorithm with data form a real oil spill site instead of simulated values. Also, the design of the borehole and antenna system is worth looking into. Low frequencies need to be used and the system needs to be low-powered, because of the possible explosive hazard of gases situated in the subsurface. Also, the electronic components of the system must be able to withstand the extreme temperatures and the moisture in the boreholes.

The work presented could have useful applications in the geophysical and biomedical areas. Future work will be directed in those areas.

BIBLIOGRAPHY

BIBLIOGRAPHY

[1]   A.M. Chrestman, G.D. Comes, S.S. Kooper, and P.G. Malone, "Rapid detection of hydrocarbon contamination in ground water and soil," *Proceedings of the Hydraulic Engineering*, Water Forum '92, Baltimore, Maryland, August 2–6, pp. 1165-1170, 1992.

[2]   United States Environmental Protection Agency. (2009, July 31). *Drinking Water Contaminants* [Online]. Available: http://water.epa.gov/drink/contaminants

[3]   United States Environmental Protection Agency. (2005, March 23). *Cost and Performance Report for LNAPL Recovery* [Online]. Available: http://www.epa.gov/tio/download/rtdf/napl/cpbpsugarcreek.pdf

[4]   Remediation Technologies Development Forum. (2005, March 21). *"The Basics" Understanding the Behavior of Light Non-Aqueous Phase Liquids (LNAPLs) in the Subsurface* [Online]. Available: http://www.rtdf.org/public/napl/training/module1.pdf

[5]   J. Ryan. (2009). *Leaking underground storage tanks* [Online]. Available: http://bcn.boulder.co.us/basin/waterworks/lust.html

[6]   F. Nadim, G. E. Hoag, S. Liu. R. J. Carley, and P. Zack, "Detection and remediation of soil and aquifer systems contaminated with petroleum products: an overview," *Journal of Petroleum Science and Engineering*, vol. 26, pp. 168-178, 2000.

[7]   C. J. Newell, S. D. Acree, R. R. Ross, and S. G. Huling, "Light nonaqueous phase liquids," *Ground Water Issue*, EPA/540/S-95/500, U.S.EPA, R.S. Kerr Environ. Res. Lab., Ada, OK, pp. 1-28, 1995.

[8]   A.J. Devaney, "Geophysical diffraction tomography," *IEEE Trans. Geosc.Remote Sensing*, vol. GE-22, no. 1, pp. 3-13, Jan.1984.

[9]   A.G. Tijhuis, K. Belkebir, A.C.S. Litman, and B.P. deHon, "Multiple-frequency distorted-wave Born approach to 2D inverse profiling," *Inverse Problems*, vol. 17, pp. 1635-1644, 2001.

[10]   Standard Guide for Using the Surface Ground Penetrating Radar Method for Subsurface Investigation, ASTM Standard D 6432 – 99 (Reapproved 2005).

[11]   Timur, A. and Toksöz, M. N., "Downhole geophysical logging," *Annual Review of Earth and Planetary Sciences*, vol. 13, pp.315-344, 1985.

[12]   J. Baker-Jarvis, M.D. Janezic, B.F. Riddle, R.T. Johnk, P. Kabos, C.L. Holloway, R.G. Geyer, and C.A. Grosvenor, "Measuring the permittivity and permeability of lossy materials: solids, liquids, metals, building materials, and negative-index materials," *NIST Tech. Note 1536*, Boulder, CO, December 2004.

[13]   J.O. Curtis, "A durable laboratory apparatus for the measurement of soil dielectric properties," *IEEE Trans. Instrum. Meas.*, vol. 50, no. 5, pp. 1364-1369, Oct. 2001.

[14]   A.M. Nicholson and G.F. Ross, "Measurement of the intrinsic properties of materials by time-domain techniques," *IEEE Trans. Instrum. Meas*., vol. IM-19, pp. 377-382, Nov. 1970.

[15]   W.B. Weir, "Automatic measurement of complex dielectric constant and permeability at microwave frequencies," *Proc. IEEE*, vol. 62, no.1, pp. 33-36, Jan. 1974.

[16]   J. Baker-Jarvis, E.J. Vanzura, and W.A. Kissick, "Improved technique for determining complex permittivity with the Transmission/Reflection method," *IEEE Trans. Microwave Theory Tech*., vol. 38, no. 8, pp.1096-1103, August 1990.

[17]   A.H. Boughrie, C. Legrand, A. Chapoton, "Non-iterative stable transmission/reflection method for low-loss material complex permittivity determination", *IEEE Trans. Microwave Theory Tech*., vol. 45, no.1, pp. 52-57, January 1997.

[18]   C.C. Courtney, "Time-domain measurement of the electromagnetic properties of materials," *IEEE Trans. Microwave Theory Tech*., vol. 46, no. 5, pp. 517-522, May 1998.

[19]   D.M. Pozar, *Microwave Engineering*, New York: Wiley, 2005.

[20]   HVS Technologies, Inc., 2597-2 Clyde Ave., State College, PA 16801.

[21]   G.F. Engen and C.A. Hoer, "Thru-Reflection-Line: An improved technique for calibrating the dual six-port automatic network analyzer," *IEEE Trans. Microwave Theory Tech*., vol. MTT-27, no. 12, pp. 987-993, Dec. 1979.

[22]   A. R. Von Hippel, *Dielectric Materials and Applications*, New York: Wiley, 1954.

[23]   USDA Natural Resources and Conservation Service Web Soil Survey. (2009, November 11). *Report OH119 Muskingum County OH* [Online]. Available: http://websoilsurvey.nrcs.usda.gov/app/

[24]   American Association of State Highway and Transportation Officials Standards and Guidelines. (2004). *T-265: Laboratory Determination of Moisture of Soils* [Online]. Available: http://www.dot.nd.gov/manuals/materials/testingmanual/t265.pdf

[25]   J.H. Dane and G.C. Topp, *Methods of Soil Analysis, Part 4 – Physical Methods*, Soil Science Society of America, Inc., Madison, WI, 2002.

[26]   N.R. Peplinski, F.T. Ulaby, and M.C. Dobson, "Dielectric properties of soils in the 0.3 – 1.3 GHz range," *IEEE Trans. Geosc. Remote Sensing*, vol. 33, no. 3, pp. 803-807, May 1995.

[27] M.C. Dobson, F.T. Ulaby, M. Hallikainen, and M. El-Rayes, "Microwave dielectric behavior of wet soil – Part II: four-component dielectric mixing models," *IEEE Trans. Geosc. Remote Sensing*, vol. GE-23, no. 1, pp. 35-41, January 1985.

[28] F.T. Ulaby, R.K. Moore, and A.K. Fung, *Microwave Remote Sensing,* vol. 3, Dedham, MA: Artech House, 1986, Appendix E.

[29] A. Sihvola, *Electromagnetic Mixing Formulas and Applications*, IEE Electromagnetic Waves Series 47, Michael Faraday House, UK, 1999.

[30] A. Sihvola, "Mixing rules with complex dielectric coefficients," *Subsurface Sensing Technologies and Applications*, vol. 1, no. 4, pp. 393-415, October 2000.

[31] W.R Tinga, W.A.G Voss, D.F. Blossey, "Generalized approach to multiphase dielectric mixture theory," *J. Appl. Phys.* vol. 44 no. 9, pp. 3897, 1973.

[32] J.C. Maxwell Garnett, "Colours in metal glasses and metal films," *Trans. of the Royal Society*, vol. CCIII, pp. 385–420, 1904.

[33] D. Polder and J.H. van Santen, "The effective permeability of mixtures of solids", *Physica*, vol. 12, no. 5, p. 257–271, 1946.

[34] D.A.G. Bruggeman, "Berechnung verschiedener physikalischer Konstanten von heterogenen Substanzen. I. Dielektrizitätskonstanten und Leitfähigkeiten der Mischkörper aus isotropen Substanzen," *Annalen der Physik*, vol. 416, no. 8, pp. 665–679, 1935.

[35] L. Tsang, J.A. Kong, and R.T. Shin, *Theory of microwave remote sensing*, Wiley New York, 1985.

[36] U. Kaatze, **"**Complex permittivity of water as a function of frequency and temperature," *J. Chem. Eng. Data*, vol. 34, no. 4, pp. 371-374, October 1989.

[37] W.J. Ellison, "Permittivity of Pure Water, at Standard Atmospheric Pressure, over the Frequency Range 0–25 THz and the Temperature Range 0–100 °C," *J. Phys. Chem. Ref. Data*, vol. 36, pp. 1-18, 2007.

[38] W.M. Alley, T.E. Reilly, and O.L. Franke, "Sustainability of Ground-Water Resources," *U.S. Geological Survey Circular 1186*, Denver, Colorado, 1999.

[39] F.M. Francisca, and V.A. Rinaldi, "Complex dielectric permittivity of soil-organic mixtures (20 MHz-1.3 GHz)", *Journal of Environmental Engineering*, vol. 129, no. 4, pp. 347-357, April 2003.

[40] B.B.S. Singhal and R.P. Gupta, "Groundwater Contamination" in *Applied Hydrogeology of Fractured Rocks*, Springer Netherlands, 2010, ch.12, pp. 221-236.

[41] A. Sihvola, "Model systems for materials with high dielectric losses in aquametry," in *Electromagnetic Aquametry: Electromagnetic Wave Interaction with Water and Moist Substances*, K. Kupfer Ed., Springer-Verlag Berlin Heidelberg, 2005, ch. 5, pp. 93-111.

[42] C.M. Rappaport, "Ground penetrating radar," in *The RF and Microwave Handbook, Volume 1*, Mike Goglio Ed., CRC Press, Boca Raton, FL, 2008, ch. 17.

[43] A. Ramírez, W. Daily, A. Binley, and D. Roelant, "Detection of leaks in underground storage tanks using electrical resistivity methods," *Journal of Environmental and Engineering Geophysics*, vol. 1, no. 3, pp. 189-203, December, 1996.

[44] D. Eisenburger and V. Gundelach, "A new direction-sensitive borehole logging tool for the spatial reconnaissance of geological structures," *Proceedings of the 12th International Conference on Ground Penetrating Radar*, Birmingham, UK, June 16-19, 2008.

[45] S.E. Prensky, "Advances in borehole imaging technology and applications," in *Borehole Imaging: Applications and Case Histories*, Lowell, Williamson, and Harvey Eds., Geological Society Special Publication No. 159, UK, 1999, pp. 1-44.

[46] A.A. Kishk, R.P. Parrikar, and A.Z. Elsherbeni, "Electromagnetic Scattering from an Eccentric Multilayered Circular Cylinder," *IEEE Trans. Antennas and Prop.*, vol.40, no. 3, pp. 295-303, March 1992.

[47] S.J. Radzevicius and J.J. Daniels, "Ground penetrating radar polarization and scattering from cylinders," *Journal of Applied Geophysics*, vol. 45, no. 2, pp. 111-125, September 2000.

[48] R.F. Harrington, *Time-Harmonic Electromagnetic Fields*, New York: McGraw-Hill, 1961.

[49] C. Balanis, *Advanced Engineering Electromagnetics*, New York: Wiley, 1989.

[50] M. Abramowitz and I. Stegun, *Handbook of Mathematical Functions*, New York, Dover Publications, 1972.

[51] G.T. Ruck, D.E. Barrick, W.D. Stuart, and C.K. Krichbaum, *Radar Cross Section Handbook*, New York: Plenum, 1970.

[52] A.P. Annan, J.L. Davis, "Ground-penetrating radar for high-resolution mapping of soil and rock stratigraphy," *Geophysical Prospecting*, vol. 37, no. 5, pp. 531-551, 1989.

[53] J.A. Stratton, *Electromagnetic Theory*, New York: McGraw-Hill, 1941.

[54] S. Lambot, I. Van den Bosch, B. Stockbroeckx, P. Druyts, M. Vanclooster, E.C. Slob, "Frequency dependence of the soil dielectric properties derived from ground penetrating radar signal inversion," *Subsurface Sensing Technologies and Applications*, vol.6, no. 1, pp. 73-87, 2005.

[55]   S. Lambot, E. Slob, J. Minet, K.Z. Jadoon, M. Vanclooster, and H. Vereecken, "Full-waveform modeling and inversion of ground-penetrating radar data for non-invasive characterization of soil hydrogeophysical properties," in *Proximal Soil Sensing*, *Progress in Soil Science I,* R.A.Viscarra-Rossel, A.B. McBratney, B. Minasny, Eds., Springer Science and Business Media, 2010, ch. 25, pp. 299-311.

[56]   C.M. Rappaport, "Ground Penetrating Radar," in *RF and Microwave Applications and Systems,* M. Goglio and J. Goglio Eds., CRC Press, 2nd Ed., 2008, ch. 17.

[57]   M. Farid, A. N. Alshawabkeh, and C. M. Rappaport, "Electromagnetic waves in contaminated soils," in *Electromagnetic Waves in Complex Matter*, Ahmed Kishk Ed., InTech, 2011, ch. 5, pp. 117-154.

[58]   M. Farid, A. N. Alshawabkeh, H. Zhan, and C. M. Rappaport, "Challenges and Validation of Cross Tomography Experimentation for Inverse Scattering Problems in Soils," in *Proc. of Geo-Frontiers 2005: GSP 138, Site Characterization and Modeling*, 2005 © ASCE Conf. Proc. doi: 10.1061/40785(164)39.

[59]   H. Zhan, C. M. Rappaport, M. Farid, A. N. Alshawabkeh, and H. Raemer, "Lossy half-space Born approximation modeling of electromagnetic wave source and scattering by soil by cross well radar," *Proc. of Geo-Frontiers 2005: GSP 138, Site Characterization and Modeling*, 2005 © ASCE Conf. Proc. doi: 10.1061/40785(164)38.

[60]   E.Wolf, "Three-dimensional structure determination of semi-transparent objects from holography data," *Optics Communications*, vol. 1, pp.153-156, 1969.

[61]   T.J.Cui, and W.C. Chew, "Novel diffraction tomographic algorithm for imaging two-dimensional dielectric objects buried under a lossy earth," *IEEE Trans. Geosci. Remote Sensing*, vol. 38, no. 4, pp. 2033-2041, July 2000.

[62]   T.J. Cui, and W.C. Chew, "Diffraction tomographic algorithm for the detection of three-dimensional objects buried in a lossy half space," *IEEE Trans. Antennas and Propagation*, vol. 50, no. 1, pp. 42-49, Jan. 2002.

[63]   S.K. Lehman, "Superresolution planar diffraction tomography through evanescent fields," *Int. J. Imaging Systems Technol.*, vol. 12, pp. 16-26, 2002.

[64]   W.C. Chew, *Waves and Fields in Inhomogeneous Media*, chapter 2, IEEE Press, Piscataway, NJ, 1997.

[65]   M. Soumekh, "A system model and inversion for synthetic aperture radar imaging," *IEEE Trans. Image Processing*, vol. 1, no. 1, pp. 64-76, Jan. 1992.

[66]   J.M. Lopez-Sanchez and J. Fortuny-Guasch, "3-D radar imaging using range migration techniques," *IEEE Trans. Antennas and Propagation*, vol. 48, no. 5, pp. 728-737, May 2000.

[67] R. Deming, and A.J. Devaney, "Diffraction tomography for multi-monostatic ground penetrating radar imaging," *Inverse Problems*, vol. 13, pp. 29-45, 1997.

[68] T. Hansen, B. and P.M. Johansen, "Inversion scheme for monostatic ground penetrating radar that takes into account the planar air-soil interface," *IEEE Trans. Geosci. Remote Sensing*, vol. 38, no. 1, pp. 496-506, Jan. 2000.

[69] A. Kak and M. Slaney, "Tomographic Imaging with Diffracting Sources," in *Principles of Computarized Tomographic Imaging*, SIAM Classics in Applied Mathematics, ch. 6, pp. 203-273, 2001.

[70] L. LoMonte, A.M. Bagci, D. Erricolo, and R. Ansari, "Spatial resolution in tomographic imaging with diffracted fields," *Proc. URSI General Assembly 2008* [Online] Available: http://www.ursi.org/proceedings/procGA08/papers/B07p2.pdf.

[71] M. Slaney, A. Kak, and L. Larsen, "Limitations of imaging with first-order diffraction tomography," *IEEE Transactions on Microwave Theory and Techniques*, vol. 32, pp. 860-874, 1984.

[72] A.G. Tijhuis, K. Belkebir, A.C.S. Litman, and B.P. deHon, "Theoretical and computational aspects of 2-D inverse profiling," *IEEE Trans. Geosci. Remote Sensing*, vol. 39, no. 6, pp. 1316-1330, June 2001.

[73] G.A. Tsihrintziz and A.J. Devaney, "Maximum likelihood estimation of object location in diffraction tomography, part II: strongly scattering objects," *IEEE Trans. Signal Processing*, vol.39, no. 6, pp. 1466-1470, June 1991.

[74] M. Pastorino, *Microwave Imaging*, New Jersey: John Wiley & Sons, 2010.

[75] K.W.Suh., S.Y. Kim, and J.W. Ra, "Electromagnetic reconstruction of 2D permittivity profiles of inhomogeneous dielectric cylinder by the diffraction slice-projection algorithm", *IEEE Transactions on Magnetics*, vol. 29, no. 2, pp. 1799-1802, March 1993.

[76] S.X. Pan and A.C. Kak, "A computational study of reconstruction algorithms for diffraction tomography: interpolation versus filtered backpropagation," *IEEE Trans. On Acoustics, Speech, and Signal Proc.,* vol. ASSP-31, no. 5, pp. 1262-1275, Oct. 1983.

[77] J. Rius, C. Pichot, L. Jofre, J. Bolomey, N. Joachimowicz, A. Broquetas, and M. Ferrando, "Planar and cylindrical active microwave temperature imaging: numerical simulations," *IEEE Transactions on Medical Imaging*, vol. 11, pp. 457-459, 1992.

[78] J. M. Rius, M. Ferrando, L. Jofre, E. de los Reyes, A. Elias-Fuste, and A. Broquetas, "Microwave tomography: an algorithm for cylindrical geometries," *Electronics Letters*, vol. 23, pp. 564-565, 1987.

[79] P.M. Morse and M. Feshbach, *Methods of Theoretical Physics*, McGraw-Hill, New York, 1953.

[80] M. Born and E. Wolf, *Principles of Optics,* Pergamon Press, New York, 1965.

[81] A. Broquetas, "Tomografía de Microondas en geometria cilíndrica para aplicaciones biomédicas," Ph.D. Dissertation, Universitat Politècnica de Catalunya, Barcelona, Spain, 1989.

[82] M.G. García, "UWB Tomography for Breast Tumor Detection," M.S. Thesis, Dept. of Signal Theory and Communications, Universitat Politècnica deCatalunya, Barcelona, Spain, 2009.

[83] W.C. Chew and J.H. Lin, "A frequency-hopping approach for microwave imaging of large inhomogeneous bodies," *IEEE Microwave and Guided Wave Letters*, vol. 15, pp. 439-441, 1995.

[84] Y. Chen, "Inverse scattering via Heisenberg's uncertainty principle," *Inverse Problems*, vol. 13, pp. 253-282, 1997.